CWP-492
July 2004

Time-Lapse Monitoring with Coda Wave Interferometry

Alexandre A. Grêt

— Doctoral Thesis —
Geophysics

Defended on July 19, 2004

Committee Chair:	Prof. Ugur Ozbay
Co-Advisors:	Prof. John A. Scales
	Prof. Roelof K. Snieder
Committee members:	Prof. Michael L. Batzle
	Prof. Thomas M. Boyd
	Prof. Luis Tenorio

Center for Wave Phenomena
Colorado School of Mines
Golden, Colorado 80401
(1) 303 273-3557

Abstract

The coda of seismic waves consists of that part of the signal after the directly arriving phases. In a finite medium, or in one that is strongly heterogeneous, the coda is dominated by waves which have repeatedly sampled the medium. Small changes in a medium which may have no detectable influence on the first arrivals are amplified by this repeated sampling and may thus be detectable in the coda. We refer to this use of multiple-sampling coda waveforms as *coda wave interferometry.* We have exploited ultrasonic coda waves to monitor time-varying rock-properties in a laboratory environment. We have studied the dependence of velocity on uni-axial stress in Berea sandstone, the temperature dependence of velocity in granite and in aluminum, and the change in velocity due to an increase of water saturation in sandstone. Furthermore, We applied coda wave interferometry to seismic data excited by a hammer source, collected at an experimental hard rock mine, Idaho Springs, CO. We carried out a controlled stress-change experiment in a pillar and we were able to monitor the internal stress change. We used coda wave interferometry to monitor temporal changes in the subsurface of the Mt. Erebus Volcano, Antarctica. Mt. Erebus is one of the few volcanoes known to have a convecting lava lake. The convection provides a repeating seismic source producing seismic energy that propagates through the strongly scattering geology in the volcano. There are many other possible applications of coda wave interferometry in geophysics, including dam and nuclear waste deposit monitoring, time-lapse reservoir characterization, earthquake relocation, stress monitoring in surface mining and rock physics.

To Adrienne

"Dear Mr. Freud

...The quest of international security involves the unconditional surrender by every nation, in a certain measure, of its liberty of action–its sovereignty that is to say–and it is clear beyond all doubt that no other road can lead to such security...

Yours very sincerely,

A. Einstein"

"Dear Mr. Einstein

...There is but one sure way of ending war and that is the establishment, by common consent, of a central control which shall have the last word in every conflict of interests...

Yours,

Sigm. Freud"

Why War?
The Einstein-Freud correspondence (1931-1932)

Table of Contents

Acknowledgments

I would like to thank Prof. Roel Snieder who started the whole coda wave interferometry avalanche. I am grateful for all his great ideas and all the exciting discussions on scattering, coda, volcanoes, cycling and an endless list of scientific, political and personal topics. The door of Roel's office was always open and he always had an open ear for my questions and problems, especially during times when I wanted to ditch the whole Ph.D. stuff.

My very special gratitude goes to Prof. John A. Scales. I have rarely seen a person with more enthusiasm and energy. John not only created the Physical Acoustics Laboratory but by doing so he built a place where graduate and undergraduate students, professors, visitors, family and Charlie meet to talk about anything and everything. If I'd have to pick the single most valuable thing I learned from John it would be his attitude toward research, or as he likes to say "let's do it!"

It would be meaningless to rave about the Lab without acknowledging Kasper van Wijk, Albena Mateeva, Alison Malcolm, Brian Zadler, Hans Ecke and Matt Haney who all carry the vibes of this special place.

Without Prof. Mike Batzle none of my experimental work would have been possible. Every experiment starts with consulting Mike and the Center for Rock Physics where anything is possible, even creating our own beer label.

The Center for Wave Phenomena and its sponsors supported me and not only financially. In particular, I thank Prof. Ken Larner for making sure that the Center for Wave Phenomena can continue to be a learning place for all of us. I acknowledge Barbara McLenon, Michelle Szobody and Sara Summers for making the wheel go round. I extend my thanks to all the faculty and student members of the Center for Wave Phenomena and the Department of Geophysics, for their friendship and encouragements.

I thank Prof. Luis Tenorio who is not only a mathematician asking awkward questions but a friend who has partial responsibility for my caffeine addiction. Luis treated me more as a colleague than a student and that is extremely encouraging, especially at times when nothing seems to work.

I owe it all to my beloved wife Adrienne. She joined me for this adventure, thousands of miles away from family and old friends. Adrienne, thank you for being with me during all the difficult and all the easy times. Matéo, I had no idea how much energy can come from your smiles!

Chapter 1

Introduction

In this introduction, I give a birds-eye view of my work for the non-specialist. I highlight the important ideas and concepts, provide an intuitive explanation of the physics, leaving references, equations and details to the following chapters. I hope that most readers will be excited enough to read on to the end of the thesis.

1.1 What are coda waves?

The first waves we generally record after an earthquake are P-waves (primary) followed by S-waves (secondary) (Figure 1.1). As these body waves interact with the surface, some of their energy is transformed into surface waves. Surface waves have large amplitudes and reach the seismometer after the first arriving P and S waves. After that, the recorded amplitudes decrease steadily. This decaying wave-train after an earthquake is composed of a mixture of P, S and surface waves that arrive along scattered paths through the complex structure of the earth. It is this part of a seismogram that is called the coda. This word is used by analogy with the final section of a musical composition (Latin cauda, tail).

Although the word coda waves originated in the earthquake seismology community, its use does not have to be restricted to seismograph readings. Measurements from exploration seismology and ultrasonic laboratory experiments generally contain coda energy. Examples of ultrasonic coda measurements are given in Chapters 2 and 3, while Chapter 4 contains coda wave data from a hammer source seismic experiment and Chapter 5 includes earthquake data recorded at a volcano.

While we usually have a good understanding of the traveled paths and velocities of the first arriving P and S waves, our knowledge about coda waves is more limited. Unraveling the different wave modes and propagation paths forming the coda is in most cases not possible. We often can, however, explain part of it. A P-wave for example can bounce back and forth between two boundaries many times (Figure 1.2a). The P wave arrives at the receiver in constant time intervals, leaving a distinct pattern of wave arrivals in the coda measurement. I like to think of this as a bouncing ball mode. A second example is a phenomenon often seen in global seismology, where surface waves created by an earthquake circle the earth many times (Figure 1.2b), which leaves a distinct pattern in the coda energy as well. A more complex behavior is the multiple reflection from boundaries where the waves reflect in all directions in random fashion (Figure 1.2c), or the scattering from inhomogeneities within the medium of propagation (Figure 1.2d). In the last two examples, it is difficult to recognize a pattern in the coda measurement.

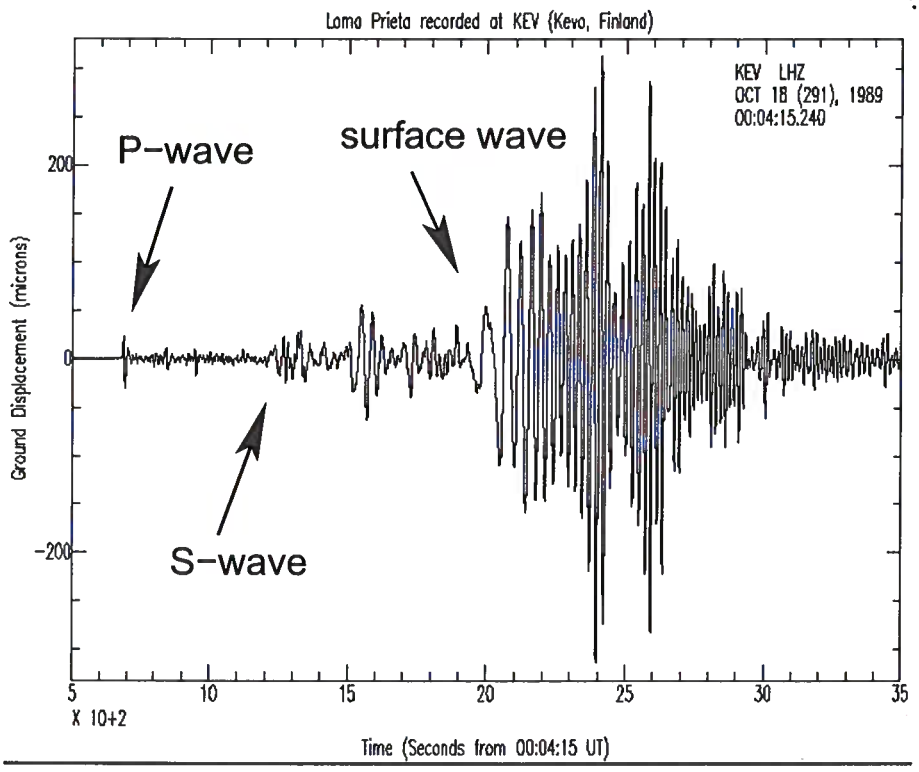

Figure 1.1. This seismogram shows the vertical motion of the earth in Kevo, Finland. The record begins at 500 seconds (8.3 minutes) after the earthquake occurred in Loma Prieta, California, near San Francisco. The first arrivals for P-, S- and surface waves are indicated by arrows.

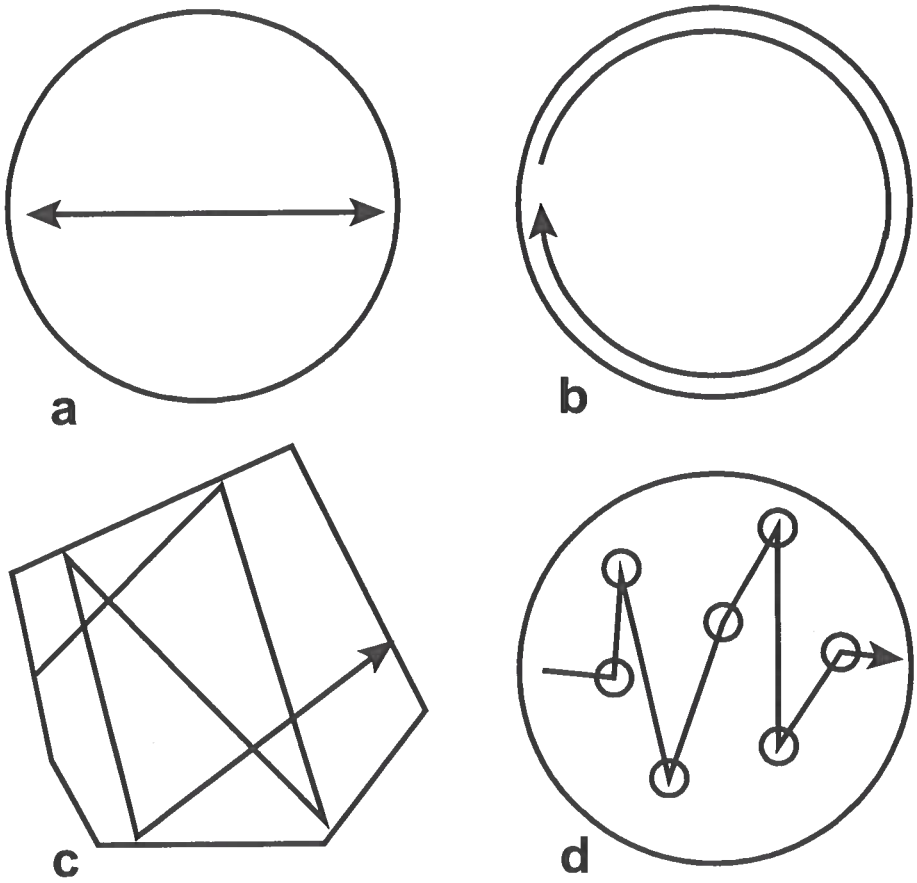

Figure 1.2. Cartoon of different wave modes that may co-exist in a medium. a) A bouncing ball mode where the waves go straight back and forth between two boundaries. b) Surface waves that propagate along the boundary, circling the medium. c) More complex reverberations between the boundaries. d) Multiple scattering from small-scale scatterers (small circles) in the medium.

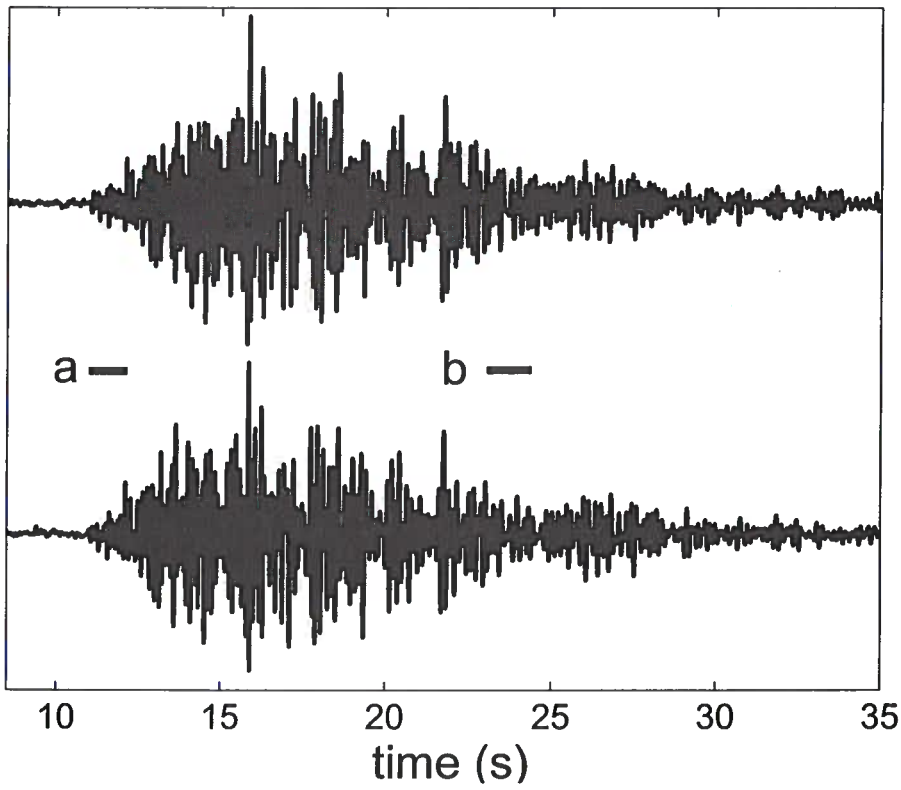

Figure 1.3. Two waveforms recorded at the Merapi volcano. The blue and the black lines represent two measurements taken at different days, two weeks apart in time. The two bars (a and b) indicate the position and duration of the time window shown in Figures 1.4 and 1.5.

In contrast to a wave that propagates in a direct path from source to receiver, coda waves travel along much longer and more complex trajectories. This long propagation path of coda waves is the key observation in order to understand Coda Wave Interferometry. A large part of chapter 6 is devoted to the discussion of path length and the increased sensitivity of coda waves due to long paths.

1.2 Reproducibility of coda waves

Coda Waves may have a noise appearance and are therefore often discarded by geophysicists in their analysis. They are, however, very different from random noise. In fact, there are many examples that show their high reproducibility. Figure 1.3 shows two seismic waveforms, recorded by Ulrich Wegler and colleagues from the University of Podsdam. The seismograms were recorded at the Merapi volcano in Indonesia. A repeatable source (air-

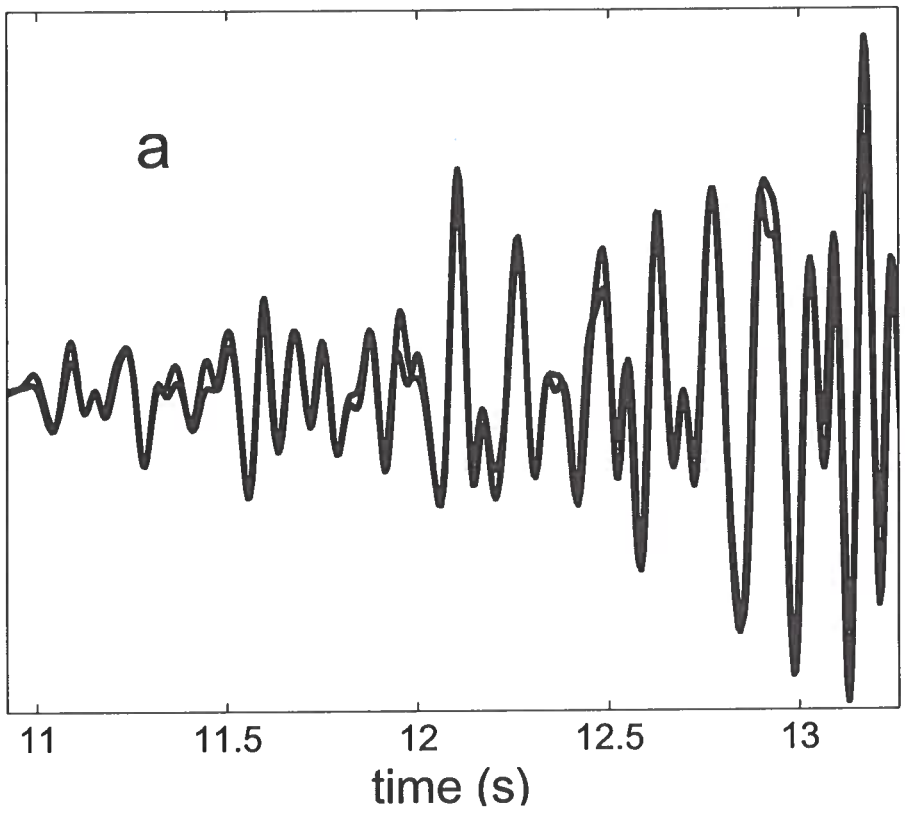

Figure 1.4. A short time window of the same data presented in Figure 1.3. For comparison, the two measurements are plotted on top of each other (blue and black lines represent the same measurements as in Figure 1.3).

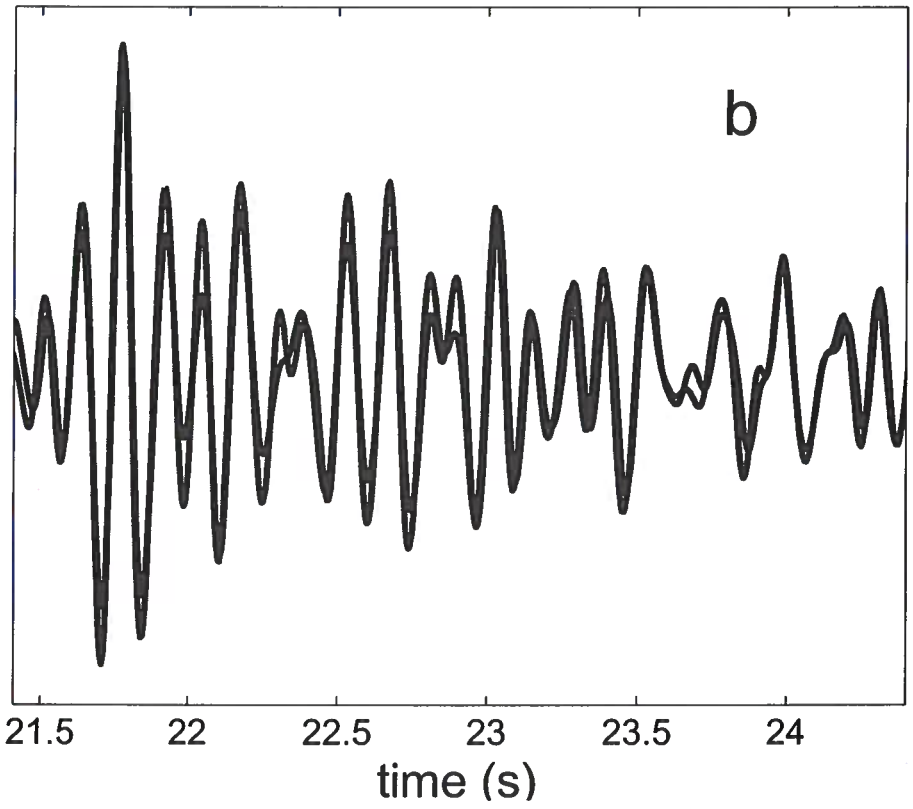

Figure 1.5. A short time window of the coda for the same data presented in Figure 1.3. For comparison, the two measurements are plotted on top of each other (blue and black lines represent the same measurements as in Figure 1.3).

gun in a water-pool) is fired and the resulting seismic signal is recorded by the seismometer located at the other side of the volcano. The blue line in Figure 1.3 shows the recorded waveform. One week later the air-gun is fired again, and the same seismometer, at the same location, records the resulting waveforms (black line in Figure 1.3). The two waveforms are almost identical. If we inspect the early part (first arriving waves) of the two measurements (Figure 1.4), we see the similarity even clearer. Furthermore, Figure 1.5 shows part of the coda of the two measurements and the waveforms match wiggle by wiggle. In other words, given a repeatable source at a fixed location, a fixed receiver, and nothing changes in the medium through which the waves propagate, the recorded signals remain identical, including the coda waves. Chapters 4 and 5 show other good examples of reproducible seismic coda measurements.

Evidently, seismic data contain random noise, which leads to differences in the measurements. In practice we may need to filter and/or average records to reduce noise. In a laboratory experiment, where we use ultrasonic waves, we can easily average hundreds or thousands of measurements within seconds. This results in data that are virtually noise free. The ultrasonic data used in Chapters 2 and 3 are such examples.

1.3 De-correlation of coda waves by changes in the medium

As long as we keep the source, receiver and medium traversed by the waves unchanged, we record an identical signal (up to random noise). Figure 1.6 shows the records for the seismic experiment at the Merapi volcano, discussed in the previous paragraph, but the time elapsed between the two records is now one year. As expected, the two waveforms are very similar. Comparing the early arriving waves (Figure 1.7), again displays the reproducibility of the measurement. Comparing the coda shown in Figure 1.8, however, shows that the waveforms don't match. Since we demonstrated the repeatability of the seismic source and the recording equipment in the previous paragraph, this difference in the coda can only originate from a change in the subsurface. An important observation is that one coda measurement is almost a time-shifted version of the other. We will later relate that time-shifts to differences in seismic velocity.

It is important to note that the two measurements are not completely different; their early part remains largely unchanged while the later arriving waves are altered. In other words, the change in the medium has little effect on the early arriving waves. These early arriving waves can therefore not be used to detect the change. The coda waves are, however, more sensitive to the change and can therefore be used to estimate the change in the medium. The increased sensitivity of coda waves as compared to that of the early arrivals can be explained by differences of the length of paths traversed by these waves. For example, a surface wave that circles the earth five times is five times more sensitive than a wave that only makes one trip around the globe. Chapter 6 is entirely devoted to the sensitivity question, both in time- and frequency domain measurements.

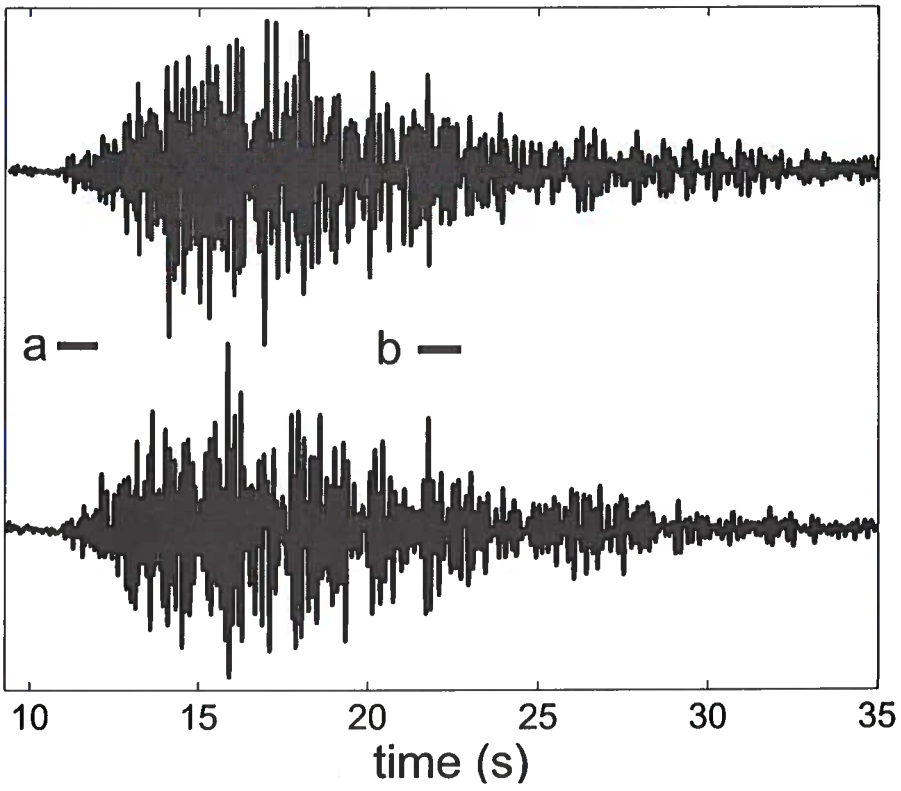

Figure 1.6. Two waveforms recorded at the Merapi volcano. The blue and the black lines represent two measurements taken at different days (one year apart). The two bars (a and b) indicate the position and duration of the time window shown in Figures 1.7 and 1.8.

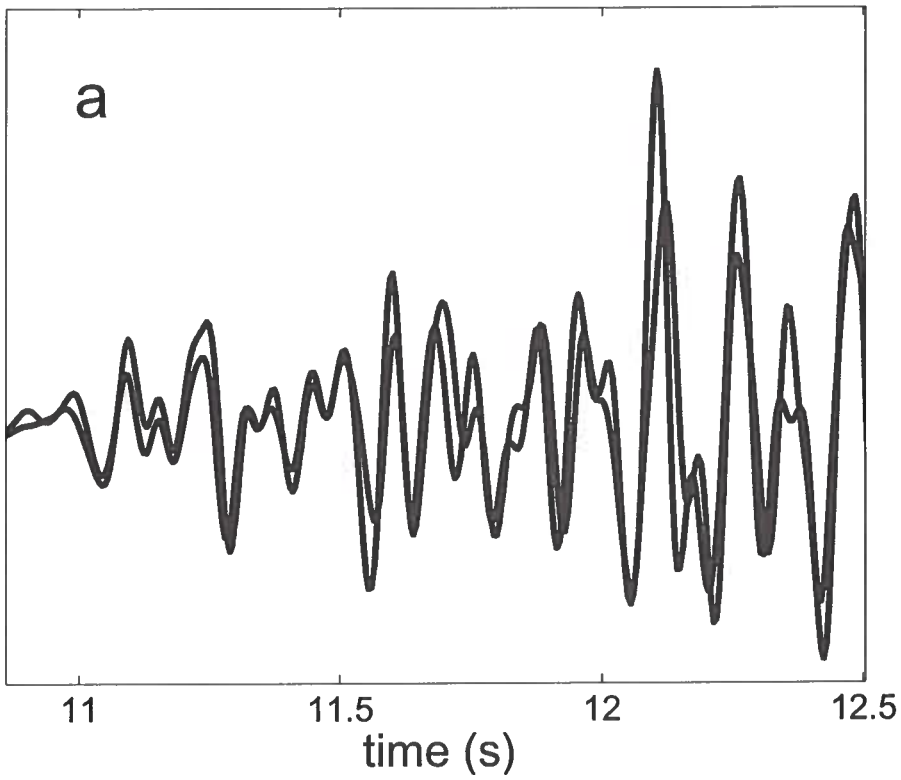

Figure 1.7. A short time window of the same data shown in Figure 1.6. For comparison, the two measurements are plotted on top of each other (blue and black lines represent the same measurements as in Figure 1.6).

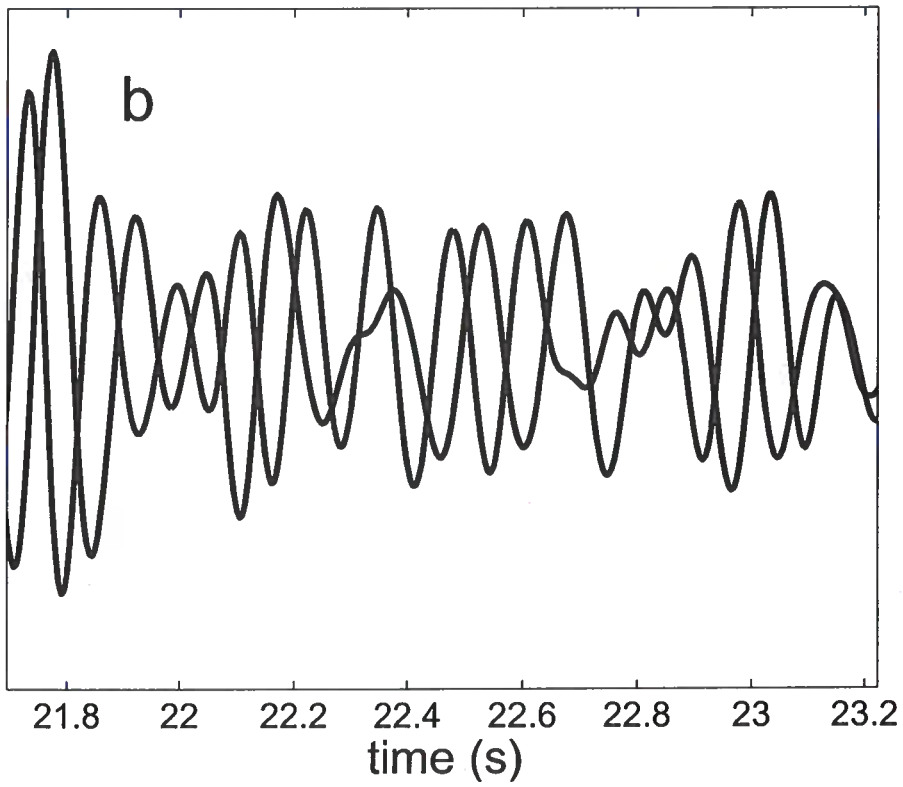

Figure 1.8. A short time window of the coda for the same data presented in Figure 1.6. For comparison, the two measurements are plotted on top of each other (blue and black lines represent the same measurements as in Figure 1.6).

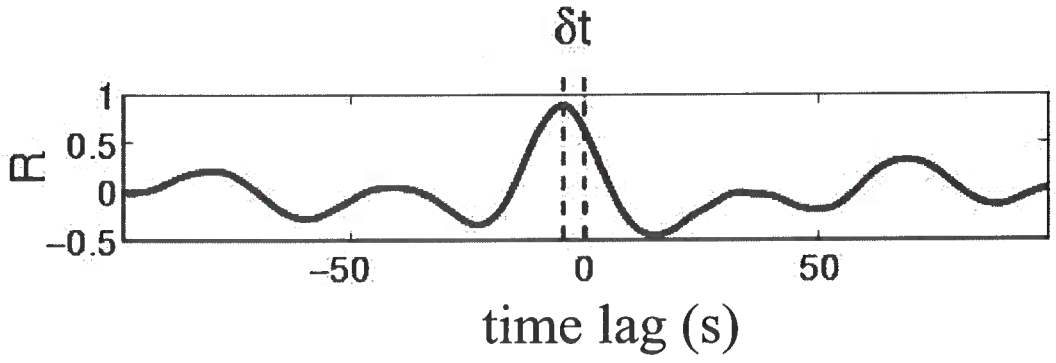

Figure 1.9. Cross-correlation function of the data shown in Figure 1.8. Note that the maximum of the cross-correlation function is centered at δt which is the value we try to estimate.

1.4 Cross-correlation function, the heart of coda wave interferometry

In the previous two paragraphs we have talked about waveforms that are identical, similar or different. But how do we quantify how similar or different these waves are? The tool of choice to compute the degree of similarity of two signals is the cross-correlation function (Figure 1.9).

The maximum of the cross-correlation function (R_{max}) characterizes how similar two signals are, where $R_{max} = 1$ means that they are identical. The time at the maximum (δt), is the time by how much the two signals have to be shifted with respect to each other to achieve the best possible match. We use R_{max} in Chapters 2 and 5, whereas we use δt in chapters 2, 3, 4 and 6 to monitor changes with Coda Wave Interferometry.

Note that it is this comparison of two waveforms, where one wave has propagated through an un-changed and one through a changed medium, which is similar to an interferometer, lending our method its name. Furthermore, an optical interferometer can be made more sensitive by lengthening the propagation path of the light, the Fabry-Perot interferometer is an example (6).

As explained in the previous paragraph, the sensitivity increases with path length. Similarly, there is a sensitivity increase with total travel time (twice around the globe takes twice as long than going around once). In order to compare waves that have similar sensitivity, we compare small parts of the whole signal by computing R_{max} and δt for different time windows.

1.5 Velocity changes

Often we can extract information about changes in a medium by monitoring the velocity of wave propagation. I explain the main idea in the following toy example. Figure 1.2b is a sketch of a surface wave that circles the medium repeatedly. What we would record at a fixed point on the boundary, is a series of surface waves arriving in constant time intervals (Figure 1.10). If we reduce the velocity in the medium and repeat the experiment, we measure a similar series of surface waves but with a lower velocity as it takes the wave longer to make one round-trip and arrives at the receiver with a time lag δt. The wave that circles twice has a time lag $2\delta t$, the one that makes three trips $3\delta t$ and so forth (Figure 1.10a). We can estimate the time lag from the data by means of the cross-correlation function in a time window centered around the arrival of one wave. It is important to note that the velocity decrease might be too small to be detected by a wave that samples the medium once, but as time elapses the lag becomes larger and larger (Figure 1.10b). If the propagation path before and after the velocity change remains fixed, the relative time lag ($\delta t/t$) is a direct measure of the relative velocity change ($\delta v/v$). In chapters 2, 3, 4 and 6, I show how we can use this coda wave interferometry to monitor relative velocity changes, in applications that range from small rock samples in the laboratory to seismic waves in a gold and silver mine.

For all the applications of coda wave interferometry described in this thesis, we assume a homogeneous change in the whole medium. In other words we gain sensitivity at the

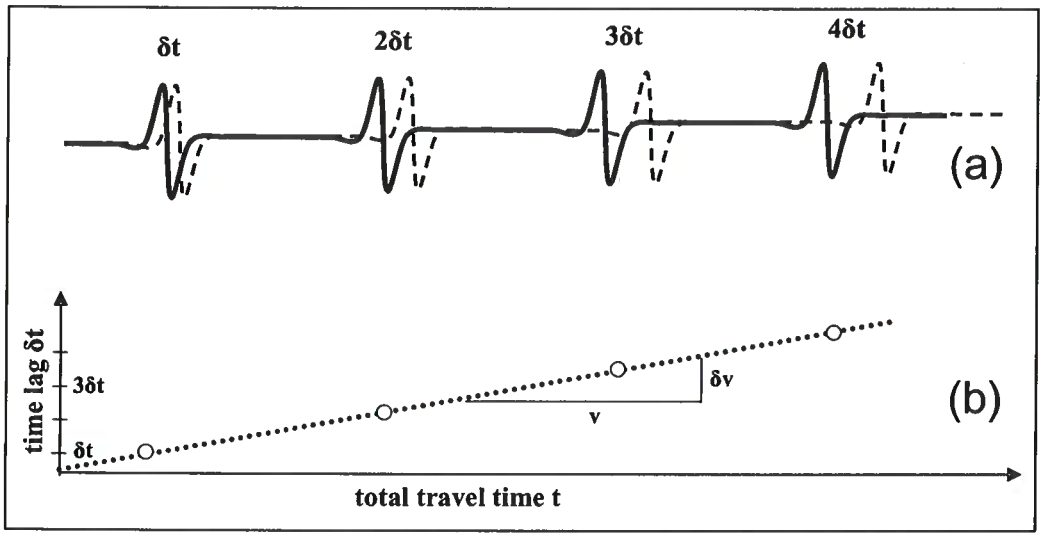

Figure 1.10. (a) Sketch of a surface wave that circles the medium repeatedly. The measured wave-train consists of a series of surface waves arriving in constant time intervals. Waves before (solid line) and after the velocity change (dashed line). (b) A change in velocity leads to a shifting of the wave-trains, where the shift becomes larger with increasing time.

expense of spatial resolution. This is certainly, however, not always a good approximation. Some arguments of how we can check weather or not the change occurs in the entire medium are given in Chapter 4. Furthermore, Pacheco & Snieder (2003) developed a theoretical extension to coda wave interferometry that allows the spatial localization of the changed area, based on multiply scattered waves.

1.6 Applications

As described in the previous paragraphs, we can use coda wave interferometry to monitor small changes in a medium. In Chapters 2 through 5 we monitor changes at the laboratory scale up to the scale of monitoring a volcano. In this paragraph I give a preview of the applications described in the corresponding chapters.

Ultrasonic wave velocity in solids depends on temperature. In most cases, the velocity decreases with an increase in temperature. We use this in Chapters 2 and 3 where we introduce a controlled velocity change in aluminum and granite samples. We alter the temperature of the samples and monitor the associated velocity change with coda wave interferometry. In contrast to aluminum, where we find a linear dependence of velocity on temperature, we observe non-linear dependence of velocity on temperature in granite. This can be attributed to internal cracking that produces acoustic emissions. The cracking causes an irreversible damage as the granite is heated and cooled.

In addition to the temperature dependence of ultrasonic velocity, we study the effects of water saturation and stress change on the velocity in Berea sandstone (Chapter 3). There are many potential applications for coda wave interferometry in rock physics. Deformation, phase change of fluids, compaction of granular materials, and steam injection are a few examples of changes that can be monitored with coda wave interferometry.

Stress change, and deformation are important in mining hazard and safety applications. Inspired by the stress change experiment in the laboratory, we conducted a hammer source seismic experiment in an underground mine (Chapter 4). We introduced a controlled internal stress change in a rock pillar with a hydraulic pressure cell introduced into the rock formation. We monitor internal stress changes in the rock pillar with coda wave interferometry. The method can be used to monitor the rate of stress change and deformation in the rock mass around excavations, both in underground and surface mines.

Volcanoes are known for their highly complex subsurface, which often results in the multiple scattering of waves that propagate through the volcano's underground. At Mt. Erebus (Antarctica), eruptions of a lava lake located in the volcano's crater acts as a repeatable seismic source. The earthquakes recorded at a seismic network around the volcano contain a highly reproducible coda. We use these multiply scattered coda waves to monitor a rapid temporal change in the subsurface of the volcano (Chapter 5).

Waves that follow a distinct pattern of propagation (Figure 1.2), can be viewed either as modes or as traveling waves, the modes and the traveling waves are complementary views of the wave propagation. In resonance spectroscopy such modes are excited and the frequency response is measured. This is a purely frequency domain measurement that has similarities with coda wave interferometry, which is a time domain technique. In chapter 6, we discuss the similarities and differences between the two techniques, with a particular focus on the comparison of the sensitivity to detect changes.

With all the applications of coda wave interferometry included in this thesis, we only cover the most basic aspects, in the sense that each application could be explored in much greater depth, and independently be the topic of a Master or Ph.D. thesis. The in-depth study of velocity change due to temperature on the basis of intra molecular bonding or the mechanics and physics of crack formation between crystal boundaries in rocks are only two examples. It is the focus of this thesis to study the feasibility of this technique to a variety of applications, with the hope that it leads to future research projects.

1.7 Similar methods

Diffusive wave spectroscopy or acoustic diffusive wave spectroscopy in particular, is a technique similar to coda wave interferometry. In contrast, it uses the diffusion approximation to model the wave-field. We do not make that requirement in coda wave interferometry, but only assume that the coda wave, sample the medium multiple times.

Cavity ring-down spectroscopy is a technique in optics, which is often used in atmospheric pollution analysis and optical probing of flames. A laser pulse bounces back and fourth between two mirrors, sampling the medium between the mirrors multiple times (similar to Figure 1.2a). Analogous to coda wave interferometry, the method makes use of the

fact that the signal is directly proportional to the length of the path traveled by the laser light. In cavity ring-down spectroscopy the geometry of the optical cavity (space between the mirrors) is known and used to compute an absolute velocity or absorption value of the medium in the cavity. In contrast, coda wave interferometry compares a measurement before with a measurement after a change, resulting in a relative quantity. This has the advantage that we do not need any knowledge about the geometry of the propagated paths.

1.8 The coda wave interferometry bunch

Many Researchers have been working on coda wave interferometry projects, which greatly inspired, influenced and helped my work. In this section I give a short list of the different projects and at the same time I want to thank the whole group for helping me with my research.

Roel Snieder and Huub Douma laid the foundation with the theory and numerical simulations. They showed how we can extract information about the change in scatterer location from coda waves (Snieder & Douma, 2000). Furthermore, Huub Douma worked on the change in scatterer strength and Roel Snieder developed an extension for elastic waves (Snieder, 2002) and used coda wave interferometry to monitor changes in volcanic interiors (Snieder & Hagerty, 2004). Carlos Pacheco's masters thesis shows how we can detect a localized change with coda wave interferometry (Pacheco, 2003) and Mark Vrijlandt used coda wave interferometry to constrain the relative source location of earthquake doublets (Snieder & Vrijlandt, 2004).

1.9 Data contributions

The ultrasonic data I used to monitor uni-axial stress on Berea sandstone (chapter 3) where recorded by Debashish Sarkar and Robert Kranz (Sarkar *et al.*, 2003). Rick Aster from New Mexico Tech, Socorro, NM, provided the seismic data, that we use to monitor rapid changes in the subsurface of the Mt. Erebus Volcano (chapter 5).

1.10 A collection of papers

Chapters 2 through 6 are published or submitted to scientific peer-reviewed journals.

- Chapter 2: Coda Wave Interferometry for Estimating Nonlinear Behovior in Seismic Velocity, Science 2002, by Roel Snieder, Alexandre Grêt, Huub Douma and John Scales.
- Chapter 3: Time-Lapse Monitoring of Rock Properties with Coda Wave Interferometry, submitted to the Journal of Geophysical Research 2004, by Alexandre Grêt, Roel Snieder and John Scales.
- Chapter 4: Monitoring Stress Change in an Underground Mining Environment with Coda Wave Interferometry, submitted to Mining Engineering 2004, by Alexandre Grêt, Roel Snieder and Ugur Ozbay.

- Chapter 5: Monitoring Rapid Temporal Changes in a Volcano with Coda Wave Interferometry, submitted to Geophysical Research Letters 2004, by Alexandre Grêt, Roel Snieder and Rick Aster.
- Chapter 6: Time-Domain versus Frequency-Domain Resolution of Small Changes, submitted to American Journal of Physics 2004, by Brian Zadler, Alexandre Grêt and John Scales.

Chapter 2

Coda Wave Interferometry for Estimating Nonlinear Behavior in Seismic Velocity

2.1 Abstract

In coda wave interferometry one records multiply scattered waves, at a limited number of receivers, to infer changes in the medium over time. With this technique we have determined the nonlinear dependence of the seismic velocity in granite on temperature and the associated acoustic emissions. This technique can be used in warning mode, to detect the presence of temporal changes in the medium, or in diagnostic mode, where the temporal change in the medium is quantified.

2.2 Introduction

In many applications, such as non-destructive testing, monitoring of volcanoes or radioactive waste disposal sites, one is primarily interested in detecting temporal changes in the structure of the medium. Temporal changes in Earth's structure accompanying earthquakes have been observed based on the attenuation of coda waves (Chouet, 1979; Aki, 1985; Sato, 1986; Got *et al.*, 1990), on the arrival times of the directly arriving waves (Leary *et al.*, 1979), on velocity changes inferred from later arriving waves (Poupinet *et al.*, 1984; Ratdomopurbo & Poupinet, 1995; Dodge & Beroza, 1997; Li *et al.*, 2000; Snieder & Douma, 2000) (see also (Roberts *et al.*, 1992)), and on changes in seismic anisotropy (Bokelmann & Silver, 2002; Miller & Savage, 2001). Here we introduce coda wave interferometry whereby multiply scattered waves are used to detect temporal changes in a medium by using the scattering medium as an interferometer. For quasi-random perturbations of the positions of point scatterers, or for a change in the source location, or for a change in the wave velocity, estimates of this perturbation can be derived from multiply scattered waves by a cross-correlation in the time domain.

In the numerical example (Figure 2.2), the wave-field for a medium consisting of isotropic point scatterers is computed using a deterministic variant (Groenenboom & Snieder, 1995; Snieder & Scales, 1998) of Foldy's method (Foldy, 1945). Given the mean free path ($l = 20.1$ m) and the wave velocity ($v = 1,500$ m/s) one can infer that after $t = 5.4 \times 10^{-2}$ s the waves are on average scattered more than three times. The later part of the signal is called the *coda*. Suppose that one repeats this multiple scattering experiment after the scatterer locations are perturbed. The perturbation in the scatterer location 1/30 of the

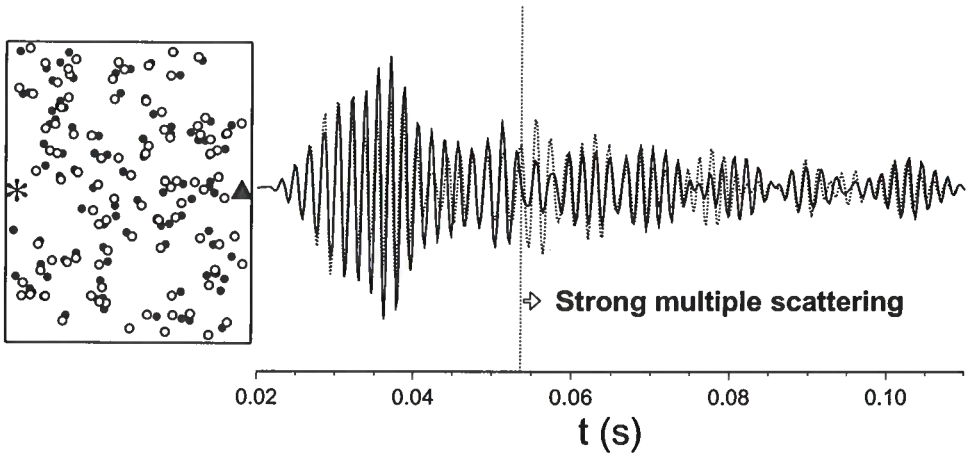

Figure 2.1. Location of 100 scatterers before and after the perturbation (filled dots and open dots respectively) with the source (asterisk) and receiver location (triangle). For the sake of clarity the scatterer displacement is exaggerated with a factor 40. The scatterers are placed in an area of 40×80 m. The waveforms recorded before and after the perturbation at the receiver are shown on the right with a solid and dashed line respectively.

dominant wavelength and is uncorrelated between scatterers (Maret & Wolf, 1987; Heckmeier & Maret, 1997).

In this example the scatterers locations are perturbed. In general, a perturbation can involve other changes in the medium or a change in source location. We refer to the waveform before the perturbation as the unperturbed signal, and to the waveform after the perturbation as the perturbed signal. For early times ($t < 0.04$ s) the waves in Figure 2.2 have not scattered often, rendering the path lengths of these waves insensitive to the small perturbations of the scatterers (small compared to the dominant wavelength $\lambda = 2.5$ m), which causes the unperturbed and perturbed signals to be similar. However, the multiply scattered waves are increasingly sensitive with time to the perturbations of the scatterer locations because the waves bounce more often among scatterers as time increases. The correlation between the unperturbed and perturbed signals therefore decreases with increasing time.

2.3 Coda wave interferometry

The perturbation in the medium can be retrieved from the cross-correlation of the coda waves recorded before and after the perturbation. The unperturbed wave-field can be

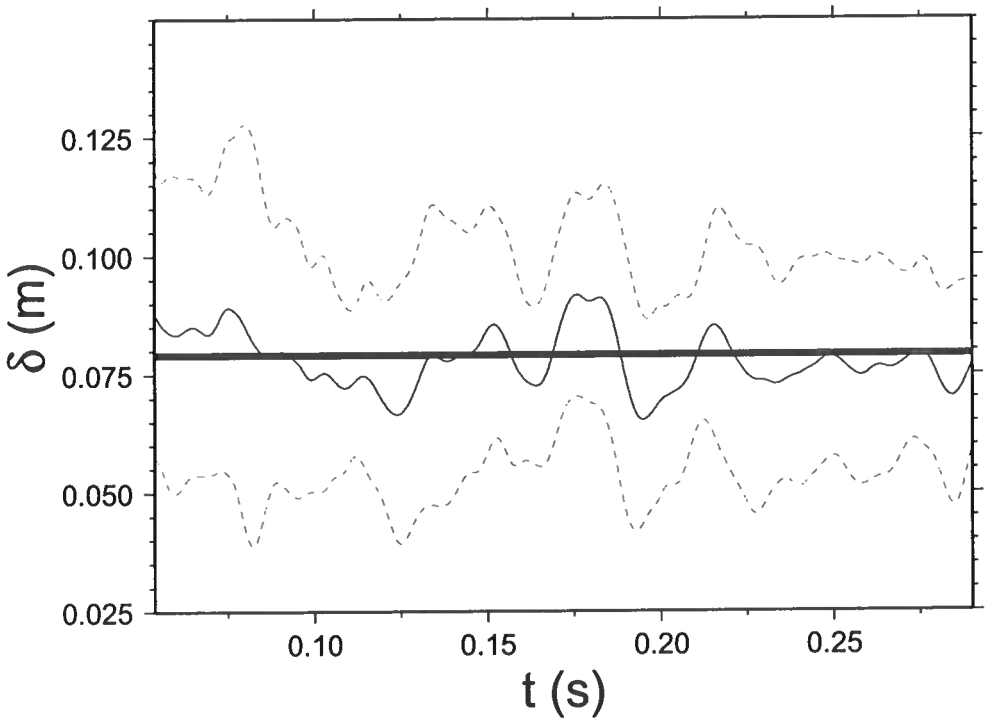

Figure 2.2. The value of δ obtained from the time-windowed cross correlation of the wave forms in Figure 2.2 and of 20 other receivers as a function of the center time t of the time window (solid line) plus or minus one standard deviation (dotted lines) for $T = 2 \times 10^{-2}$ s. The true root mean square displacement value $\delta_{true} = 8 \times 10^{-2}$ is shown by the horizontal solid line.

written as a Feynman path summation (Snieder, 1999) over all possible paths P:

$$u_{unp}(t) = \sum_P A_P S(t - t_P) \, , \tag{2.1}$$

where a path is defined as a sequence of scatterers that is encountered, t_P is the travel time along path P, A_P is the corresponding amplitude and $S(t)$ is the source wavelet. When the perturbation of the scatterer locations (or source location) is much smaller than the mean free path, the effect of this perturbation on the geometrical spreading and the scattering strength can be ignored and the dominant effect on the waveform arises from the change in the travel time τ_P of the wave that travels along each path:

$$u_{per}(t) = \sum_P A_P S(t - t_P - \tau_P) \, . \tag{2.2}$$

The time-windowed correlation coefficient is computed from:

$$R^{(t,T)}(t_s) \equiv \frac{\int_{t-T}^{t+T} u_{unp}(t') u_{per}(t' + t_s) dt'}{\left(\int_{t-T}^{t+T} u_{unp}^2(t') dt' \int_{t-T}^{t+T} u_{per}^2(t') dt' \right)^{1/2}} \, , \tag{2.3}$$

where the time window is centered at time t with duration $2T$ and t_s is the time shift used in the cross-correlation. When equations (2.1) and (2.2) are inserted, double sums $\sum_{PP'}$ over all paths appear. In these double sums, the cross-terms with different paths ($P \neq P'$) are incoherent and average out to zero when the mean of the source signal vanishes. This means that in this approximation:

$$R^{(t,T)}(t_s) \approx \frac{\sum_{P(t,T)} A_p^2 C(\tau_P - t_s)}{\sum_{P(t,T)} A_p^2 C(0)} \, , \tag{2.4}$$

where $\sum_{P(t,T)}$ denotes a sum over the paths with arrival times within the time window of the cross-correlation, and the auto-correlation of the source signal is defined as $C(t) \equiv \int_{-\infty}^{\infty} S(t' + t) S(t') dt'$.

For time shifts τ much smaller than the dominant period, a second-order Taylor expansion gives $C(\tau) = C(0) \left(1 - \frac{1}{2} \bar{\omega}^2 \tau^2 \right)$, where $\bar{\omega}^2$ is the mean-squared frequency of the multiply scattered waves that arrive in the time window. Using this gives

$$R^{(t,T)}(t_s) = 1 - \frac{1}{2} \bar{\omega}^2 \left\langle (\tau - t_s)^2 \right\rangle_{(t,T)} \, , \tag{2.5}$$

where $\langle \cdots \rangle_{(t,T)}$ denotes the average for the wave paths with arrivals in the time interval $(t - T, t + T)$.

The time shifted cross correlation $R^{(t,T)}(t_s)$ has a maximum when

$$t_s = \langle \tau \rangle_{(t,T)} \, , \tag{2.6}$$

where $\langle\tau\rangle_{(t,T)}$ is the mean travel time perturbation of the arrivals in the time window. The value of the cross correlation at its maximum is given by

$$R_{max}^{(t,T)} = 1 - \frac{1}{2}\bar{\omega}^2\sigma_\tau^2 \,, \tag{2.7}$$

with σ_τ^2 the variance of the travel time perturbations for waves arriving within the time window. This means that the mean and the variance of the travel time perturbation of the waves arriving in the employed time window can be extracted from the data recorded with a repeatable source, and one or more receivers.

Different types of perturbations leave a different imprint on the time shifted correlation coefficient. When the scatterer locations are perturbed independently with root mean square displacement δ, the mean travel time perturbation vanishes ($\langle\tau\rangle_{(t,T)} = 0$) and the variance is given by (Snieder, 1999)

$$\sigma_\tau^2 = \frac{2\delta^2 t}{v l_*} \,, \tag{2.8}$$

where l_* is the transport mean free path (Maret, 1995; Lagendijk & van Tiggelen, 1996). In deriving (2.8) we assume that the number of scatterers encountered is on average given by $n = vt/l$, where t is the time that the wave has spent in the scattering medium. Using (2.7) and (2.8), the root mean square perturbation of the scatterer location follows from the maximum of the time-windowed correlation coefficient:

$$\delta^2 = \left(1 - R_{max}^{(t,T)}\right) \frac{v l_*}{\bar{\omega}^2 t} \,. \tag{2.9}$$

A different type of perturbation is a constant change δv in the velocity for fixed locations of the scatterers. The mean travel time perturbation is given by $\langle\tau\rangle_{(t,T)} = -(\delta v/v)t$, and when the time window is small ($T \ll t$), $\sigma_\tau = 0$. The velocity change follows from the time of the maximum of the time-shifted cross correlation function:

$$\frac{\delta v}{v} = -\frac{t_{max}}{t} \,. \tag{2.10}$$

When the perturbation consists of a displacement of the source location over a distance δ for a fixed medium, only the wave-path to the first scatterer is perturbed. In that case the mean travel time perturbation vanishes $\langle\tau\rangle_{(t,T)} = 0$ and for an isotropic source the variance is given by $\langle\sigma_\tau^2\rangle = (\delta/v)^2$. The source displacement then follows from

$$\delta^2 = \left(2v^2/\bar{\omega}^2\right)\left(1 - R_{max}^{(t,T)}\right) \,. \tag{2.11}$$

These different perturbations can be distinguished on the basis of the time shifted cross correlation. When the positions of the scatterers are perturbed, the mean travel time perturbation vanishes and the maximum of the cross correlation decreases linearly with increasing time, whereas for the perturbation of the source position the maximum value of this function is independent of time. A change in the velocity is detectable by a shift in the position of the maximum of $R^{(t,T)}(t_s)$ that increases linearly with time.

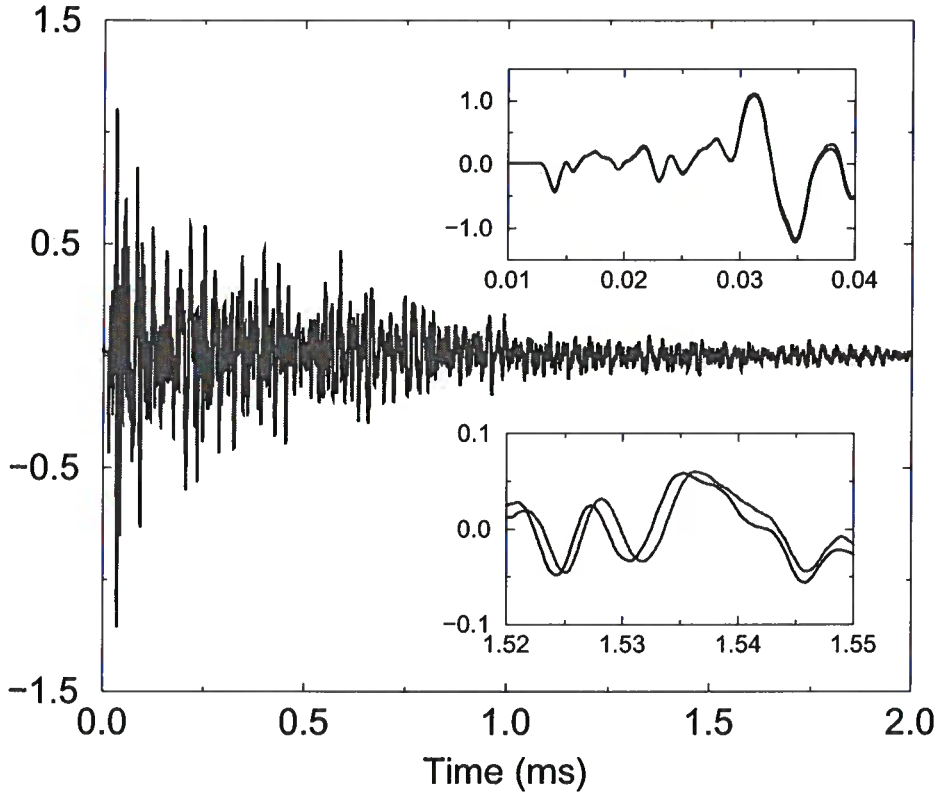

Figure 2.3. Wave-forms recorded in the granite sample for temperatures of $45°C$ (in blue) and $50°C$ (in red) respectively. The insets show details of the wave-forms around the first arrival (top) and in the late coda (bottom).

The root mean square displacement of the scatterers inferred from the numerical example (Figure 2.2) is shown in Figure 2.3 as a function of the center time t of the time window. The inferred change δ in the scatterer location does not depend on the center time of the window used for the cross correlation. This provides a consistency check of the method.

2.4 Laboratory experiment

The extreme sensitivity of the coda waves to changes in the medium is used here in a laboratory experiment to infer the temperature dependence of the seismic velocity in Elberton granite. In many experiments, the change in the seismic velocity in rock samples

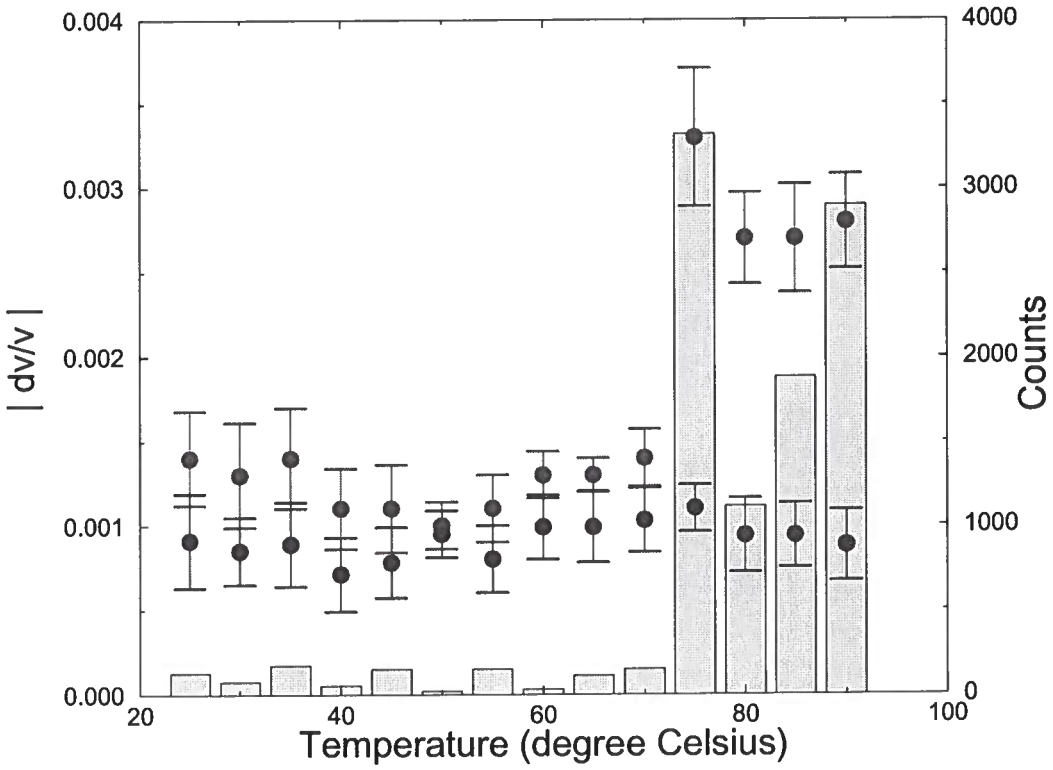

Figure 2.4. The absolute value of the relative velocity change for a $5°C$ increase (red symbols) and $5°C$ decrease (blue symbols) respectively as a function of the highest temperature during the change. The histograms shows the count of acoustic emissions.

is measured for a temperature change of about $100°C$ (Hughes & Maurette, 1956; Peselnick & Stewart, 1975; Kern *et al.*, 2001). In our experiment a cylindrical sample of granite with a height of 110 mm and a diameter of 55 mm was heated with a heating coil inside the sample from $20°C$ to $90°C$ and cooled down to room temperature. The heating and cooling phase took about 8 hours each. Two piezo-electric transducers were used to excite and record elastic waves in the sample with a dominant frequency of about 100 kHz. The waveforms were recorded after each $\pm 5°C$ change in temperature. In order to reduce the influence of ambient noise the wave-forms were stacked over 10 shots. A third transducer was used to monitor the acoustic emissions in the sample.

The difference in the early part of the wave-forms recorded at temperatures of $45°C$ and $50°C$ (Figure 2.4) are small. This change in temperature does not affect the first arrival, which means that the travel time of the first arrival cannot be used to infer any possible small change in velocity due to a $5°C$ temperature difference. The late time window (bottom inset) shows a clear time shift of the wave-forms.

For each change of $\pm 5°C$ in temperature the change in the velocity is inferred from equation (2.10) using 20 different time windows of the coda waves with a duration of 0.1 ms each. The mean and variance of the velocity change (Figure 2.4) is inferred from the estimates of the the velocity change in the different time windows. The relative velocity change is of the order of 0.1% for a temperature change of $\pm 5°C$ with an error of about 0.02%.

During the heating phase the velocity change is constant for temperatures less than $75°C$. Above that temperature the velocity change during heating increases (Figure 2.4). The acoustic emissions correlate with the increased value of the velocity change at $75°C$ (Yong & Wang, 1980). During the cooling phase the velocity change is constant, and there are no acoustic emissions. When the sample is heated again to a temperature of $90°C$ the velocity change does not increase dramatically around $75°C$ and there are no acoustic emissions (Ide, 1937). In order to test whether the transducer coupling and the presence of the heating coil played a role we repeated the experiment with an aluminum sample. In that case the velocity change is constant both during heating and cooling.

The acoustic emissions and the change in the velocity gradient occur only in a pristine sample during heating (the Kaiser effect (Yong & Wang, 1980) and are due to the irreversible formation of fractures by differential thermal expansion (Meredith *et al.*, 2001) of the minerals in the sample. This indicates that the velocity change is due to two different mechanisms. The first is a reversible change in velocity due to the change in bulk elastic constants with temperature. The second mechanism is associated with irreversible changes in the sample that generate acoustic emissions. The damage done to the sample leads to a greater change in the seismic velocity with increasing temperature.

These measurements could be carried out because of the extreme sensitivity of coda wave interferometry to changes in the medium. This makes it possible to infer the nonlinear dependence of the velocity on temperature that is associated with irreversible damage to the granite sample.

2.5 Acknowledgments

We thank Robert Kranz and Mike Batzle for their help and advice. This work was partially supported by the NSF(EAR-0106668 and EAR-0111804), by the US Army Research Office (DAAG55-98-1-0070), and by the sponsors of the Consortium Project on Seismic Inverse Methods for Complex Structures at the Center for Wave Phenomena.

Chapter 3

Time-lapse Monitoring of Rock Properties with Coda Wave Interferometry

3.1 Abstract

The coda of seismic waves consists of that part of the signal after the directly arriving phases. In a finite medium, or in one that is strongly heterogeneous, the coda is dominated by waves which have repeatedly sampled the medium. Small changes in a medium which may have no detectable influence on the first arrivals are amplified by this repeated sampling and may thus be detectable in the coda. We refer to this use of multiple-sampling coda waveforms as *coda wave interferometry*. We have exploited ultrasonic coda waves to monitor time-varying rock-properties in a laboratory environment. We have studied the dependence of velocity on uni-axial stress in Berea sandstone, the temperature dependence of velocity in granite and in aluminum, and the change in velocity due to an increase of water saturation in sandstone. There are many other possible applications of coda wave interferometry in geophysics, including dam and volcano monitoring, time-lapse reservoir characterization, earthquake relocation, stress monitoring in mining and rock physics.

3.2 Introduction

Geophysicists investigate the structure of the subsurface by making indirect measurements on the surface and relating them to those predicted by theoretical Earth models. The Earth, however, is a highly complex system, and we almost always have to simplify our models in order to make them tractable. In many applications, this simplification means treating unmodeled physics as noise, with the result that information contained in the data is discarded. For seismic data, this typically means ignoring the coda waves that make up the tail of a seismogram. (In music the coda is the concluding passage of a movement or composition (Latin *cauda*, tail).) Geophysical applications based on use of the coda waves include proposed schemes for earthquake prediction (Aki, 1985; Sato, 1988), volcano monitoring (Poupinet *et al.*, 1984; Ratdomopurbo & Poupinet, 1995; Fehler *et al.*, 1998; Aki & Ferrazzini, 2000) or monitoring of temporal changes in the subsurface (Chouet, 1979; Revenaugh, 1995; Baisch & Bokelmann, 2001; Niu *et al.*, 2003).

Consider the following examples: in monitoring a nuclear waste disposal site, one is not primarily interested in imaging the site. It is, however, critical to monitor temporal changes in the site. In recent years, applied geophysicists have spent much effort on time-lapse

seismology to monitor hydrocarbon reservoirs during recovery operations. Hydrocarbons move in the subsurface, reservoir rocks are artificially fractured, water-oil horizons move and injected steam propagates through the reservoir (Lumley, 1995; Wang, 1997). The high sensitivity of coda waves to small perturbations of the medium makes them a powerful tool to monitor these kinds of changes.

We present four laboratory experiments in which we monitor the change in seismic velocity resulting from (i) a change in uni-axial stress in a sample of Berea sandstone, (ii) a change in water saturation in a sample of Berea sandstone, (iii) a temperature change in a sample of aluminum and (iv) in a sample of Elberton granite. We excited and record ultrasonic waves to extract the velocity change from the coda waves.

3.3 Sensitivity of coda waves

In a tomographic transmission experiment, the area under investigation is usually sampled once. The traversing waves have a certain sensitivity to a velocity change in this area (depending on distance, velocity and sampling). In a coincident-source-receiver reflection experiment the area traversed by the waves is sampled twice and is therefore twice as sensitive to a velocity change than in the transmission case. Hence, in a setup where a wave is bouncing back and forth, and samples the same area multiple times, the wave is much more sensitive to a velocity change. This amplification of a velocity change, due to the multiple sampling of the same area is the key idea we use in this research.

Figure 3.1 outlines some examples of wave propagation where multiple sampling of the same area is achieved. In figure 3.1a the waves bounce back and forth between opposite boundaries of the medium, we think of this as a "bouncing ball mode." In the laboratory experiment where we monitor a velocity change due to a change in uni-axial stress, we record a wave field which is dominated by such a bouncing ball mode (see "Monitoring uni-axial stress in Berea sandstone"). In figure 3.1b surface waves sample the medium by circling around the boundary, they are influenced by the velocity change each time they encircle the medium. Because of the cylindrical symmetry of the samples, surface waves dominate the coda in the experiment where we monitor temperature in aluminum and granite (see "Monitoring thermally induced velocity changes in aluminum" and "Monitoring thermally induced change and acoustic emissions in granite"). In figure 3.1c waves propagate in a more complex manner, bouncing off the boundaries in a complex pattern. Because of the irregular shape of the sandstone sample in the experiment where we monitor water saturation, we record such complex waveforms (see "Monitoring water saturation in Berea sandstone").

If the medium under investigation contains many small-scale scatterers, and the wave follows a path that connects these scatterers (figure 3.1d), then the scattered path is much longer than the direct path from source to receiver. Hence the scattered wave is more sensitive to a velocity change than the direct wave. Examples of such scatterers in a background medium are colloidal suspensions, aerosols in air, and grains in rock.

In a laboratory environment it is difficult to avoid waves that repeatedly sample the medium, because the samples are of finite size. The associated repeated sampling (as in Figure 3.1a) lends itself naturally to a modal (i.e. resonance) analysis, as shown for rock

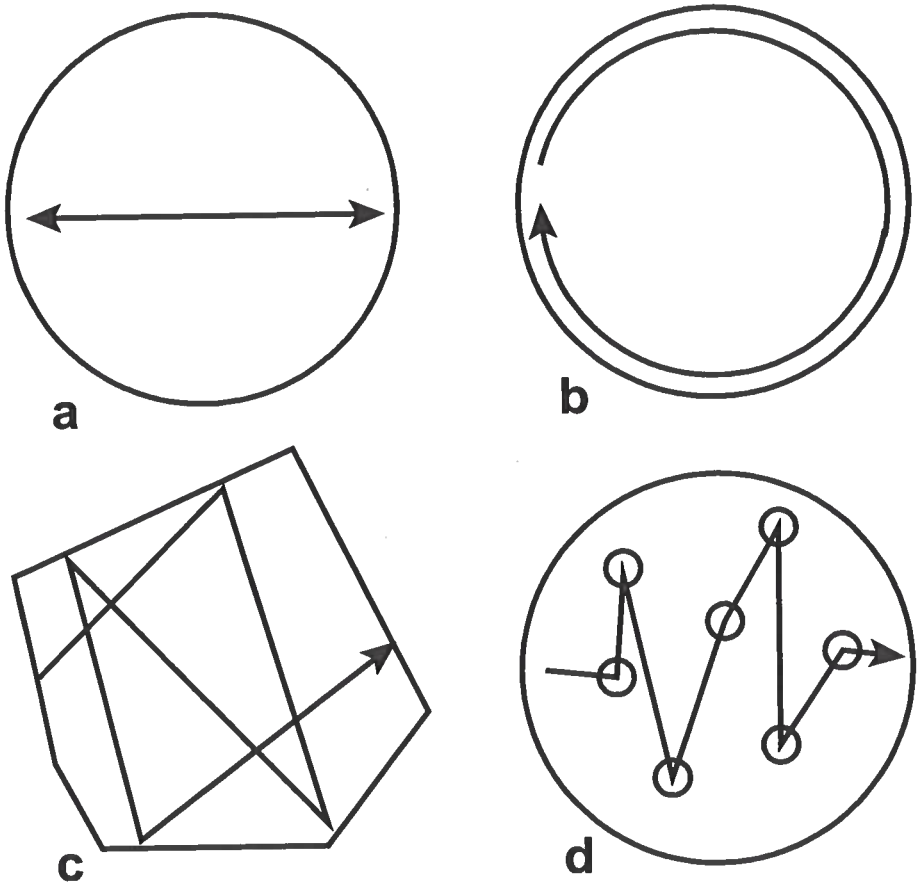

Figure 3.1. Cartoon of different wave modes that may co-exist in a medium. a) A bouncing ball mode where the waves go straight back and forth between two boundaries. b) Surface waves that propagate along the boundary, circling the medium. c) More complex reverberations between the boundaries. d) Multiple scattering from small-scale scatterers (small circles) in the medium.

cores by Scales & Malcolm (2003). Modal analysis is used in long period seismology (e.g., Dahlen & Tromp, 1998)) and resonance spectroscopy (McSkimmin, 1964; Zadler *et al.*, 2004). The power of resonance comes from the ability to use frequency to selectively excite certain waves (e.g., a bouncing ball modes), and from Rayleigh's Principle (Rayleigh, 1896, chap. 88) which states that the perturbation in the squared eigenfrequency of a mode can be related to perturbations in the density and elastic moduli, involving only the *unperturbed* mode vectors.

In field situations, however, there will likely be many scenarios where no modes can be excited (Figure 3.1d). In those situations, coda wave interferometry can still be applied as well as in the case where modes are excited.

This sensitivity increase with longer path length is extensively used in optical applications, for example in atmospheric pollution analysis. In this application, air is introduced into a long tube. A laser pulse propagates trough the tube parallel to the long axis of the tube, and is measured at the other end. The ratio of the incident laser energy to the outgoing energy is a function of tube length, pollution density and pollution type. The longer the tube (path length), the more sensitive the instrument (Hodges *et al.*, 2004). Similar to coda wave interferometry, the path can be increased by multiple sampling of the same area. In optics this is called Cavity Ring-Down Spectroscopy (O'Keefe & Deacon, 1988).

3.4 Estimation of velocity change from coda waves

For a constant change δv in seismic velocity and fixed location of the scatterers and reflectors, we can write the propagation path $l = vt$, where v is the constant seismic velocity and t the propagation time. For a homogeneous velocity change δv in the medium and an unchanged path we get $l = vt = (v + \delta v)(t + \delta t)$, or to first order

$$\frac{\delta v}{v} = \frac{-\delta t}{t}, \tag{3.1}$$

where δt is the travel-time difference caused by the velocity change δv. A more rigorous derivation in given in the appendix. We extract δt from the data by means of the cross-correlation function, where δt is given by the position of the maximum of the cross-correlation function that is defined as

$$R^{(t,t_w)}(t_s) \equiv \frac{\int_{t-t_w}^{t+t_w} u_{\mathrm{unp}}(t')\, u_{\mathrm{per}}(t'+t_s)dt'}{\left(\int_{t-t_w}^{t+t_w} u_{\mathrm{unp}}^2(t')dt' \int_{t-t_w}^{t+t_w} u_{\mathrm{per}}^2(t')dt'\right)^{\frac{1}{2}}}, \tag{3.2}$$

where the time window is centered at time t with duration $2t_w$, t_s is the time shift used in the cross-correlation, u_{unp} is the unperturbed (before the velocity change) wave field and u_{per} the perturbed wave field.

In the following experiments where we monitor rock properties, the coda consists of waves that are repeatetly reflected from the free surface, and waves scattered from the crystals and grains in rocks (see previous paragraph). The above formulation (equation 4.1, using the path summation in the appendix), includes all the scenarios for multiple scattering

sketched in figure 3.1, and we can use the same theory for all our measurements.

It is important to note that up to this point we have not distinguished between P- or S-waves. An extension for elastic waves is given by Snieder (2002), who uses an analysis based on a simple P- and S-wave equilibration model. Snieder (2002) shows that coda wave interferometry is much more sensitive to S-wave than P-wave velocity, in particular for a Poisson medium the velocity change measured with coda wave interferometry is given by

$$\frac{\delta v}{v} \approx 0.09\frac{\delta v_P}{v_P} + 0.91\frac{\delta v_S}{v_S}, \tag{3.3}$$

where v_S and v_P are S- and P-wave velocities, and δv_S and δv_P are the velocity changes for S and P-waves, respectively. In some situations, the coda can be dominated by a modal behavior as sketched in figure 3.1. In the case of a surface wave that repeatedly propagate around the circumference of a sample (figure 3.1b), we measure a change in surface wave velocity, which is approximately 0.9 times the S-wave velocity for typical Rocks (Carmichael, 1982).

In the following experiments we only consider the relative velocity change estimated from the coda of the ultrasonic measurements. Other types of perturbations such as the displacement of the source or receiver position and opening and closing of pores and fractures, leave a different signature on the time shifted correlation coefficient than a constant velocity change. Snieder (2004) gives a summary and a brief explanation for the different types of change that could potentially be monitored with coda wave interferometry.

All these laboratory experiments involve essentially the same measurement of ultrasonic waves, we measure the impulse response of a rock sample with compressional ultrasonic transducers. The difference between the experiments consists of the physics of the change introduced (stress, fluid saturation or temperature), the geometry, size and type (Berea sandstone, Elberton granite and aluminum) of the samples.

3.5 Monitoring uni-axial stress in Berea sandstone

Time-varying stress fields are important in a number of areas of geophysics. Changes near plate boundaries are important in order to understand plate tectonics (Bokelmann & Silver, 2002). In earthquake prediction, the stress field is important for understanding fault behavior and its relation to earthquake occurrence (Stein, 1999; Freed & Lin, 2001; Niu *et al.*, 2003). In hydrocarbon reservoirs, the stress field is changed by recovery operations. It is important to understand the associated temporal change for time-lapse reservoir monitoring (Teanby *et al.*, 2004). In underground coal mining, "Room and Pillar" is a method in which approximately half of the coal is left in place to support the roof of the active mining area. Monitoring the stress field in the pillars and roofs is crucial for safe mining operations (Nikitin, 2003).

Wyllie *et al.* (1958) measured ultrasonic P-wave velocity as a function of effective stress in water-saturated Berea sandstone. They showed that at a constant confining pressure, v_p increases with decreasing pore pressure, and for constant effective stress the velocity remains approximately constant. Similar relationships between effective stress and P-wave velocity

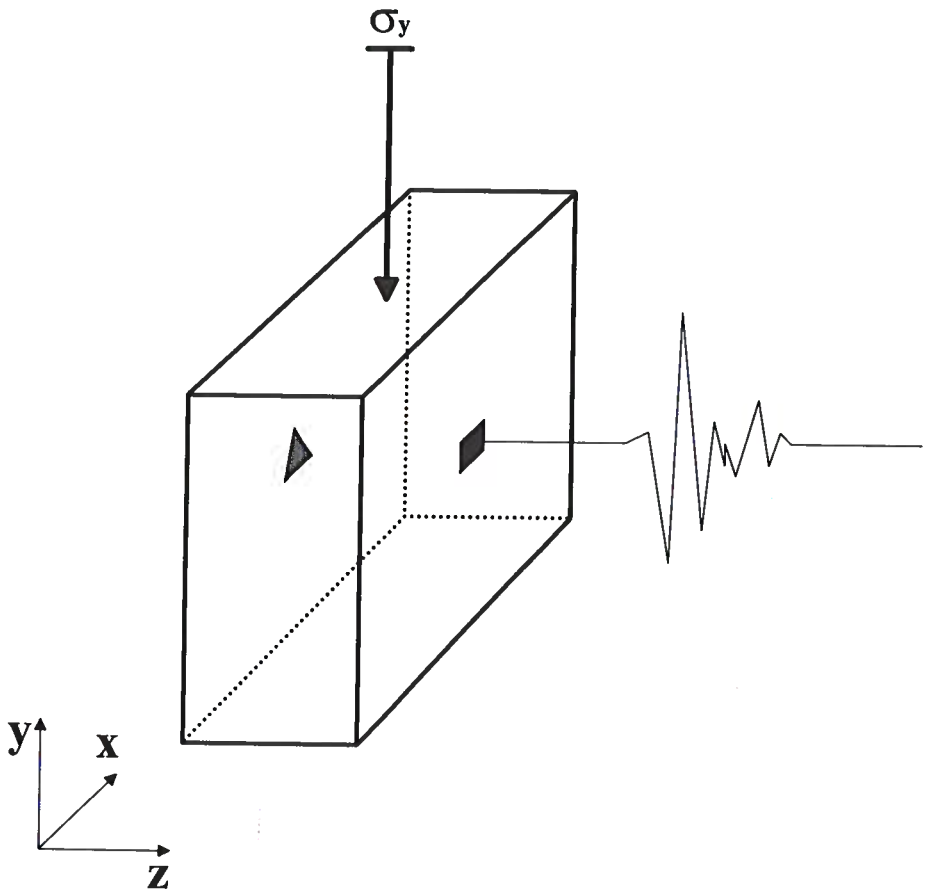

Figure 3.2. The first experiment a 12.5 x 40 x 40 cm^3 block of Berea sandstone is subjected to a uni-axial load in the y-direction. Ultrasonic waves propagate in the z-direction.

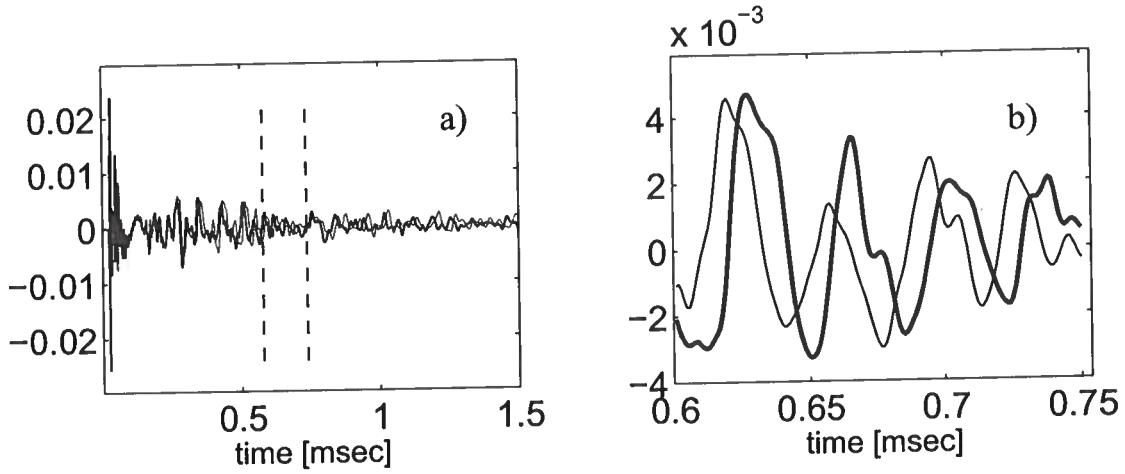

Figure 3.3. a) Two waveforms recorded at an applied uni-axial load level of 6 MPa (thick line) and 8 MPa (thin line). b) The same two waveforms as in figure 3.3a, but only a small time window of the signal is shown; the time interval is marked by the two dashed lines in 3.3a. The path length of the ultrasonic wave in this time interval is about 2.5 m and the wave has bounced back and forth about 20 times.

have also been reported by others (Nur & Simmons, 1969; Hicks & Berry, 1956; King, 1966; Christensen & Wang, 1985, e.g.,). Hence, a good knowledge of seismic velocity is important for pore pressure prediction. Experimental results indicate that confining and pore pressures have almost equal but opposite effects on v_p (Terzaghi's effective stress principle). Confining pressure influences the wave velocities because pressure deforms most of the compliant parts of the pore space, such as micro-cracks and loose grain contacts. Closure of micro-cracks increases the stiffness of the rock and increases bulk and shear moduli. An increase in pore pressure mechanically opposes the closing of cracks and grain contacts, which lowers the effective moduli and velocities. Hence, when both confining pressure and pore pressures vary, only the difference between the two pressures has a significant influence on velocity (Terzaghi, 1936; Hicks & Berry, 1956).

We show how coda wave interferometry can be used for stress-field monitoring in a laboratory environment. In this experiment we use a fine-grained Berea sandstone to investigate the dependence of elastic waves on uni-axial stress. The sandstone block is equipped with an ultrasonic source (transducer) on one side and a receiver on the other (Figure 3.2). The transducer excites the rock with a pulse with a dominant frequency of 0.2 MHz. A single receiver records the propagated waves, with a sampling interval of 1 μs. To reduce the noise level, 512 traces are stacked for each stress level. A typical record is shown in Figure 3.3a.

To introduce a controlled change in the medium over time, the sandstone block is placed in a hydraulic press and a uni-axial load is applied (see Figure 3.2). We monitor

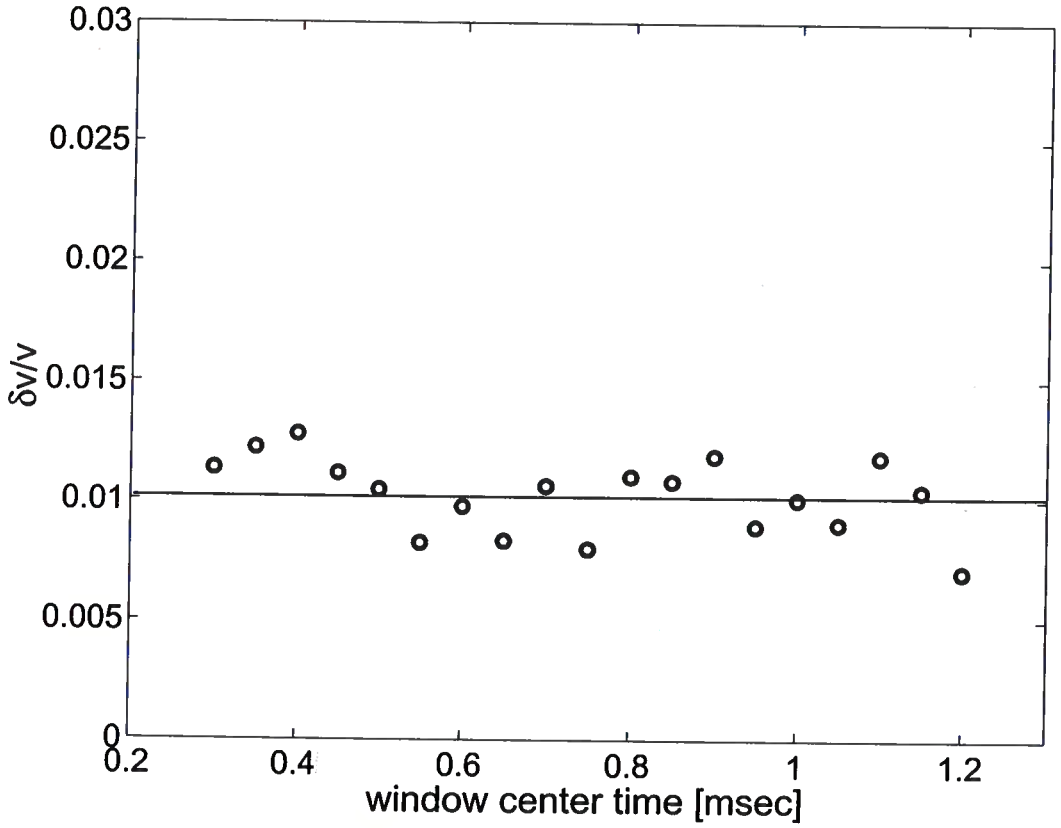

Figure 3.4. Velocity change estimates for 20 non-overlapping windows with different center times. The mean velocity change is 1.02 % and the standard deviation is 0.16 %.

uni-axial load by a pressure sensor between rock and press. For each stress state (4, 6 and 8 MPa) the ultra-sonic measurement is repeated.

Figure 3.3a shows two waveforms superimposed, one at a load of 6 MPa and the other at 8 MPa. After about 0.5 ms, the waves have a noisy appearance. If we look at a smaller time-window as shown in figure 3.3b, we see a strong correlation between the two waveforms, with one waveform time-shifted with respect to the other. Thus, despite the noisy appearance of the coda waves, these waves carry information about the structure of the medium, information that can be used to infer the change of sonic velocity with applied pressure.

We infer the velocity change caused by an increase in the load from 6 MPa to 8MPa, from the phase shift in the coda waves, using 20 non-overlapping time windows each with a duration of 0.05 ms each of the coda waves, as described in (Snieder *et al.*, 2002). The windows provide a independent estimates of the relative velocity change. This can be used for a consistency check of the method. Since we have multiple estimates of $\delta v/v$ we can calculate the mean and variance of the relative velocity change. The relative velocity change for these time windows is shown in Figure 3.4, this change is of the order of 1.02% for a increase in load of 2 MPa with an error of 0.16%.

Sarkar *et al.* (2003) shows comparable velocity changes in the same Berea sandstone block using one-way travel-times of the first arrivals (1 % for P-waves and 3 % for S-waves). They estimate the uncertainty, based on errors in travel-time picking to be approximately 1 %. Note that their measured velocity change is on the same order of magnitude than the estimated uncertainty. The accuracy and sensitivity of coda wave interferometry are an order of magnitude higher than methods based on one-way travel-time. In contrast to coda wave interferometry, Sarkar *et al.* (2003) are able to measure P- and S-wave velocity independently.

Monitoring stress changes is important, for example, in mining applications, radioactive waste disposal cites or fault zones. Using coda wave interferometry in these applications could lead to a highly sensitive stress-change monitoring technique with modest hardware requirements. Grêt *et al.* (2004b) apply coda wave interferometry to monitor stress changes in a gold and silver mine.

3.6 Monitoring water saturation in Berea sandstone

Seismic methods can monitor ground water (Bachrach & Nur, 1998), Dense Non-Aqueous Phase Liquid (DNAPL) contamination movement (Griffin & Watson, 2002), and hydrocarbon migration (Lumley, 1995; Mjaaland *et al.*, 2001) by detecting changes in seismic velocity. Compressional and shear wave velocities respond to changes in the bulk and shear modulus and density, caused by the presence of water. We demonstrate the application of coda wave interferometry for monitoring changes in water saturation in Berea sandstone.

We use an irregularly shaped piece of Berea sandstone with an approximate height of 20 cm and an approximate diameter of 5 cm. The sample is equipped with a compressional source on one side and a receiver on the other (Figure 3.5). The room-dry sample is placed

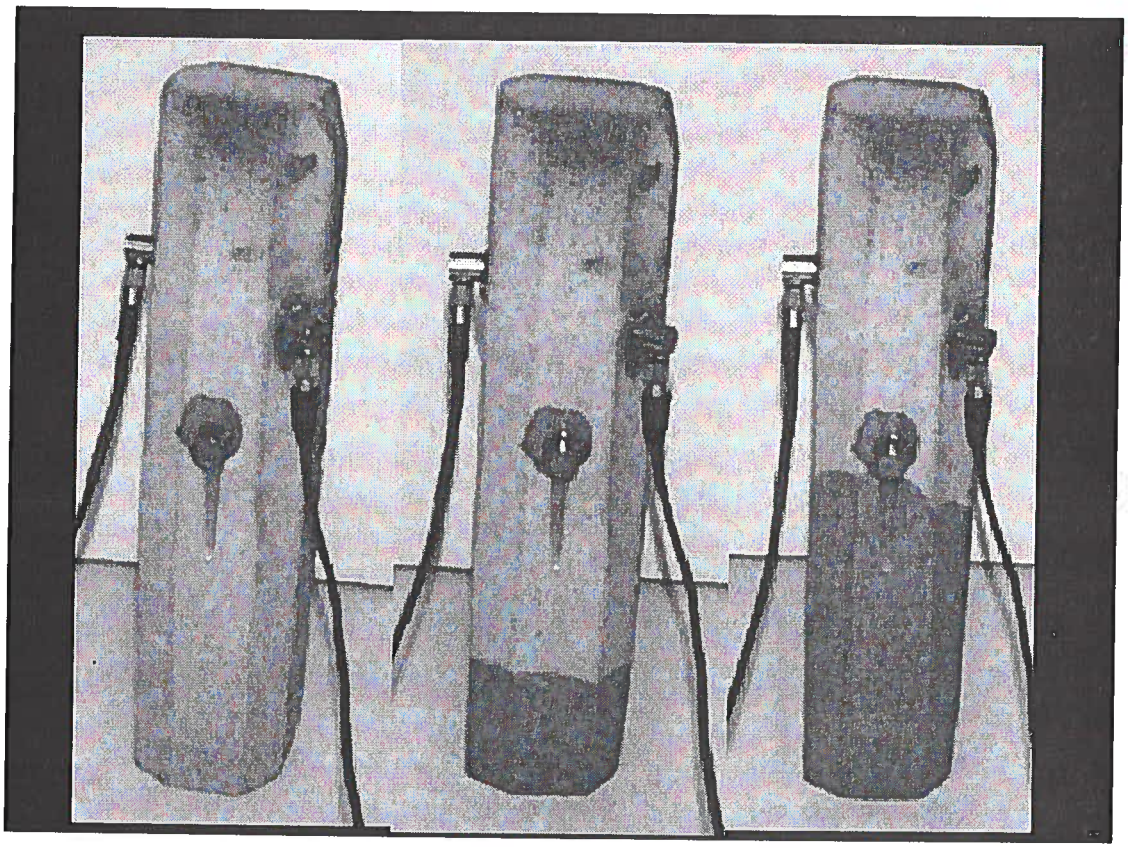

Figure 3.5. The Berea sandstone sample as the fluid is infiltrating. Ultrasonic source and receiver glued to the rock. The left picture shows the room-dry sample. The middle picture shows the water rising in the sandstone sample (dark line about a fourth up the sample) and the right picture shows the water almost half way up the rock. The third transducer glued to the rock is not used in this experiment.

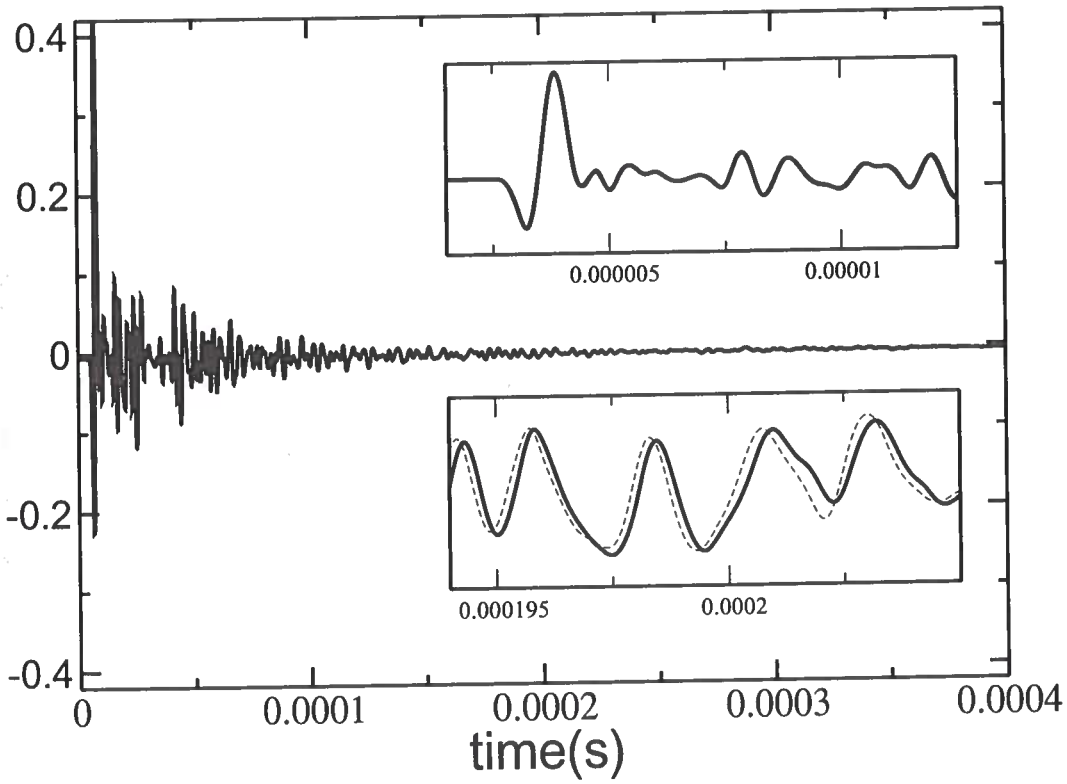

Figure 3.6. Wave-forms recorded in the Berea sandstone block for two different levels of water saturation (water infiltrated 2 cm of the rock (dashed line) and 3 cm (thin line)). The insets show details of the wave-forms around the first arrival (top) and in the late coda (bottom.). The dominant frequency is 0.33 MHz.

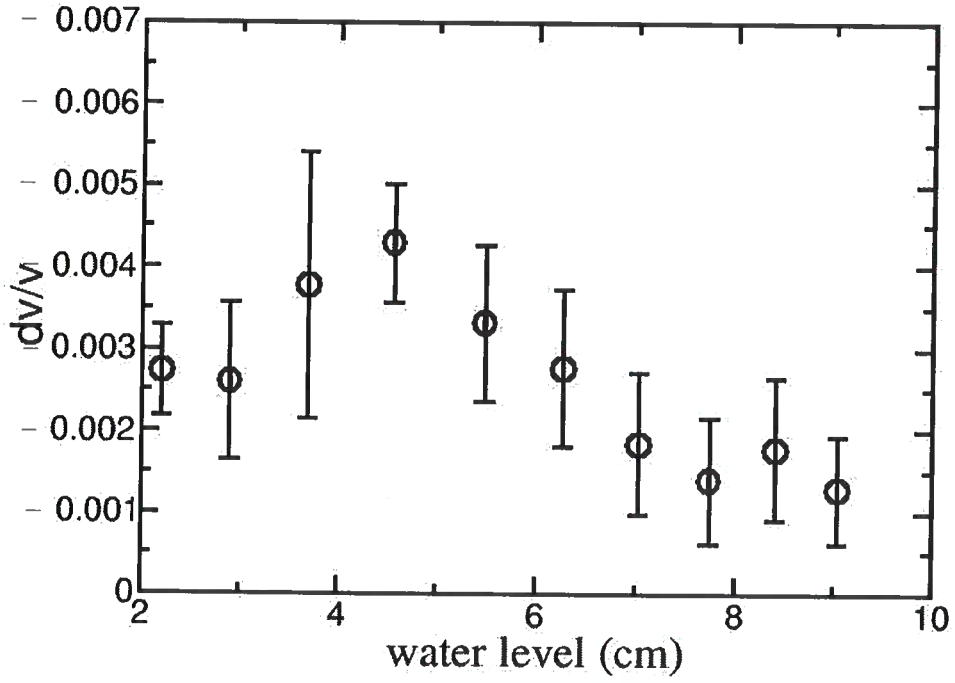

Figure 3.7. Relative velocity change $\delta v/v$ in Berea sandstone, for approximately 1 cm increment in water level from room-dry to 9 cm into the sample. Error bars are plus and minus one standard deviation.

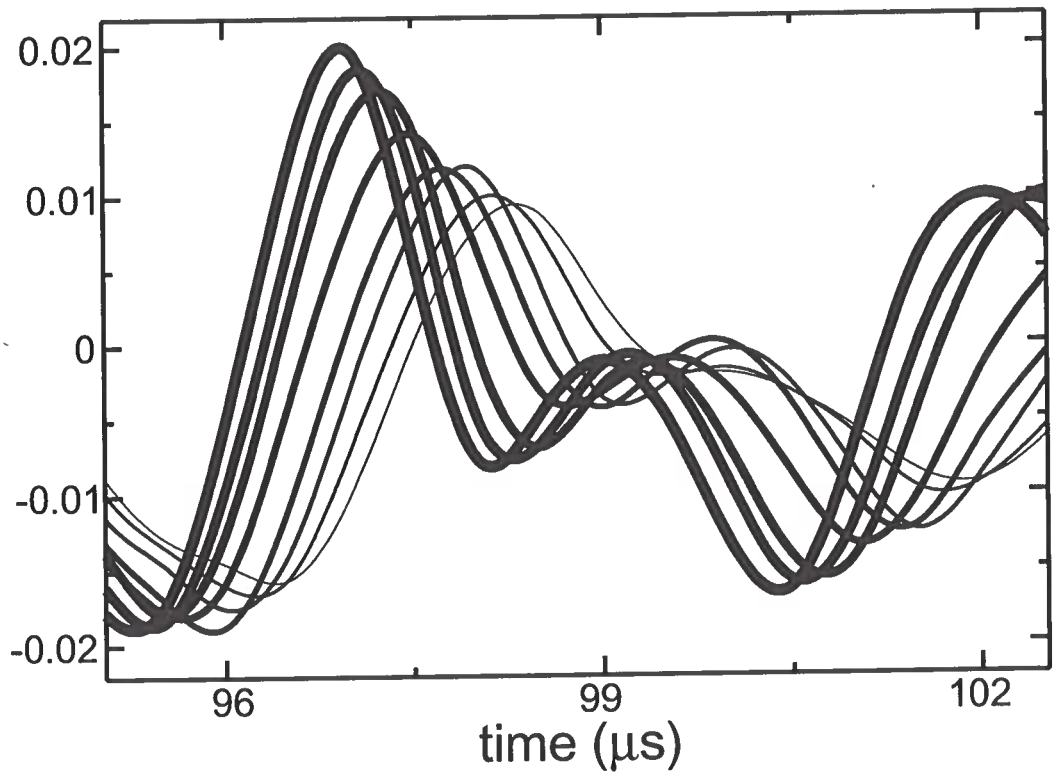

Figure 3.8. Eight waveforms, each measured at a different height of the water front. The fastest (thickest line) is measured on the dry sandstone and the slowest (thinnest line) is measured at a water front height of 7 cm. In addition to the velocity change, the amplitudes decrease with increased water content in the sample.

in a container that holds 5 mm of water. While the water is infiltrating into the pores of the sandstone by capillary pressure (Wulff & Mjaaland, 2002), the water-level in the container is kept constant at 5 mm. When the water-front is rising from 5 mm to 10 cm, we repeat the ultrasonic impulse-response measurement for every 1 cm increase in water-level in the sandstone. Again, for a 20 cm sample and a water-front rise of 1 cm there is no significant travel-time difference for the first arriving waves (see top inset of Figure 3.6). In a late time window (bottom inset of Figure 3.6), however, we see a distinct time shift of the wave-forms. Figure 3.8 shows the consistent slowing of the sonic waves with increasing water-level.

We infer the relative change in velocity for each change of 1cm in water-level using 12 different 0.1 ms time windows of the coda waves. The relative velocity change is of the order of -0.3% for a water-level rise of 1cm with an error of 0.05% (Figure 3.7). It is important to note that in many laboratory experiments, changes in rock properties are measured for saturation changes of about 5% on small samples (Spencer, 1981). With coda wave interferometry we can monitor fluid saturation about 10 times more precisely.

In addition to the effect on velocity, fluid saturation changes the attenuation of the rock (Mavko & Nur, 1979). In figure 3.8 one can clearly see the amplitude decrease with increased water-level. When monitoring velocity changes with coda wave interferometry, this attenuation change doesn't influence the estimates of the velocity change, because the normalization used in equation (3.2) renders the quantity independent of amplitude changes.

3.7 Monitoring thermally induced velocity changes in aluminum

The dependence of ultrasonic velocity on temperature in metals and alloys is an important characteristic in non-destructive testing (Kobori & Iwashimizu, 1990, e.g.,). Often, the effect of stress on this velocity/temperature relationship is studied (Salama & Ling, 1980; Chern & Heyman, 1981). Multiply scattered or reverberating waves are known to be sensitive to variations in temperature (Weaver & Lobkis, 2000). We use this sensitivity of coda waves to monitor temperature changes in aluminum.

In this ultrasonic experiment we use an aluminum cylinder with a height of 11 cm and a diameter of 5.5 cm. The sample is equipped with an ultrasonic source on one side and a receiver on the other (Figure 3.9). The transducer sends a pulse through the sample, and the single receiver records the impulse response of the sample, with a sampling interval of $1\mu s$ (the dominant frequency is 100 kHz.) We stack ten traces to reduce the noise level. Two typical records for a cylindrical sample are shown in Figure 3.10. To apply a controlled change in the medium, the aluminum sample is equipped with a heating element in a central borehole. We monitor the temperature with two thermocouples glued to the side of the sample and in the borehole (Figure 3.9).

While increasing the temperature from 25^oC to 90^oC, we repeat the ultrasonic measurement for every 5^oC increase in temperature. Then the aluminum sample is cooled to room-temperature and we repeat the ultrasound measurement again for every 5^oC in temperature decrease.

In some published laboratory experiments, the change in the seismic velocity is measured for a temperature change of about 100^oC (Timur, 1977; Peselnick & Stewart, 1975;

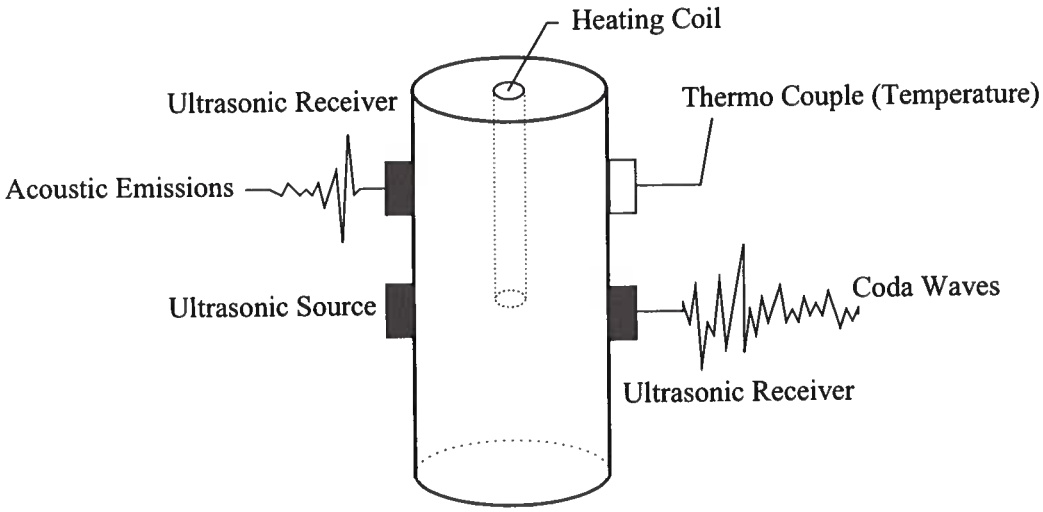

Figure 3.9. The cylinder represents the Elberton granite or the aluminum sample. Sonic waves are transmitted through the sample. A longitudinal transducer, which excites primarily P-waves, and an identical receiver (right rectangle) are used throughout the experiment. A third identical P-wave transducer (top left rectangle) detects acoustic emissions. The sample is heated with a heating coil placed in a centered borehole and the temperature is measured with a thermo-couple at the sample surface (white rectangle.)

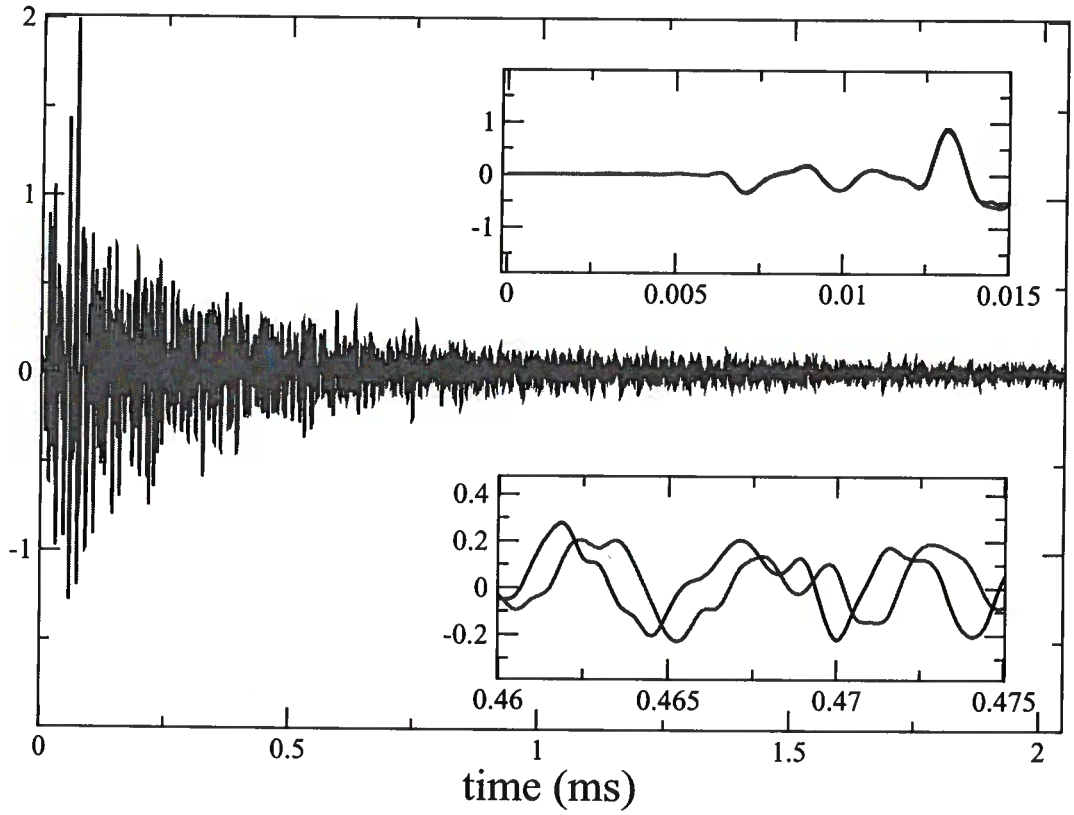

Figure 3.10. Wave-forms recorded in the granite sample for temperatures of 45^oC (thin line) and 50^oC (thick line), respectively. The insets show details of the wave-forms around the first arrival (top) and in the late coda (bottom.) The main frequency in the data is 0.13 MHz.

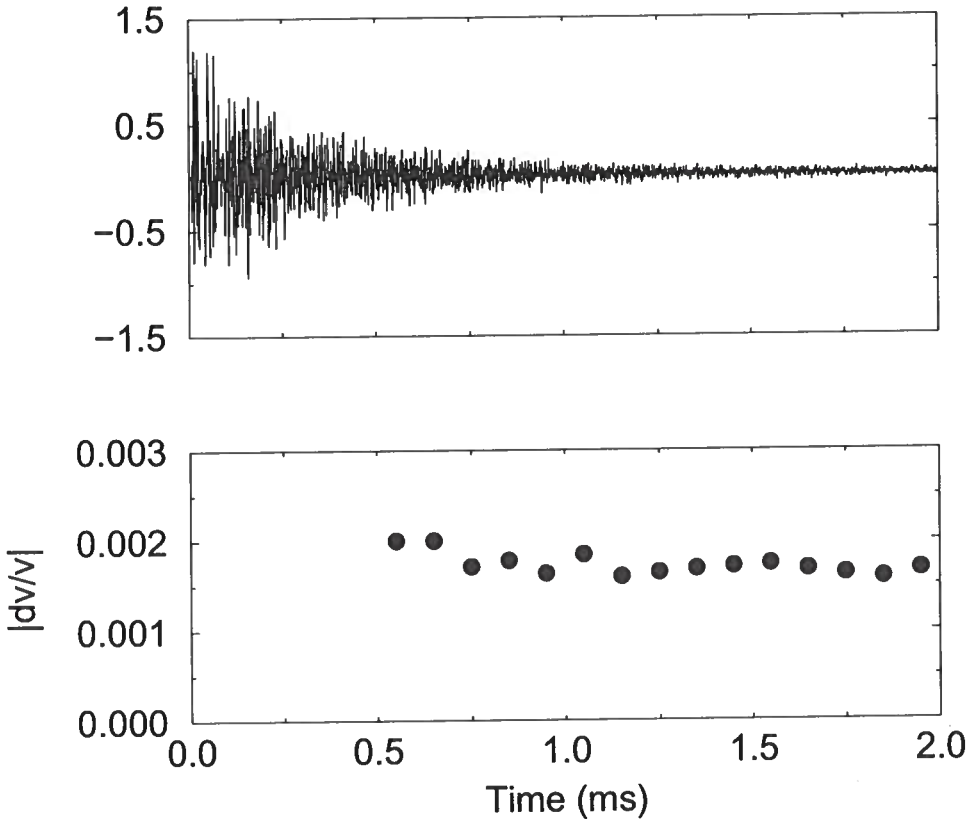

Figure 3.11. The top figure shows the ultra-sonic signal recorded on the aluminum sample. The bottom figure shows different estimates of $\delta v/v$ for multiple time-windows, therefore providing a consistency check.

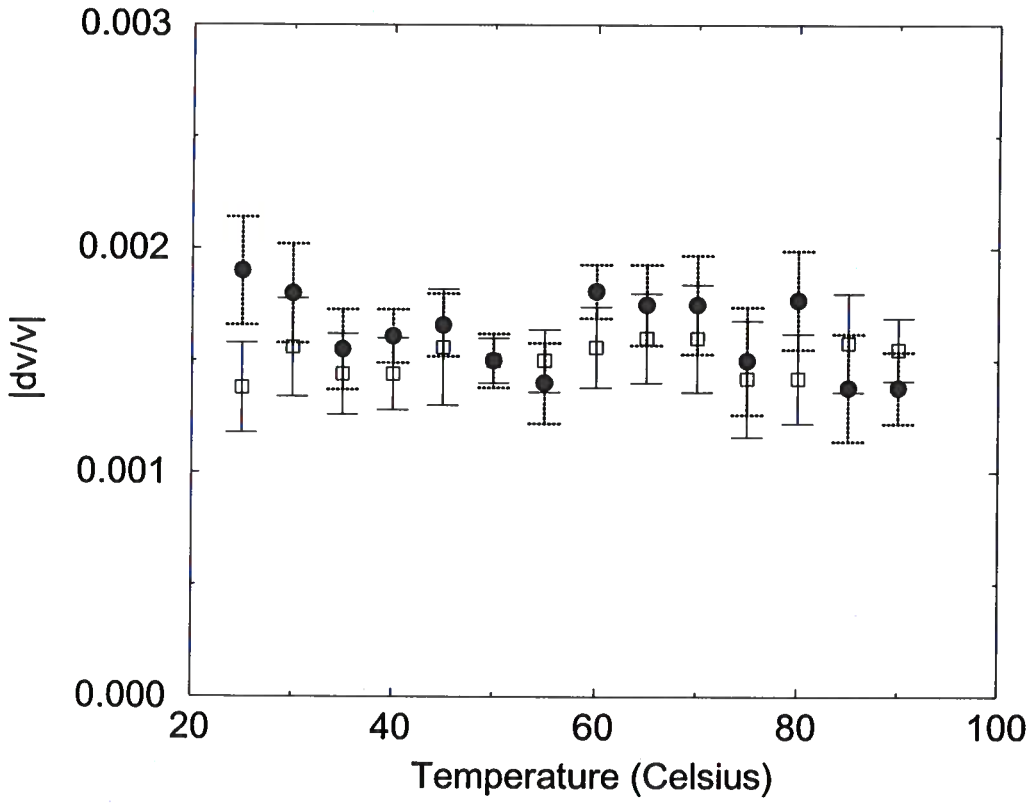

Figure 3.12. Absolute values of $\delta v/v$ in aluminum, for 5^oC temperature intervals from 25^oC to 90^oC. Circles correspond to the heating phase (velocity decrease) and rectangles (unfilled) to the cooling phase (velocity increase).

Hughes & Maurette, 1956). For a 11 cm small sample and a temperature difference of only 5^oC, there is no significant travel-time difference for the first arriving waves (see top inset of Figure 3.10). Therefore, first arriving waves do not provide any information about velocity changes for such a small temperature difference. In a late time window (bottom inset of Figure 3.10), we see a distinct time shift of the wave-forms. This information can be used to infer the change of ultrasonic velocity with temperature.

We estimate the relative change in velocity for each change of 5^oC in temperature with 20 different 0.1 ms time windows of the coda waves (figure 3.11). The relative velocity change is of the order of 0.15% for a temperature change of 5^oC with an error of 0.025% (Figure 3.12). It is important to note that with the exception of a sign change, the relative velocity change with temperature does not depend on whether the sample is in the heating or the cooling phase. In other words, if we sum all the relative velocity changes for the heating phase (negative velocity change) and the cooling phase (positive velocity change) we obtain a relative velocity change after the heating cycle that is approximately zero.

We use this laboratory experiment to test the presence of non-linear temperature effects on the measurement equipment, such as the piezoelectric transducers, the cables, the transducer couplant, and mounting devices. We measure a linear dependence of velocity on temperature in aluminum as in the experiment of Weaver & Lobkis (2000). We therefore conclude that non-linear instrument effects can be neglected. The change in path length due to thermal expansion of aluminum ($10^{-5}C^{-1}$ (Carmichael, 1982)) causes an apparent velocity change. This effect is two orders of magnitude smaller than the obtained velocity change from the coda waves and can be neglected.

3.8 Monitoring thermally induced velocity change and acoustic emissions in granite

With the same technique and same experimental setup as described in the previous section, we measured the thermally induced velocity change in a granite sample. In addition, we count acoustic emissions for every temperature interval. Since the coefficient of thermal expansion for quartz is $10^{-6}C^{-1}$ (Carmichael, 1982), the associated apparent velocity change is three orders of magnitude smaller than the velocity change obtained from the coda waves and can be neglected.

During the heating phase the velocity decrease (negative relative velocity change) is constant for each 5^oC increase in temperatures, for temperatures below 70^oC. At that temperature, however, the velocity change is non-linear (Figure 3.13). Since we tested for non-linear temperatrure effects of the measurement equipment on the aluminum sample, the non-linear velocity decrease in granite must be attributed to a change in the rock sample. The temperature of 70^oC corresponds to the critical fracture temperature for granite (Johnson *et al.*, 1978; Fredrich & Wong, 1986). Thermal cracking results from the internal stress concentration induced by thermal expansion anisotropy or thermal expansion mismatch between minerals or grains. Such micro-cracking is a similar effect as the thermal stresses induced by thermal gradients in homogeneous solids; for a high temperature gradient, cracking may occur even in a perfectly homogeneous solid (Boley & Weiner, 1960).

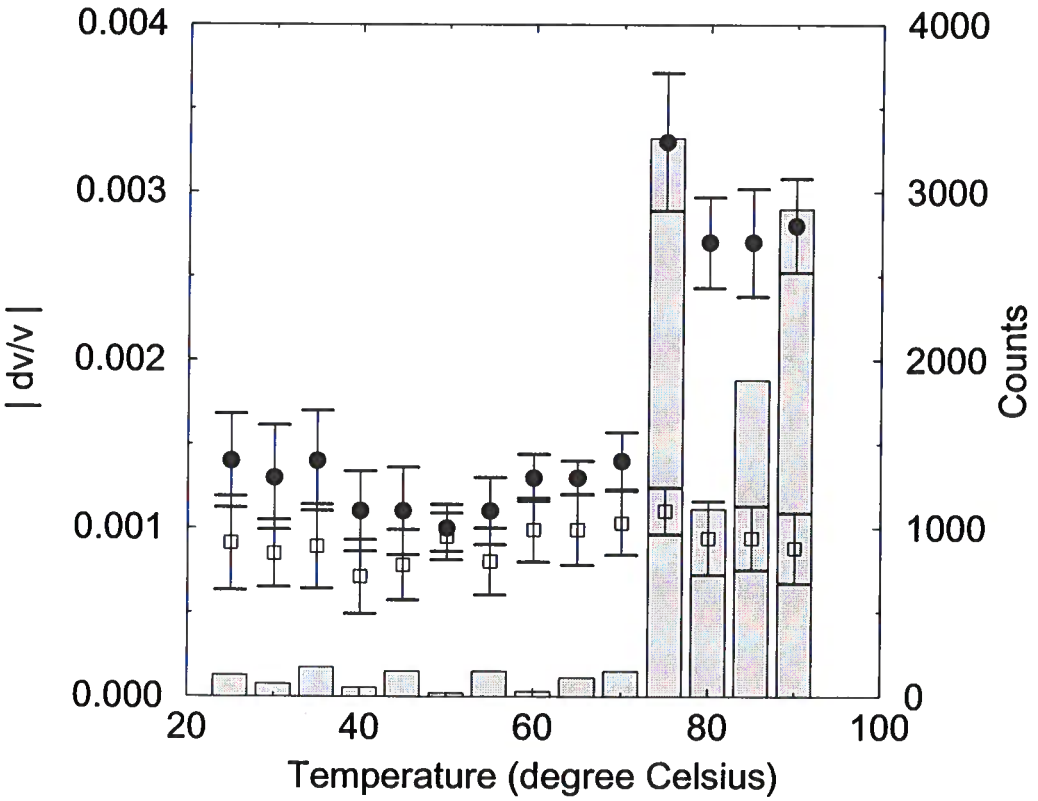

Figure 3.13. Absolute values of $\delta v/v$ in Elberton granite, for 5^oC temperature intervals from 25^oC to 90^oC. Circles correspond to the heating phase and rectangles to the cooling phase. The histograms show the count of acoustic emissions for a given temperature interval during the heating phase.

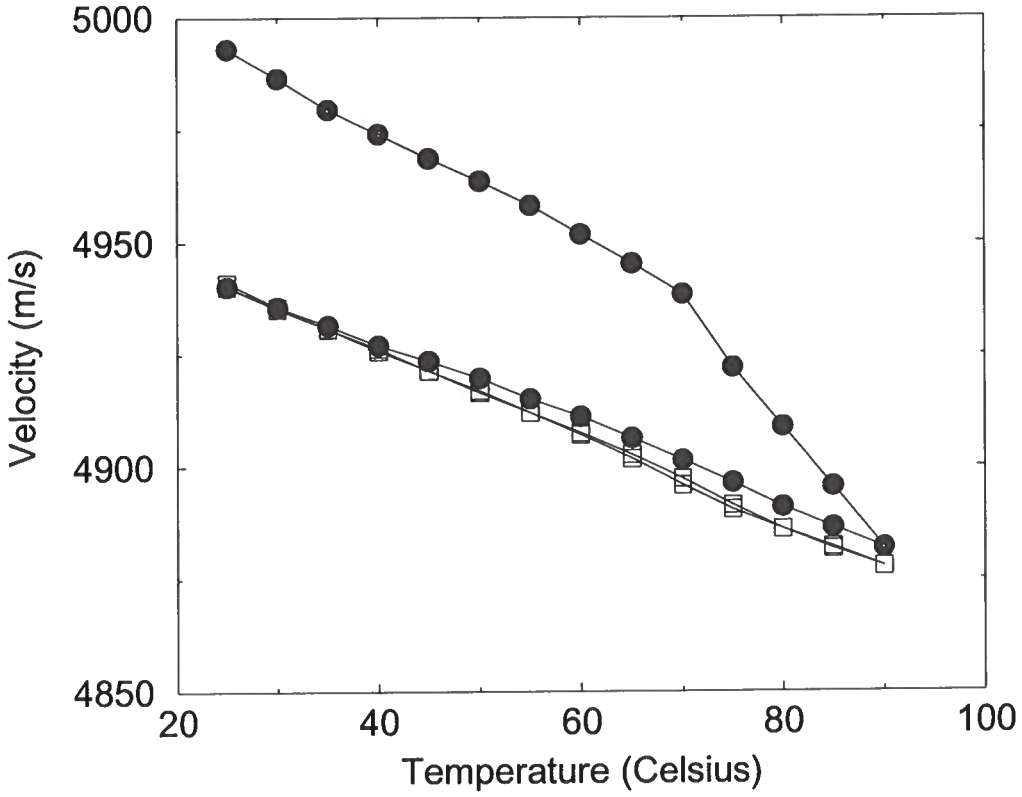

Figure 3.14. Velocity versus temperature in Elberton granite, for two heating cycles. Filled circles represent the first heating cycle and open rectangles the second. Note that during the second heating cycle the temperature dependent velocities during the heating and cooling phase are indistinguishable.

Fredrich & Wong (1986) show that thermal cracking in rocks occurs principally along mineral or grain boundaries. The thermally induced cracks can significantly influence both the mechanical and transport properties, as well as thermoelastic moduli (Simmons & Cooper, 1978).

In this experiment we use a third ultrasonic transducer to detect acoustic emissions in the granite due to thermal cracking. The histogram in Figure 3.13 shows the count of acoustic emissions versus temperature. There is a small number of acoustic emissions at low temperatures. There is, however, a significant increase in acoustic emissions between 70^oC and 75^oC. The increase in velocity change and the jump in the number of acoustic emissions correlate well.

Kaiser (1953) found that during repeated loading of metals, little or no acoustic emissions occurred until previously applied stress levels where exceeded. Since then, this effect has been known as the "Kaiser effect." Later, it was found that the Kaiser effect is a common phenomenon for various materials including rocks (Kurita & Fujii, 1979; Lavrov, 2002). Thus, the maximum stress applied in the previous cycles is 'memorized' in rocks.

During the cooling phase of the granite, the velocity depends linearly on temperature over the whole temperature change and there are few acoustic emissions. The seismic velocity does not return to its initial value at the end of the cycle. This difference in velocity is due to irreversible damage done to the rock by thermal cracking (Figure 3.14).

Todd (1973) studied the acoustic emissions of Westerly granite during cyclic heating. He noted that if a sample was re-heated to the same maximum temperature, few acoustic emissions occurred. Similarly we find in a second heating cycle up to the same maximum temperature (90^oC) for the same granite sample, only few acoustic emissions occur and there is no non-linear velocity decrease around 70^oC. Furthermore, the velocity increases back to the value before the second heating cycle when cooled down (Figure 3.14). Note that there is a small difference in relative velocity change between the cooling phase of the first heating cycle and the second cycle. Thirumalai & Demou (1973) studied the residual strain in a granitic rock produced by cyclic heating, and showed that predominant damage took place during the initial exposure to heating and the damage reached a steady state after three successive heating cycles. If we increase the temperature above the previous maximum temperature (90^oC), the same non-linear effect occurs; the granite "remembers" the maximum temperature.

This indicates that two different mechanisms drive the temperature induced velocity change. The first mechanism is the change in bulk elastic constants with temperature, which is linear and reversible. This explains the constant velocity change with temperature during the second heating cycle during heating and cooling. The second mechanism is the irreversible damage done to the granite due to thermal cracking, which explains the non-linear velocity change at the critical fracture temperature during the first heating cycle.

Ide (1937), found the same temperature dependence of velocity on temperature in Quincy granite. Using the travel time of first arrivals, he obtained 7 measurements over one heating cycle, with a peak temperature of 300^oC. With coda wave interferometry we are able to measure twenty times more points over the same temperature interval. In other words, coda wave interferometry is orders of magnitude more sensitive to a temperature

change.

3.9 Conclusions

Due to the sensitivity of coda waves, we are able to study the influence of changes in stress, temperature and fluid on small samples to a high level of precision. The key idea is that multiple sampling of the same area increases the sensitivity of coda waves. This new level of sensitivity may lead to a better understanding of rock properties and material properties in general.

The velocity estimation based on the coda waves requires only a single repeatable source and a single receiver, which makes it a potential method for inexpensive, real-time monitoring of land slides, hydrocarbon reservoirs, volcanoes, nuclear waste disposal sites and as a diagnostic tool in non-destructive testing. Snieder & Vrijlandt (2004) apply coda wave interferometry to obtain the relative location of earthquakes from the seismic coda.

Coda wave interferometry has similarities with Cavity Ring-Down spectroscopy (O'Keefe & Deacon, 1988) and resonance spectroscopy (McSkimmin, 1964). In those methods modes are excited and analyzed in time or frequency. In contrast, we can use coda wave interferometry in field experiments, when it is not possible to excite modes because the system is open. For example, we use multiply scattered seismic waves to monitor a rapid temporal change in a volcano (Grêt *et al.*, 2004a). We could use coda wave interferometry to monitor minute changes in-situ, for example in groundwater monitoring or DNAPL contamination. On a global seismology scale, coda wave interferometry could play an important part in monitoring large scale changes using surface energy from earthquakes that circle the earth many times (Earth HUM). In addition there are countless industrial applications, where monitoring of stress, cracks, temperature and fluids is important, including aircraft engine monitoring, monitoring of punch press heads or applications in medical imaging like monitoring osteoporosis.

3.10 Acknowledgments

We thank Bob Kranz, Debashish Sarkar and Mike Batzle for their help with the experiments. We also thank the members of the Center for Wave Phenomena and the Physical Acoustics Laboratory for stimulating discussions. This work was partially supported by the NSF(EAR-0106668 and EAR-0337379).

3.11 Appendix

This appendix follows Snieder (2002). For a change in the wave velocity, for quasi-random perturbations of the point scatterer location, or for a change in the source location, we can estimate this perturbation from multiply scattered waves by a cross-correlation in the time domain (Snieder *et al.*, 2002). We refer to the waveform before the perturbation as the unperturbed signal, and to the waveform after the perturbation as the perturbed

signal. The unperturbed wave-field can be written as a Feynman path summation over all possible trajectories T (Snieder, 1999):

$$u_{\rm unp}(t) = \sum_T A_T(t), \tag{3.4}$$

where a trajectory is defined as a sequence of scatterers encountered by the wave. The sum over trajectories contains a sum over all possible mode conversions (P-waves, S-waves and surface waves), and it describes both trajectories that bounce off the free surface and/or trajectories that connect scatterers.

When the background velocity is perturbed, the dominant effect on the waveform arises from the change in the travel time τ_T of the wave that travels along each trajectory:

$$u_{\rm per}(t) = \sum_T A_T(t - \tau_T). \tag{3.5}$$

We can compute the time-windowed correlation coefficient between the unperturbed and the perturbed signal from equation (3.2). When the perturbed and unperturbed wave fields defined by equations (3.4) and (3.5) are inserted into (3.2), double sums over all trajectories appear. The cross-terms with different trajectories ($T \neq T'$) are incoherent and average out to zero when the mean of the source signal vanishes. We therefore approximate the time-windowed correlation coefficient by:

$$R^{(t,t_w)}(t_s) \approx \frac{\sum_{T(t,t_w)} C_T(\tau_T - t_s)}{\sum_{T(t,t_w)} C_T(0)}, \tag{3.6}$$

where the sum is taken over the trajectories with arrival times within the time window of the cross-correlation, and the auto-correlation of the source signal is defined as

$$C_T(t) \equiv \int_{-\infty}^{\infty} A_T(t'+t) A_T(t') dt'. \tag{3.7}$$

For time shifts τ much smaller than the dominant period, a second-order Taylor expansion gives $C(\tau) = C(0)(1 - \frac{1}{2}\overline{\omega}^2\tau^2)$, where $\overline{\omega}^2$ is the mean-squared frequency of the waves that arrive in the time window defined as:

$$\overline{\omega}^2 \equiv - \frac{\sum_T \int_{t-t_w}^{t+t_w} A_T(t') \ddot{A}_T(t') dt'}{\sum_T \int_{t-t_w}^{t+t_w} A_T(t')^2 dt'}. \tag{3.8}$$

Using this in equation (3.6) we can write

$$R^{(t,t_w)}(t_s) = 1 - \frac{1}{2}\overline{\omega}^2 \left\langle (\tau - t_s)^2 \right\rangle_{(t,t_w)}, \tag{3.9}$$

where $\langle \cdots \rangle_{(t,t_w)}$ stands for the average over the wave paths with arrivals in the time interval $(t - t_w, t + t_w)$.

The time shifted cross-correlation $R^{(t,t_w)}(t_s)$ has a maximum when

$$t_s = t_{\max} \equiv \langle \tau \rangle_{(t,t_w)}\,, \tag{3.10}$$

where $\langle \tau \rangle_{(t,t_w)}$ is the mean travel time perturbation of the arrivals in the time window. Using expressions (3.9) and (3.10) gives the maximum value of the cross-correlation

$$R_{\max}^{(t,t_w)} = 1 - \frac{1}{2}\bar{\omega}^2\sigma_\tau^2, \tag{3.11}$$

where σ_τ^2 is the variance of the travel time perturbation for waves arriving within the time window. This means that we can extract the mean and the variance of the travel time perturbations of the waves arriving in a time window.

For a constant change δv in seismic velocity and fixed locations of the scatterers, the mean travel time perturbation is given by $\langle \tau \rangle_{(t,t_w)} = -(\delta v/v)t$. When the time window is small ($t_w \ll t$), $\sigma_\tau \approx 0$. The velocity change follows from the time of the maximum of the time-shifted cross-correlation function:

$$\frac{\delta v}{v} = \frac{-t_{max}}{t}. \tag{3.12}$$

Chapter 4

Monitoring stress change in an underground mining environment with coda wave interferometry

4.1 Abstract

We developed a new technique (coda wave interferometry) that uses multiply scattered waves to monitor changes in a medium. Coda waves are highly sensitive to changes in stress, deformation, temperature, fluids and more. Because of this sensitivity we can monitor small stress changes in an underground mine. We applied coda wave interferometry to seismic data excited by a hammer source, collected at an experimental hard rock mine, Idaho Springs, CO. We carried out a controlled stress-change experiment in a pillar and we were able to monitor the internal stress change with coda wave interferometry.

4.2 Introduction

The coda is the tail (Latin *cauda*) of a waveform, it consists of that part of the signal after the directly arriving phases (Aki, 1969). Its late part is dominated by multiply scattered and/or multiply reflected waves (Aki & Chouet, 1975). Coda waves are used in a multitude of geophysical applications, such as earthquake-magnitude estimation (Lee *et al.*, 1972), earthquake prediction (Aki, 1985; Sato, 1986), volcano monitoring (Aki & Ferrazzini, 2000; Fehler *et al.*, 1998), monitoring of temporal changes in the subsurface (Chouet, 1979; Poupinet *et al.*, 1984; Robinson, 1987), and relocation of earthquake clusters (Snieder & Vrijlandt, 2004). Laboratory applications include diffusive wave spectroscopy (Cowan *et al.*, 2002), reversed time imaging (Fink, 1997), medical imaging (Li *et al.*, 1997) and cavity ring-down spectroscopy (O'Keefe & Deacon, 1988).

Changes in a medium can be so small that they have no detectable influence on seismic waves that sample the area only once. These changes are, however, amplified by multiple scattering and may be readily seen in the coda. We have developed a new method called *coda wave interferometry* (Snieder *et al.*, 2002) to extract information about the change in the medium from the coda. We have previously used coda wave interferometry to study the non-linear temperature dependence of ultrasonic velocity in granite (Snieder *et al.*, 2002), the dependence of ultrasonic velocity on stress change and water saturation in Berea sandstone (Grêt *et al.*, 2004c), and monitoring of a rapid temporal change in a volcano (Grêt *et al.*, 2004a). Of particular interest for the mining community is our experiment where

we monitor acoustic emissions (due to cracking) in granite with coda wave interferometry (Grêt *et al.*, 2004c).

In this work we demonstrate the usefulness of coda wave interferometry for monitoring stress changes in an underground mining environment. It is known that the sensitivity of seismic wave velocity to stress changes in rocks is low (Nur, 1971) and detection of temporal variations has been extremely difficult (Niu *et al.*, 2003). Attempts have been made to monitor stress changes in underground mines with travel-time tomography, where tomographic images based on one-way travel-times of seismic waves for different stress states are compared (Friedel *et al.*, 1995, 1996). Since a major stress change in rocks only leads to a small change in velocity, those methods are inherently prone to large uncertainties. Hence, tomography studies to monitor stress changes in rocks have to be viewed with caution. Instead of sampling the regional stress once as in the tomography approach, we make use of the fact that repetitive sampling of the same area by coda waves makes these waves increasingly sensitive to stress changes. Since coda waves are so sensitive to small changes in the medium, they are a suitable tool to monitor stress changes in rocks (Grêt *et al.*, 2004c).

4.3 Short introduction to coda wave interferometry

A detailed description of coda wave interferometry is given by Snieder (2002), and by Grêt *et al.* (2004c). Here we give the main results that are needed to understand the technique. For a change in the medium that consists of a constant change δv in seismic velocity and unchanged locations of the scatterers and reflectors, we can write the path length l that the seismic waves cover as $l = vt$, where v is the seismic velocity and t the propagation time. For a constant velocity change δv and an unchanged path length l we get $l = vt = (v + \delta v)(t + \delta t)$, hence to first order

$$\frac{\delta v}{v} = \frac{-\delta t}{t}, \tag{4.1}$$

where δt is the travel-time difference (in a given time window) caused by the velocity change δv. We extract δt from the data by means of the cross-correlation function, that is defined as

$$R^{(t,t_w)}(t_s) \equiv \frac{\int_{t-t_w}^{t+t_w} u_{\rm unp}(t')\, u_{\rm per}(t'+t_s)dt'}{\left(\int_{t-t_w}^{t+t_w} u_{\rm unp}^2(t')dt' \int_{t-t_w}^{t+t_w} u_{\rm per}^2(t')dt'\right)^{\frac{1}{2}}}, \tag{4.2}$$

where the time window is centered at time t with duration $2t_w$, t_s is the time shift used in the cross-correlation, $u_{\rm unp}$ is the unperturbed (before the velocity change) wave field and $u_{\rm per}$ the perturbed wave field (after the velocity change), δt is the arrival time difference between the waves recorded before the velocity change and the waves recorded after the velocity change, for all the waves that arrive in the same time window. Hence, we can estimate δt for multiple non-overlapping time-windows independently and from equation (4.1) we calculate the relative velocity change for each time window. Thus, coda wave

interferometry features its own consistency check.

4.4 Experimental setup and local geology

The Edgar Mine, Idaho Springs, CO, is located about 55 km west of Denver, CO, and is owned and operated by the Colorado School of Mines (CSM), Golden, CO. The 305 m of crosscuts and drifts that access several silver-gold veins are located at en elevation of 2,405 m. Widths of the crosscuts and drifts average about 3 m, and the overburden above the mine is about 120 m. The experiment is performed on a 43 m long and 23 m wide pillar (figure 4.1). In order to introduce a controlled stress change in the pillar, a pressure cell was installed into the rock by Scott *et al.* (1999). The slot cut for the pressure cell is 1 m high and 0.76 m wide and is cut 3 m deep into the pillar. The slot was formed by drilling closely spaced holes into the pillar, and the pressure cell is installed to a depth of 2.1 m. Grout was pumped around the pressure cell to allow it to press against the walls of the slot without expanding excessively. The pressure cell that is used to induce pressure against the walls of the slot, measures 30 x 30 x 1 cm^3 (inset of Figure 4.1).

The mine is developed in Precambrian metamorphic and granitic rocks. Specifically, the rocks are assigned to the Idaho Springs Formation. Rocks in the pillar include biotite schist, biotite microcline pegmatite, biotite-hornblende schist, quartz-feldspar-biotite gneiss and migmatized gneiss. Ultrasonic core velocity measurements on rock samples from the Edgar mine were taken in the laboratory by Scott *et al.* (1999). Ultrasonic P-wave velocities for the biotite-hornblende-schist range between 5.00 km/s and 5.45 km/s, and for the pegmatite between 4.72 km/s and 4.75 km/s. Carmichael (1982) lists P-wave velocity changes for similar rocks (not from the Edgar Mine) for a pressure difference of 1000 psi in schist and pegmatite that range between 0.03% and 0.045%, depending on the specific kind and area of origin.

The seismic experiment consists of a repeated hammer source (5 kg sledge hammer) and two vertical component geophones bolted to the wall on the left and the right of the slot. One geophone is used as a trigger channel and the other for data acquisition with a Tektronix digital oscilloscope. The full seismic waveforms are recorded and saved to a computer.

The pressure in the cell is increased in steps of 220 psi, from 0 to 2200 psi. For every increase of pressure, we record three repeated seismic waveforms (three hits with the hammer). Those three seismic records are then stacked (averaged) in order to reduce random noise in the data. In addition, we apply a bandpass filter with corner frequencies of 20 Hz and 10 kHz to further reduce the electronic noise from the instruments. The stacked and filtered waveforms, recorded at different pressures in the cell are then compared to extract information about the stress change in the pillar.

4.5 Reproducible seismic waveforms

For late times, coda waves commonly have a noisy appearance (figure 4.2a). If we look closer, we find that not only are the first arriving wave modes reproducible (figure 4.2b) but

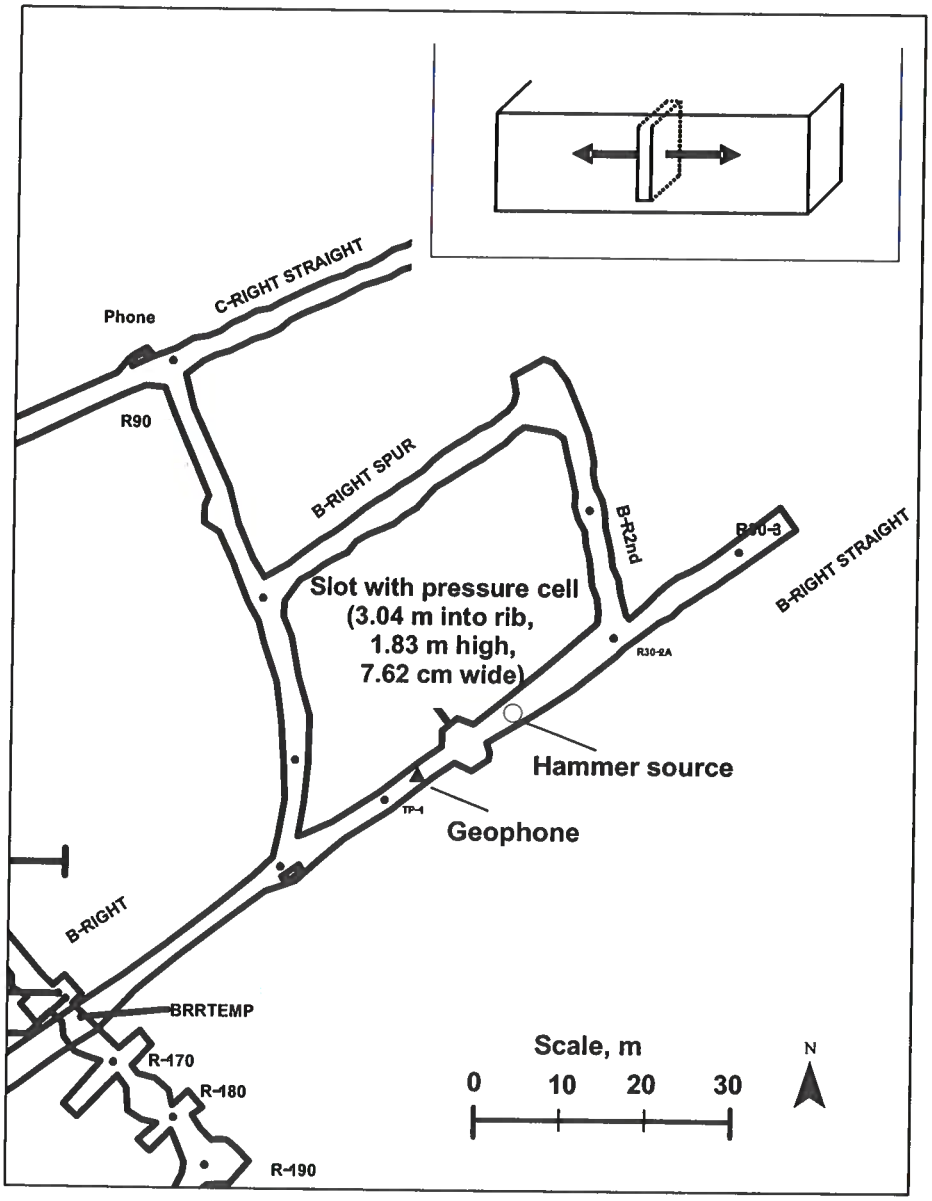

Figure 4.1. Plan view of the Edgar Mine pillar. Geophone and hammer source locations are labeled in the plan. The pressure cell in the slot is indicated by the small line between geophone and source location. The inset (top right) sketches the pressure cell installed in the pillar.

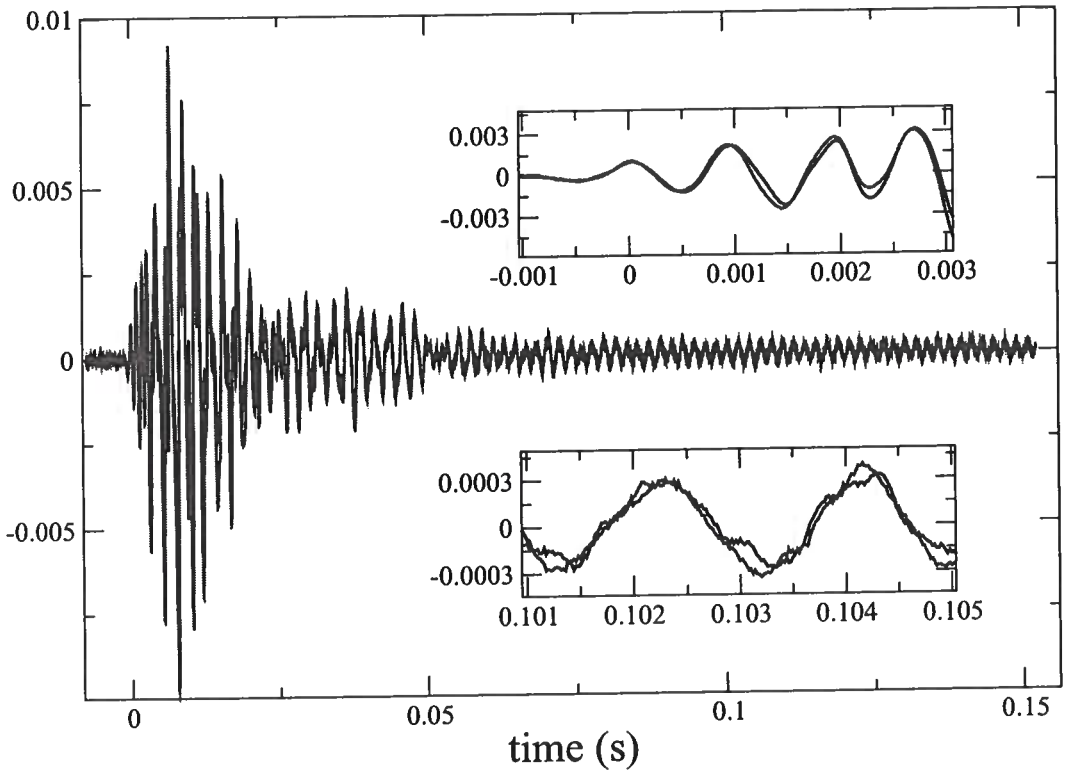

Figure 4.2. The blue line represents the first measurement and the red line the repeated measurement. The top inset (a) shows the early part of the seismic record and the bottom inset (c) shows a time window of the late part (coda). As described in the text, the whole waveform is highly reproducible.

the coda of two repeated measurements match wiggle by wiggle (figure 4.2c). Geophysicist often discard coda measurements because of their complexity. Their high repeatability shows that they are different from noise and carry information about the medium they propagated through. In the late coda, the noise level in the un-stacked data (vibration noise, instrument noise, air movement) is ten times smaller than the signal amplitude. We estimate the noise of the seismic records from that part of the measurement before the first arriving wave. Since in that section of the record no waves have yet reached the receiver, we only measure noise.

In order to quantify the reproducibility of the seismic waveforms we calculate a time-shifted correlation coefficient R_{max} (maximum of equation (4.2)) of 0.96 for two repeated measurements, which confirms the high repeatability of seismic coda measurements in the underground mining environment. In other words, if all the recording parameters (source, receiver, instrumentation) stay constant and nothing changes in the rock-mass, we can reproduce the same seismic measurement to a high degree of precision. If there is a change in the rock (e.g. stress, modulus of deformation) the seismic measurements will change too.

If we apply coda wave interferometry to our data, then the velocity perturbation that we infer is averaged over the entire pillar as well as over shear and compressional waves. However, even a cursory examination of the coda shows that after the transient has died out we have a nearly monochromatic (constant frequency) signal. The frequency measured is about 500 Hz. This frequency is consistent with the fundamental (lowest frequency) mode of a surface wave bouncing up and down between the base and roof of the pillar (about 3 m) along the surface near the source and receiver. It is also consistent with a higher overtone (or harmonic) of a body wave propagating back and forth within the pillar (25 m across). The measurements could be explained by several modes that match with the geometry of the pillar, velocity and frequency of the waves. We would need further information to conclusively determine what the type of wave mode is recorded. For example, we can use an array of receivers and compute the direction of wave propagation (Scales & Malcolm, 2003).

4.6 Decorrelation of coda waves with stress change

If we increase the pressure in the cell, we change the seismic velocity and thus the recorded waveforms are different. When the change in the medium is small, we only change the coda waves and the early arriving waves will remain unchanged. Figure 4.3a shows two waveforms, one recorded at 600 psi and one at 1800 psi. The early arriving waves (figure 4.3b) are invariant to the stress change and cannot be used to monitor a stress difference of 1200 psi in the slot. Consequently, tomographic images based on one-way travel-times, before and after the stress change, would be identical and cannot be used to monitor the stress difference. The coda waves, however, show a decorrelation of the waveforms (figure 4.3c). Hence, due to their increased sensitivity, coda waves can be used to monitor the velocity change that is induced by a stress difference of 1200 psi.

The velocity change in the medium does not lead to an erratic decorrelation of the coda but rather a coherent time lag or phase shift (figure 4.3c). We compute this time lag

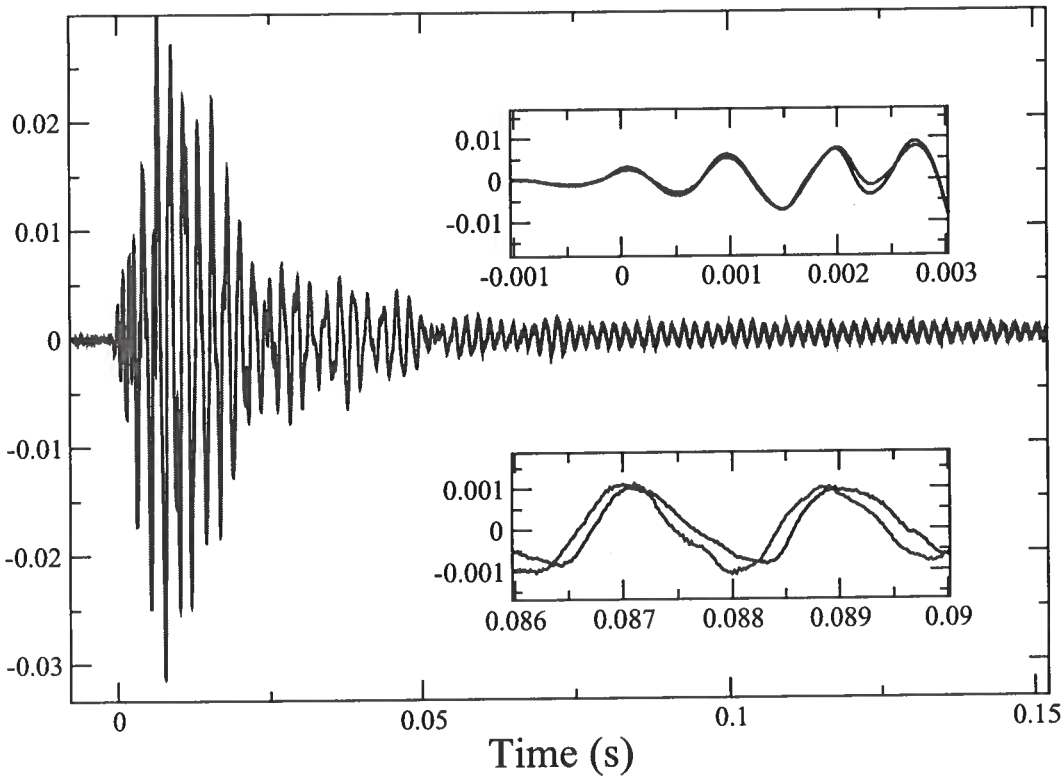

Figure 4.3. Two waveforms, one measured at 600 psi of pressure in the cell (blue) and one measured at 1800 psi (red). The top inset (a) shows the the early time window and the bottom inset (c) the coda.

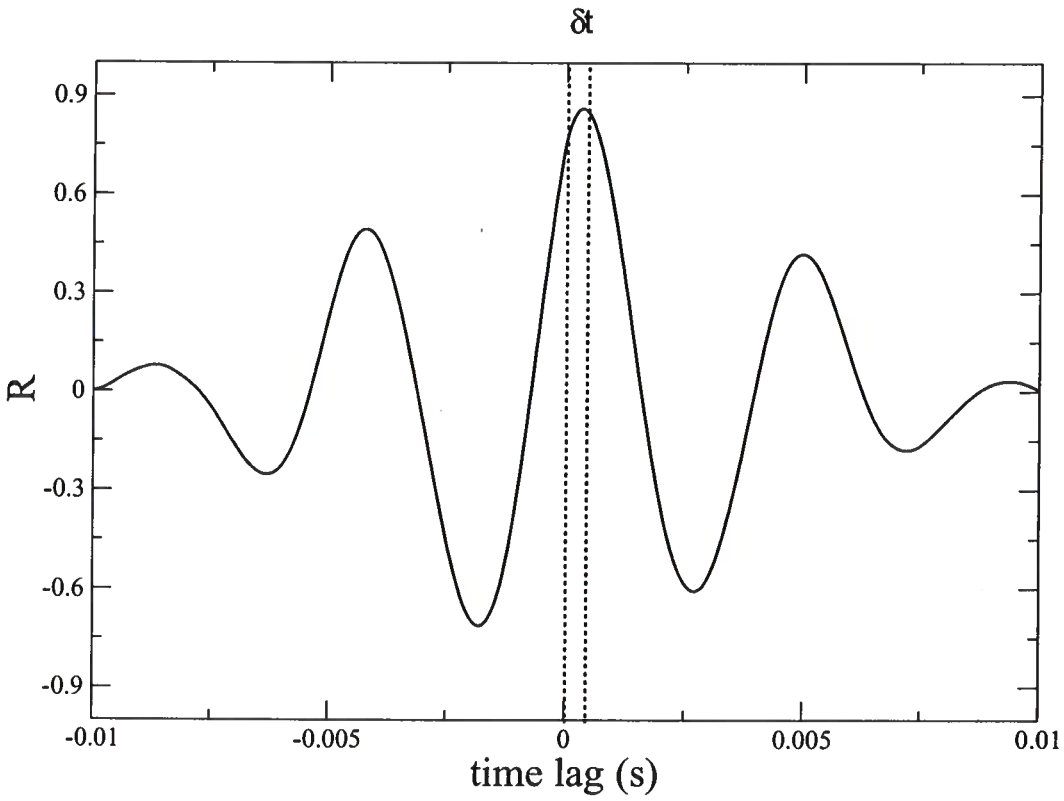

Figure 4.4. Cross correlation function of the data shown in figure 4.3c. Note that the maximum of the cross correlation function is centered at the time lag δt, which is the value we estimate from the coda.

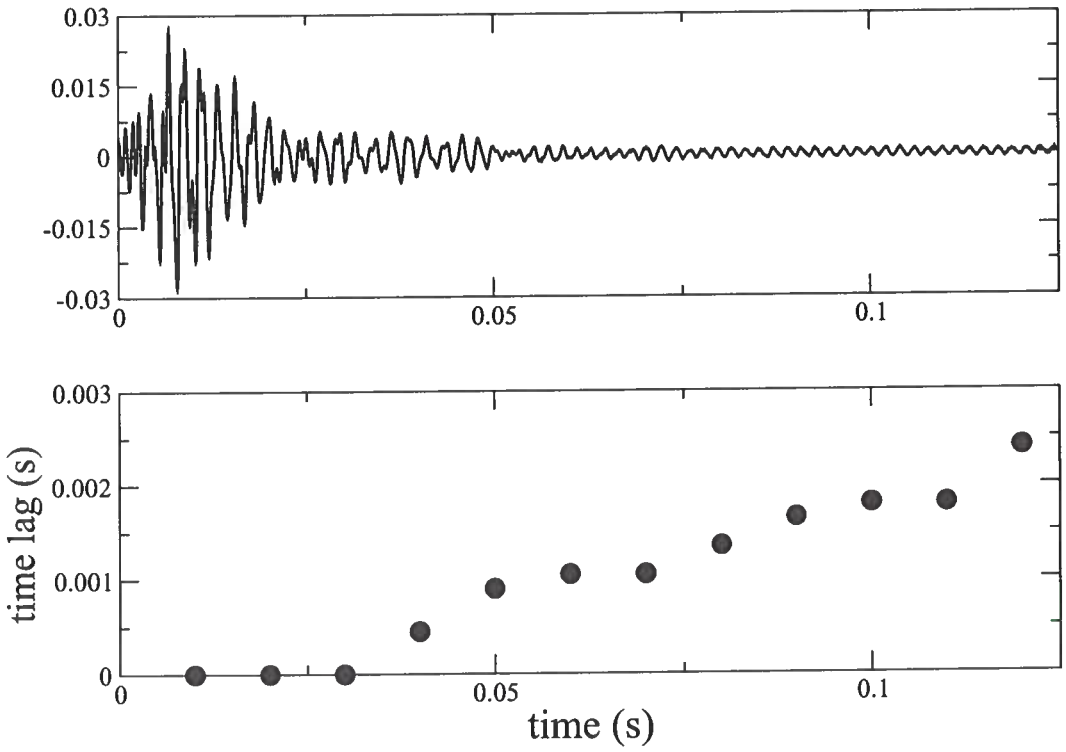

Figure 4.5. The top figure shows the seismic record. The bottom figure shows different estimates of δt for multiple time-windows, therefore providing a consistency check. The first three points are computed from the early part of the waveform and are not sensitive enough to detect the introduced velocity change.

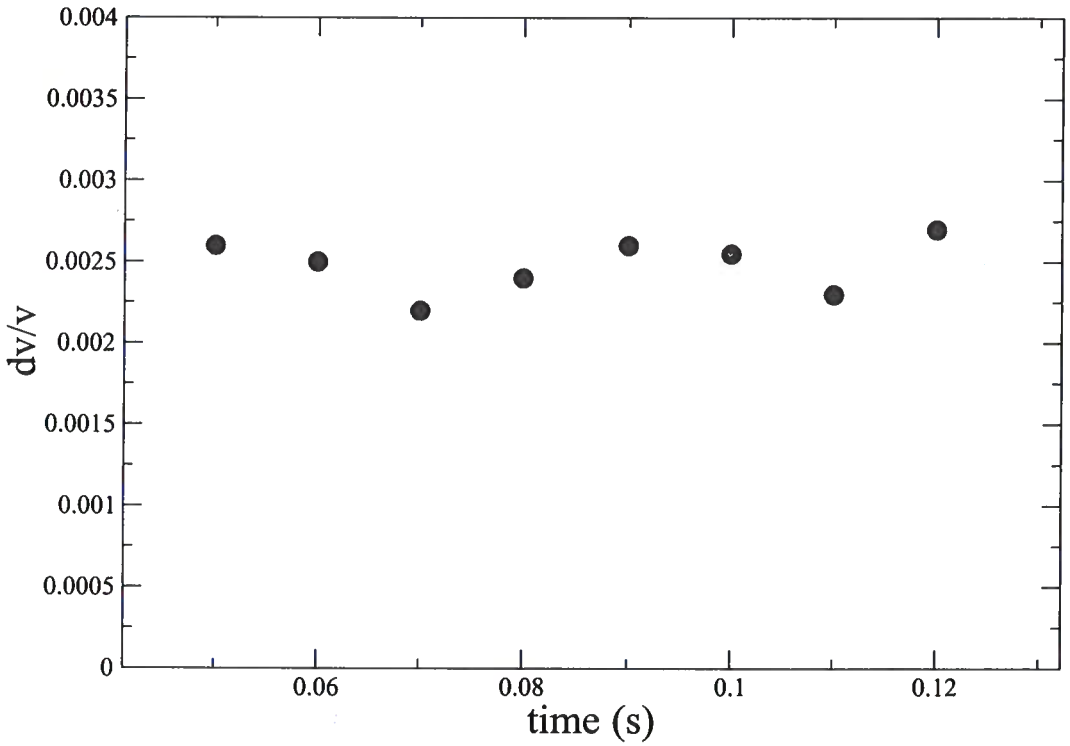

Figure 4.6. Velocity change estimates for eight non-overlapping windows with different center times. The mean velocity change is 0.25 % and the standard deviation is 0.02 %.

δt by the lag of the maximum of the cross-correlation function given by equation 4.2. The cross-correlation function for the coda measurements in Figure 4.3c is shown in Figure 4.4. By computing δt for multiple, non-overlapping, time windows we obtain increasing values for δt for increasing total travel-times t (Figure 4.4). These are independent estimates of travel-time perturbations for given total travel times.

Because of the low sensitivity of early arriving waves, δt is for the early arriving waves smaller than the sampling interval of the seismic record. This leads to large uncertainties in the estimated velocity changes (equation 4.1). For that reason, we don't estimate velocity changes from the early part of the signal (δt smaller than sampling interval). Furthermore, we assume a constant velocity change over the whole area sampled by the waves. If that assumption holds, then the time lag δt grows linearly with total travel-time t (Grêt *et al.*, 2004c). If the velocity change is localized, however, then there is a non-linear dependency of δt on t (Pacheco, 2003). In our experiment we introduce a localized stress change around the pressure cell and would therefore expect a non-linear dependency of δt on t. Nonetheless, we measure a linear increase of δt with time t (figure 4.5). In order to explain this contradiction, we speculate that the wave energy that leaks out of the pillar does not come back. Hence, the waves measured for the entire duration of recording are trapped in the pillar and sample only some portion of the rock mass in the pillar. In other words, the induced stress change is locally confined but so is the area sampled by the recorded waves.

We compute the relative velocity change in the rock $\delta v/v$ from equation (4.1). As previously explained, we obtain the phase shift δt from the cross-correlation function and the total travel-time from the time-location of the data window. Since we use non-overlapping time windows, we get multiple, independent estimates of $\delta v/v$ (figure 4.6), that provides a mean relative velocity change and standard deviation. Note that we are measuring a very small relative velocity change of the order of 0.2 %. This is a value which would be very hard or even impossible to detect with a travel-time tomography, even with the most accurate instrumentation.

4.7 Monitoring stress change

In order to test the accuracy of the method we compute the relative velocity change for four pressure differences of equal amount (1200 psi) but with different starting pressures (0, 600, 800 and 1000 psi, see table 4.7). The measured velocity changes for a stress difference of 1200 psi each, agree well with the exception of the initial stress increase from 0 psi. The large velocity increase with the initial stress change can be explained by the closure of void space, e.g. pores and cracks (Hubbert & Willis, 1957; Friedel *et al.*, 1995). During the installation of the slit, probably new cracks where formed and old ones opened. These cracks are closed back by increasing the pressure in the cell from 0 to 600 psi, which is approximately the pressure from the overburden and corresponds to the stress state before the installation of the slit. The velocity increase is greatest with an early increment increase in stress because of this change, voids are easily closed.

The relative velocity change, due to a pressure increase of 1200 psi, measured with coda wave interferometry is consistently lower than what we would expect from textbook

Stress difference	*Mean rel. velocity change from CWI*	*Standard deviation from CWI*
0-1200 psi	0.25%	0.02%
600 – 1800 psi	0.14%	0.05%
800 – 2000 psi	0.15%	0.02%
1000 – 2200 psi	0.13%	0.03%

Figure 4.7. Table of measured relative velocity change for 1200 psi pressure difference in the cell and four different starting pressures. The standard deviation is calculated from the eight non-overlapping windows

values of about 0.4 % (Carmichael, 1982). In the analysis we assume that the stress change occurs in the entire pillar, which is not the case in this experiment. What we measure with coda wave interferometry is a mean velocity change over the full pillar area. This results in a lower value of velocity change, since some areas of the pillar are not affected by the stress change. An increase of 1200 psi in the entire pillar would result in a constant velocity change in the whole area sampled by the coda waves. In that case, coda wave interferometry would measure a larger average velocity change. In other words, coda wave interferometry would be even more sensitive to a stress change in the entire pillar and could monitor smaller stress changes than 1200 psi.

4.8 Discussion

The pressure cell changes the stress in a limited area close to the slot. We can not tell from the coda waves alone where the stress change is located. In practice, one could complement coda wave interferometry with local measurements of stress change or deformation. Commonly used instruments are strain gages (Hawkes & Bailey, 1973; Hanna, 1985), extensometers (Joass, 1993; Sheppard & Murie, 1992) tiltmeters (Joass, 1993) and one-way travel-time seismic tomography. Seismic tomography in particular lends itselfs to a natural combination with coda wave interferometry, since the instrumentation can be shared by the two methods, where tomography gives an image of the stress in the pillar (provided we can meeasure the change in first arrivals) and coda wave interferometry provides the sensitivity to monitor small stress changes.

We found that the smallest pressure difference that can reliably be detected in our experiment with coda waves is 1200 psi. We introduced a localized stress change. When the same 1200 psi stress change is distributed over the entire pillar, the velocity would change in the whole area sampled by the coda waves. In that case it is possible to measure smaller stress differences.

In this study we do not distinguish between S-, P- and surface waves, but an extension of coda wave interferometry for elastic waves is given by Snieder (2002) who shows that coda wave interferometry is much more sensitive to S-wave than to P-wave velocity change. In particular, for a Poisson medium the coda wave interferometry velocity change is given by

$$\frac{\delta v}{v} \approx 0.09\frac{\delta v_P}{v_P} + 0.91\frac{\delta v_S}{v_S}, \tag{4.3}$$

where v_S and v_P are S- and P-wave velocities and δv_S and δv_P are the velocity changes for S and P-waves, respectively.

4.9 Conclusions

We demonstrate that coda wave interferometry is a sensitive tool to monitor stress changes in an underground mining environment. It is a suitable method when classical tomography is not sensitive enough to measure a stress change. In addition, coda wave

interferometry needs only one receiver (geophone) and a hammer source, this is a fraction of the hardware requirement for travel-time tomography. This makes coda wave interferometry inexpensive and easy to install. The data processing is basic and can easily be built in a simple, stand-alone instrument. An instrument can be developed that is a fully automated monitoring system and resists the rough mining environment.

The results of our study are sufficiently encouraging to repeat the experiments in an operating mine. The method has potential for monitoring rates of stress change and deformation in the rock mass surrounding excavations both in underground and surface mines.

4.10 Acknowledgments

We are thankful to Dave Mosch, who is making the mine a safe place for us to work. Doug Scott and his collegues for installing the pressure cell in the pillar. Thanks to Matt Haney, Brian Zadler and Douglas Klepacki who helped preparing the experiment and swinging the hammer. We are also greatfull to Mike Batzle for his continuous help with instruments, pumps and everything else needed to make the experiment work. Thanks to John Scales for the stimulating discussions about wave propagation. This work was supported by the NSF (EAR-0106668). We also thank the members of the Center for Wave Phenomena and the Physical Acoustics Laboratory for stimulating discussions.

Chapter 5

Monitoring rapid temporal change in a Volcano with Coda Wave Interferometry

5.1 Abstract

Multiply scattered waves dominate the late part of the seismic coda. Small changes in a medium, which have no detectable influence on the first arrivals, are amplified by the multiple scattering and may be seen readily in the coda. We exploit this idea using *Coda Wave Interferometry* to monitor temporal changes in the subsurface of the Mt. Erebus Volcano, Antarctica. Mt. Erebus is one of the few volcanoes known to have a convecting lava lake. The convection provides a repeating seismic source producing seismic energy that propagates through the strongly scattering geology in the volcano. Over a time period of two months, the first arrivals of the seismic waves are highly reproducible. For the first month this is also the case for the coda. At a certain moment, the seismic coda decorrelates rapidly. This indicates a rapid change in the subsurface of the volcano, a change that could not be detected by means of single scattered seismic waves.

5.2 Introduction

The coda of a waveform consists of that part of the signal after the directly arriving phases (Aki, 1969; Aki & Chouet, 1975). At late times the coda is dominated by multiply scattered waves. Geophysical applications based on coda waves include earthquake prediction (Aki, 1985; Sato, 1986), earthquake-magnitude estimation (Lee *et al.*, 1972), volcano monitoring (Aki & Ferrazzini, 2000; Fehler *et al.*, 1998) and monitoring of temporal changes in the subsurface (Robinson, 1987; Chouet, 1979; Revenaugh, 1995; Poupinet *et al.*, 1984). Laboratory applications include Diffusive Wave Spectroscopy (Cowan *et al.*, 2002), reversed time imaging (Fink, 1997), and medical imaging (Li *et al.*, 1997).

Small changes in a medium, which would have no detectable influence on the first arrivals, are amplified by the multiple scattering and may be seen readily in the coda. We have previously exploited ultrasonic coda waves to study non-linear temperature dependence of velocity in granite (Snieder *et al.*, 2002). This non-linearity is related to acoustic emissions during thermal cracking (Fredrich & Wong, 1986). In contrast to other methods which use multiply scattered energy, the phase information of the coda is a central part of our analysis. There are many other possible applications of *Coda Wave Interferometry* in geophysics, including dam monitoring, time-lapse reservoir characterization, and rock physics.

Figure 5.1. Mt. Erebus, Ross Island, Antarctica, is currently the most active volcano in Antarctica. The summit of Mt. Erebus contains a persistent convecting lava lake which undergoes several strombolian style eruptions daily. Within the past year (2003), small ash eruptions and a small lava flow have also been observed coming from vents near the lava lake. Aerial view of the summit plateau and volcanic plume of Mt. Erebus.

The subsurface in the regions of volcanoes is highly inhomogeneous. Such highly scattering media are attractive for the study of multiply scattering of seismic waves (Wegler & Luehr, 2001). In this paper we show the application of Coda Wave Interferometry for monitoring changes in the subsurface of Mt. Erebus, Antarctica.

5.3 Mount Erebus, it's eruptions and the seismic network

Mt. Erebus, Ross Island, Antarctica, is currently the most active volcano in Antarctica. The summit of Mt. Erebus contains a persistent convecting lava lake that undergoes several strombolian style eruptions daily (Rowe *et al.*, 1998). Within the past year, small ash eruptions and even a small lava flow have been observed coming from vents near the lava lake (See Figure 5.1 for a photo).

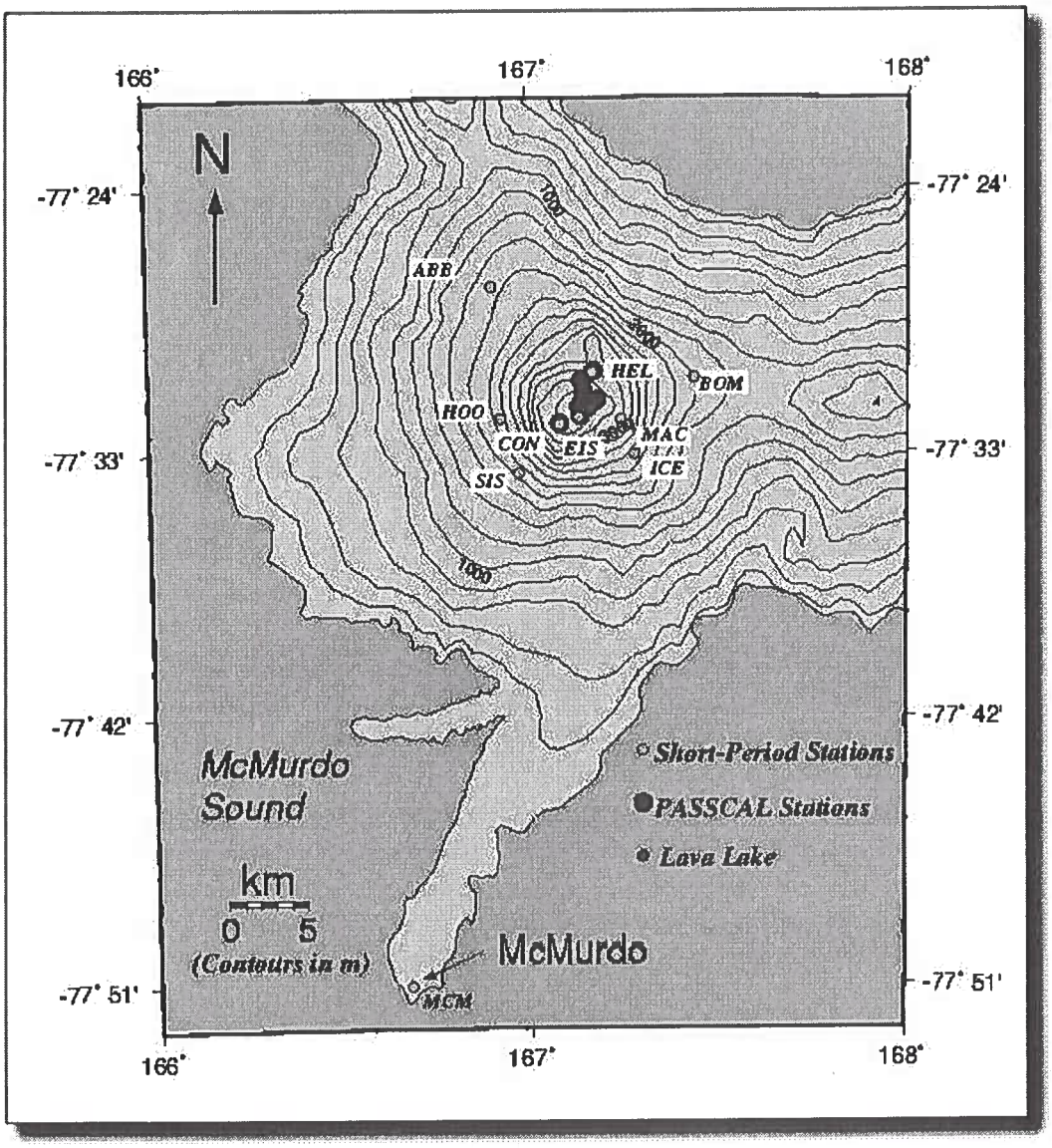

Figure 5.2. Location of the permanent network of nine, single-component short-period (1-Hz) seismometers and one three-component, 1-Hz station. A infrasonic microphone is co-located with the summit seismic station.

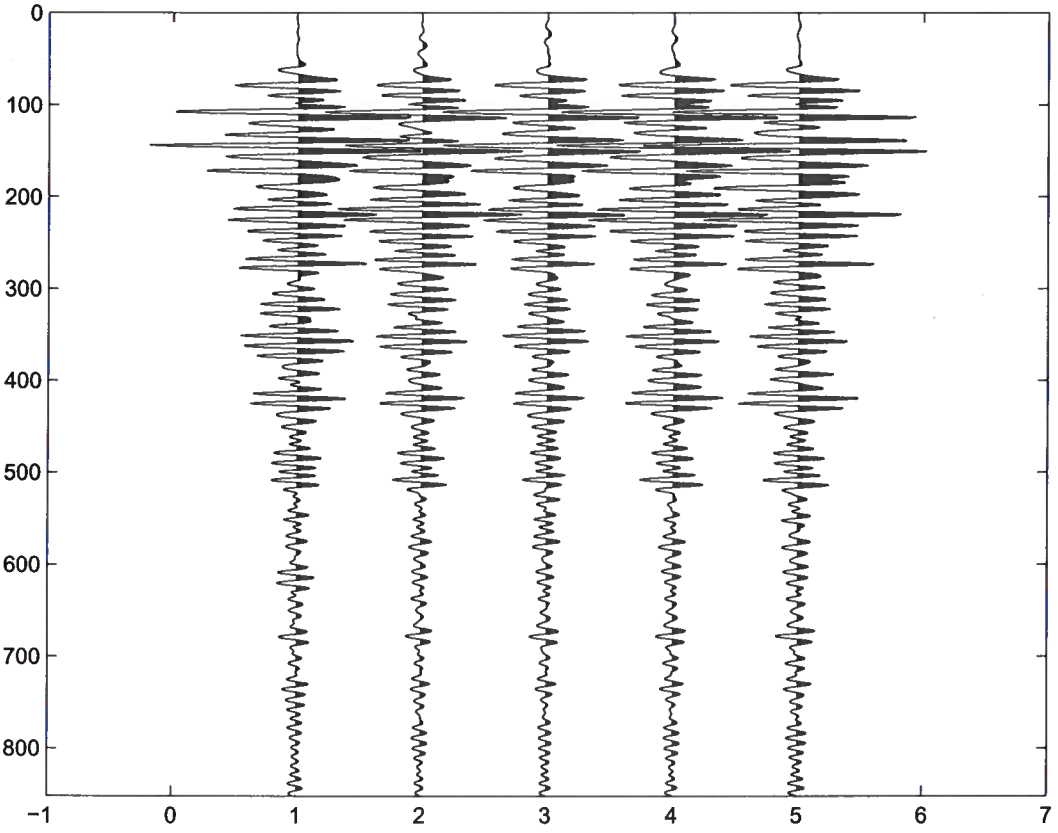

Figure 5.3. Five different events recorded at the broadband seismometer station E1S. Event one occurred on Dec. 12th, event two on Dec. 13th, event three on Dec. 14th and events four and five on Dec. 15th. Note how well the waveforms are reproducible over a time frame of days.

The mountain is currently instrumented with a permanent network of nine, single-component short-period (1-Hz) seismometers and one three-component, 1-Hz station, as well as an infrasonic microphone co-located with the summit seismic station (See Figure 5.2). In 1999, a permanent broadband seismometer was installed along with a tilt-meter and wind speed and direction instrumentation at station E1S. Stations are powered by gel-cell batteries recharged by solar panels; many short-period stations now operate throughout the Austral winter, thanks to sufficient battery capacity combined with their low power consumption (approximately one Watt) (See (Aster *et al.*, 2003) for a more detailed description of the instrumentation at Mt. Erebus).

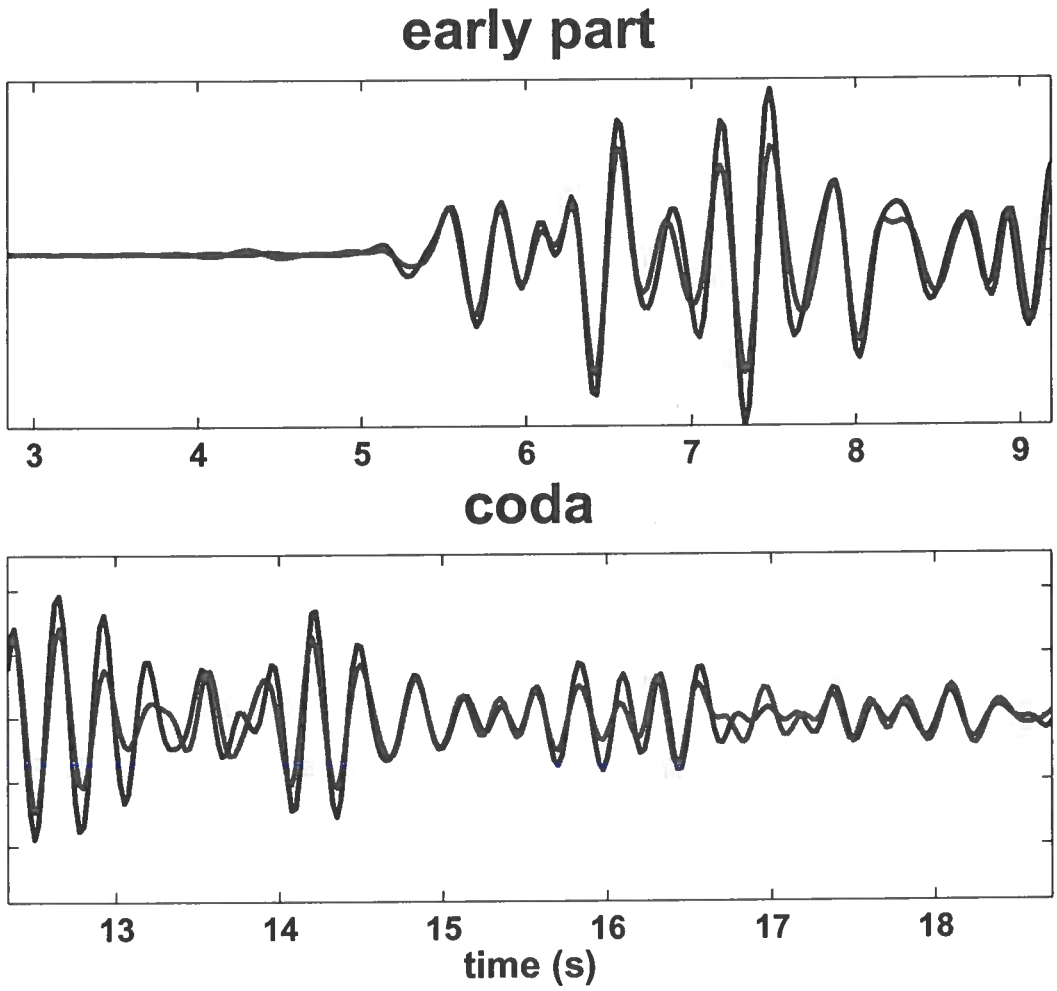

Figure 5.4. The top of the figure shows the early part of event one on Dec. 12th (red line) and event two on Dec. 13th (blue line), plotted on top of each other. The bottom of the figure shows the later part of the same events.

5.4 Reproducible seismic events at Mount Erebus

Figure 5.3 shows five different events recorded at the broadband seismometer station E1S. Event one occurred on Dec. 12, event two on Dec. 13, event three on Dec. 14 and events four and five on Dec. 15, 1999. Note the reproducibility of the waveforms over a time frame of several days. Even when looking at short time windows of the seismic data, the events are virtually identical (Figure 5.4). Not only are the first arrivals reproducible, the seismic codas of the two events overlap equally well. This means that during the period when those earthquakes were recorded, the source, receiver, and subsurface remained invariant. If either of the three had changed, the seismic waveforms would have changed too.

5.5 Decorrelation of coda waves

Figure 5.5 shows the same comparison of two seismic events, except that the events occurred two weeks apart in time. The early parts still correlate extremely well but there is a larger difference in the late parts of the waveforms. Since the source signature (early window) is reproducible, we assume that the seismic source, a strombolian eruption, for the two events and the seismometer remained invariant. Since the codas for the two events are different, however, the medium through which the waves have traveled through must have altered. We use this difference to monitor a change in the volcano. That change is too small to have an effect on the early part of the waveforms. In order to quantify the difference in waveforms, we compute the maximum of the cross-correlation function for the early parts and the late parts, respectively (Figure 5.6). In the top part of figure 5.6, the correlations for the early parts (source signature) are high (around 0.9) over the whole two month period. For the later part of the waveforms, however, the correlations drop sharply around the 8th of January 2000. This means, that around that date something has changed in the volcano that can't be monitored with the early part of the waveforms.

5.6 Measurements at different locations

We have other seismic stations on Mt. Erebus that also show this change in coda waves. This excludes nonlinear artifacts of the instrument at the station E1S. We processed four more stations in the same manner as previously described. We find a similar jump in correlation coefficients at all four stations (ABB, CON, HEL and HOO)(Figure 5.7 and 5.8). The correlation-level is in general lower than at station E1S because of the higher noise level and the difference in instrument type (some measurements are clipped). Stations ABB, CON, HEL and HOO are equipped with short-period (1-Hz) seismometers with a lower dynamic range than the broadband seismometer at station E1S.

It is difficult to determine what is the cause of the change in the subsurface because of the complex paths that multiply scattered waves travel. However, there are some scenarios we can clearly exclude. The decorrelation of the coda waves can't be due to a change in seismic velocity only since that would lead to a linear increase in phase-shift with increasing traveltime (Snieder *et al.*, 2002). We can also exclude all gradual changes with time since

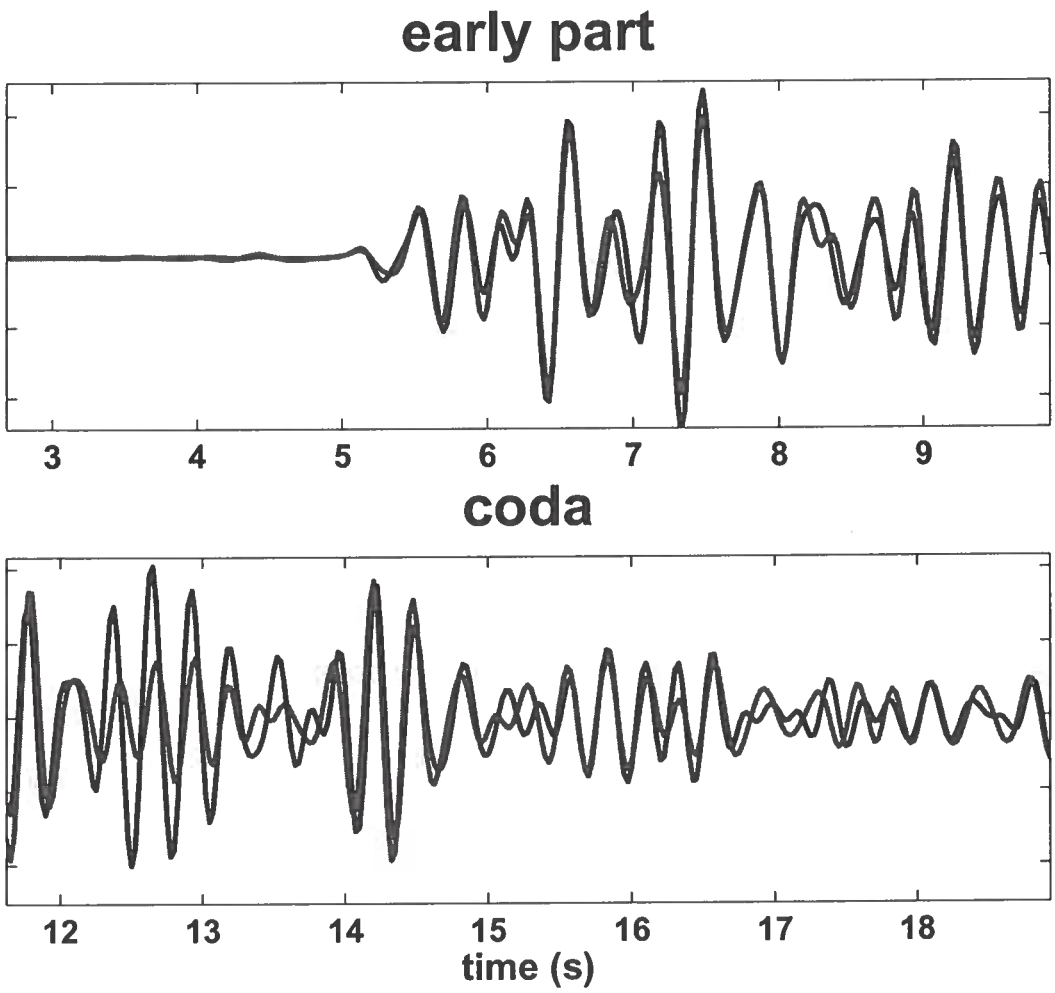

Figure 5.5. A plot similar to the previous one but the two events here occurred two weeks apart. The early parts still correlate extremely well but there is a larger difference in the late parts of the waveforms. We use this difference to monitor a change in the volcano. That change is too small to have an effect on the early part of the waveforms. In order to quantify the difference in waveforms, we compute the correlation coefficients for the early parts and the late parts, respectively.

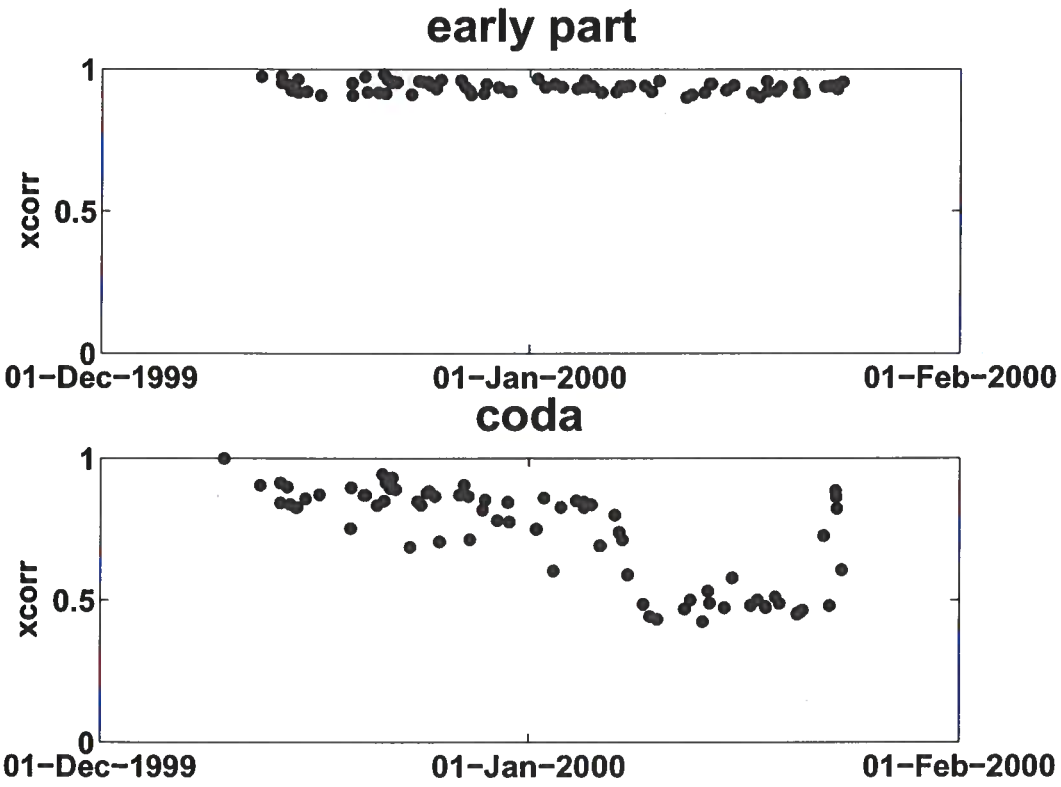

Figure 5.6. In the top of the figure the correlation coefficients (all events are correlated with event number one) for the early parts stay high (around 0.9) over the whole two month period. For the later part of the waveforms, however, the correlation coefficients have a sudden drop around the 8th of January 2000. This means, that around January 8 something has changed in the volcano that can't be seen in the early part of the waveforms.

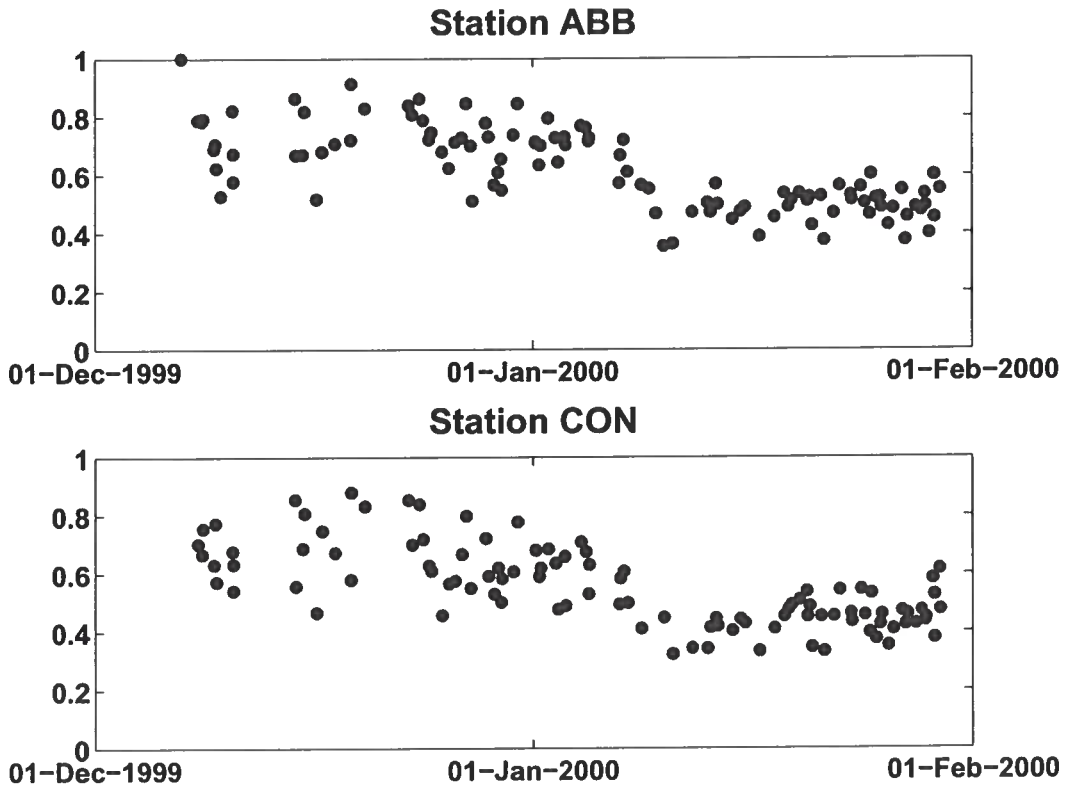

Figure 5.7. In order to exclude nonlinear artifacts of the instrument at station E1S, we processed four other stations in the same manner. We find a similar jump in correlation coefficients at all four stations (ABB, CON shown here). The correlation level is in general lower than at station E1S because of the higher noise level and the difference in instrument type (some measurements are clipped). Station ABB, CON, HEL and HOO are equipped with short-period (1-Hz) seismometers.

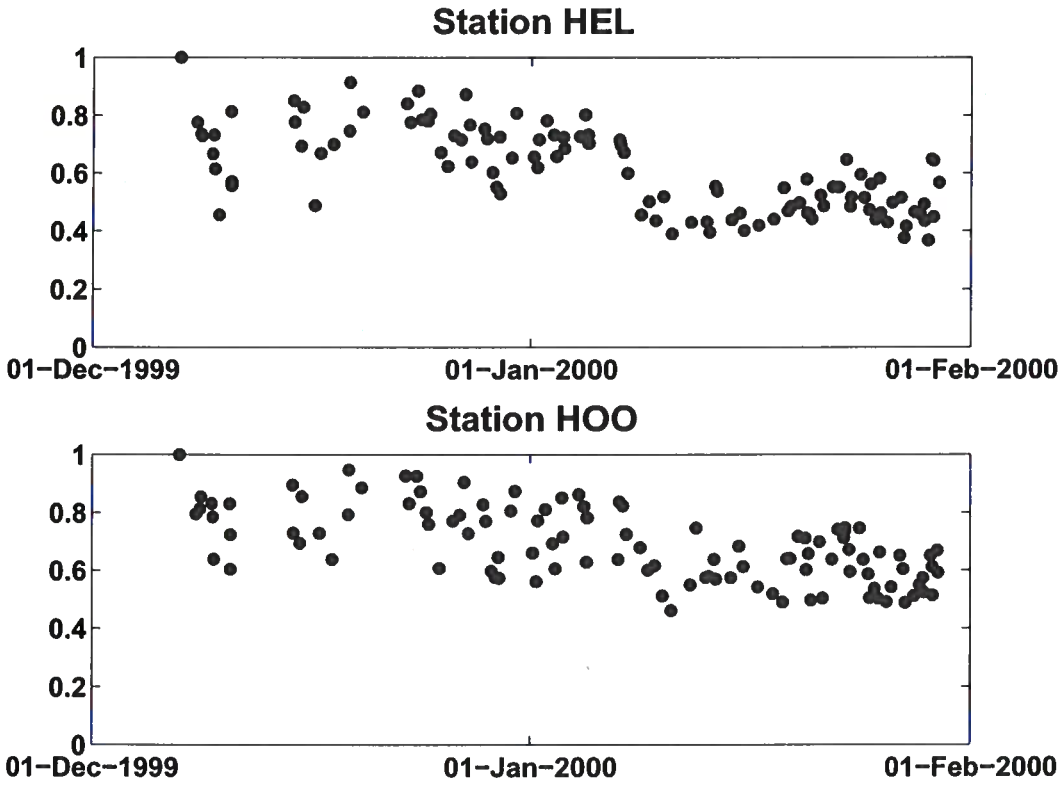

Figure 5.8. Time shifted orrelation coefficient of coda waves (in respect to the first event) for stations HEL and HOO, showing the same rapid drop in correlation as the previous stations.

the time of change can be restricted to a few days around January, 8, 2000. This leaves sudden events such as landslides, movement of lava and associated thermal change, sudden fluid migration, or slips on faults.

5.7 Conclusions

The strombolian style eruptions at Mt. Erebus provide a repeatable source for monitoring the volcano with seismic methods. The geology of volcanoes is known to be highly scattering. The seismic waveforms recorded around the volcano are highly reproducible, not only their early arriving phases but also the seismic coda. The source signature remains virtually the same over the whole two-month period. The coda, however, has a distinct drop in correlation around January 8, which suggests a change in the subsurface of the volcano. The change is not gradual but occurs within a time frame of a few days. Furthermore, the change is so small that it has no effect on the first arrivals but it's influence can be seen in the coda because of its higher sensitivity to a change in the medium.

5.8 Acknowledgments

This work was supported by the NSF (EAR-0106668). We also thank the members of the Center for Wave Phenomena and the Physical Acoustics Laboratory for stimulating discussions.

Chapter 6

Time versus frequency resolution of small changes

6.1 Abstract

Some experiments are most conveniently thought of as being performed in the time-domain, some in the frequency-domain, and some use a hybrid approach. Does the domain make any difference in the ultimate resolution of the experiment? Or can the details of the experiment always be tweaked so that the different approaches give the same underlying answer? We consider a toy experiment from optics which lends itself to many such arrangements. Using both time and frequency measurements, and taking into account the influence of noise, finite dynamic range, attenuation, and the duration of the measurement, we address the question for each formulation: how small a change in the system can we make and still detect it?

6.2 Overview

In many cases, the same basic experiment can be performed in the time or frequency domain–or some hybrid. An example is spectroscopy. At one extreme, a narow-band, frequency tunable source such as a laser or microwave oscillator can be used to probe a system and directly measure the system's transfer function (Migliori & Sarrao, 1997). In other situations it might be more convenient to drive the system with a broad-band signal such as a pulse and look at the impulse-response, as in cavity ring-down spectroscopy (Hodges *et al.*, 2004) or coda wave interferometry (Snieder *et al.*, 2002). Although, loosely speaking the methods are equivalent by virtue of the invertability of Fourier transform, in fact the experimental issues can be very different in these two extreme cases; for instance, what is the difference between pulsing a system many times and averaging versus driving the system at a fixed frequencies for a long time and then sweeping the frequency? It is by no means obvious that the sensitivity of the time or frequency domain measurement of a particular quantity is the same.

We analyze these issues in the context of a particular experiment. Consider two plane parallel reflectors as in a Fabrey-Perot etalon (Figure 6.1). Let L denote the distance between the mirrors and N the index of refraction of the medium between the mirrors; i.e., the cavity. We consider both wavepackets and monochromatic plane waves normally incident on the etalon, and we treat the etalon as being large in the vertical and out-of-plane directions, so we only deal with propagation along the x-axis. The latter case gives the well-known result from optics, although in the analysis that follows we look at both the

fields and the intensities since the same experiment can be performed with, for example, ultrasonic transducers or microwave transceivers, where the amplitude and phase of the field can be measured. To make the situation realistic we consider finite measurements involving finite dynamic range and non-zero ambient noise levels. Further, the index could be complex, allowing for attenuation.

Ultimately our goal is to consider the following problem. Suppose that a small change δN is made in the index of refraction between the two mirrors. If the unperturbed index is N_{unp}, then the perturbed index is $N_{pert} = N_{unp} + \delta N$. How big does δN have to be before it can be detected? We treat three domains for the experiment:

- **time** Launch a (Gaussian) wavepacket into the etalon and measure the field or intensity up to a certain finite time T_{max}. All data analysis is done in the time domain. For instance, we could look at the cross correlation of the signals at T_{max} before and after the change δN as in coda-wave interferometry.

- **frequency** Launch a monochromatic plane wave into the etalon; a tunable laser could be used, for instance, or an ultrasound transducer connected to a function generator. In any case, we suppose that we can control the frequency and use some sort of synchronous detection to make the measurement, such as a lock-in amplifier or a spectrometer.

- **time-frequency** This will be the same as the time domain above, but instead of analyzing the data in the time domain we Fourier transform and look at, for example, the power spectrum, as the etalon rings down. This allows us to incorporate the interference of the pulses by integrating over all time.

6.3 The Fabry-Perot etalon

The Fabry-Perot etalon is discussed in virtually every optics text; for example, see (Born & Wolf, 199) and (Lauterborn & Kurz, 2003). Our goal is to find the transmitted intensity of the system as a function of the reflectivity of the mirrors r, the index of refraction N, and frequency of the incoming light ν. We refer to Figure 6.1 throughout the derivation.

6.3.1 Time versus frequency in the ideal case

On one's first pass through this problem, the connections between the time and frequency domain analysis are subtle, so we go through the problem in some detail. The simplest place to start is with an idealized wave-packet consisting of an infinitely narrow impulse (delta function) incident on the etalon from the left. That is, the incident traveling pulse E_i has the form:

$$E_i = E_0 \delta(\omega\tau - kx).$$

We will use τ for time to avoid confusion with the transmission coefficient.

The reflected field is defined as E_r, the transmitted wave field as E_t. If there is no loss upon reflection and transmission at the mirrors, we have a conservation of energy, which means $r^2 + t^2 = 1$, where $r = E_r/E_i$ and $t = E_t/E_i$ are the reflection and transmission coefficients of the isolated mirrors.

When the pulse hits the etalon it is split up into an infinite number of transmitted and reflected pulses. Each transmitted pulse is diminished by a factor of t^2, where t is the reflection coefficient of each (identical) mirror, and another factor of r^{2m}, r is the reflection coefficient of each mirror and m is the number of bounces inside the etalon. The geometry is illustrated in Figure 6.1. In addition to the amplitude loss, each bounce inside the etalon results in time delay of $2NL/c_0$, where N is the index inside the cavity, L is the distance between the mirrors and c_0 is the speed of light.

Since we are going to fix our detector position x, we only treat the associated time shifts. The time $\tau = 0$ corresponds to the time at which we launch our pulse into the etalon so that the first transmitted pulse arrives at the detector a time $\tau = NL/c_0$ later. Hence the transmitted field is given by

$$\begin{aligned} E_t(\tau) = (E_0 t^2)\delta(\tau - \frac{NL}{c_0}) + r^2(E_0 t^2)\delta(\tau - \frac{3NL}{c_0}) \\ + r^4(E_0 t^2)\delta(\tau - \frac{5NL}{c_0}) + \cdots \\ + r^{2(m-1)}(E_0 t^2)\delta(\tau - \frac{2(m-1)LN}{c_0}) + \cdots \end{aligned} \tag{6.1}$$

Even though we are doing a time-domain experiment (an incident pulse), a great simplification of this result occurs if we Fourier transform it. So, let us multiply this expression for E_t by $e^{-i\omega\tau}$ and integrate:

$$E_t(\omega) = \int_{-\infty}^{\infty} e^{-i\omega\tau} E_t(\tau).$$

Each δ-function in the transmitted field will Fourier-transform to an $e^{i\omega\tau}$ term with appropriate delay. The expression for the m-th term is:

$$r^{2(m-1)}(E_0 t^2) e^{-i\omega \frac{2(m-1)LN}{c_0}}.$$

So we have the frequency-domain representation of the transmitted field of an impulse

$$\begin{aligned} E_t(\omega) = (E_0 t^2) e^{i\omega \frac{NL}{c_0}} + r^2(E_0 t^2) e^{i\omega \frac{3NL}{c_0}} \\ + r^4(E_0 t^2) e^{i\omega \frac{5NL}{c_0}} + \cdots \\ + r^{2(m-1)}(E_0 t^2) e^{i\omega \frac{2(m-1)LN}{c_0}} + \cdots \end{aligned} \tag{6.2}$$

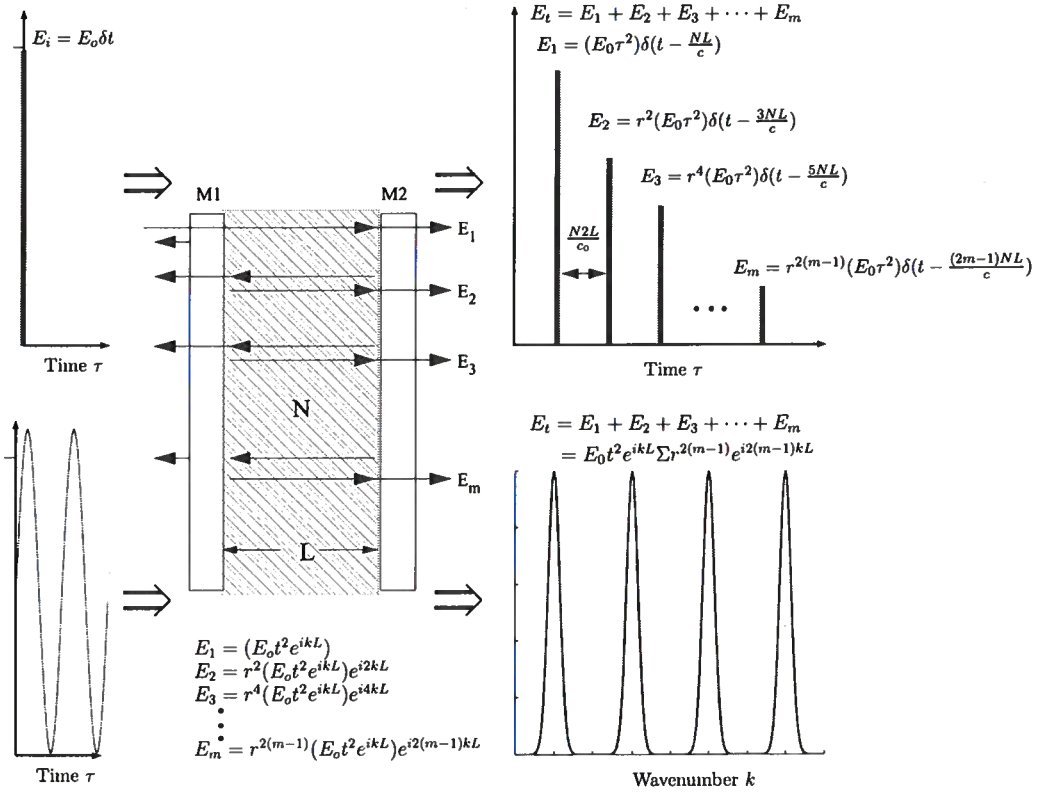

Figure 6.1. The canonical experiment. A plane wave or Gaussian wavepacket (*left*) is incident into an etalon (*center*) of spacing L from the left. Each mirror has the same properties (reflection/transmission coefficients) and the space between the mirrors is filled with a uniform medium of index N. The index may be complex. A train of Gaussian pulses is transmitted through etalon (*right*). There is no dispersion in this example, and the amplitude decays by r^2 with each transmitted pulse.

We recognize that this is a geometric series of the form

$$a + ab + ab^2 + ab^3 + ... + ab^{m-1} = \frac{a - bl}{1 - b}, \tag{6.3}$$

where $l = ab^{m-1}$ is the last term in the series, and $r \neq 1$. For us, $a = 1$ and $b = r^2 e^{2i\omega NL/c_0}$, which gives us

$$E_T = E_0 t^2 e^{i\omega NL/c_0} \frac{1 - r^{2m} e^{2mi\omega NL/c_0}}{1 - r^2 e^{2i\omega NL/c_0}}. \tag{6.4}$$

At this point we need to distinguish what type of detection we are using. In the case of ultrasonics and microwave detectors, it is possible to record the full field E that includes amplitude and phase information. However, in an optical experiment one cannot directly measure the phase of the wavefield, all we have is the time averaged intensity over some measurement duration. The transmitted intensity for the Fabry-Perot experiment is:

$$I_T = E_T E_T^* = E_0 E_0^* t^4 \frac{(1 + r^{4m} - 2r^{2m}\cos(2mNL\omega/c_0))^2}{(1 - r^2 e^{i\delta})(1 - r^2 e^{-i\delta})} \tag{6.5}$$

where $\delta = 2\omega NL/c_0$, the phase shift for one round trip through the etalon.

We can rewrite Equation 6.5 as

$$I_t = \frac{E_0 E_0^* (1 - r^2)^2 (1 + r^{4m} - 2r^{2m}\cos(2mNL\omega/c_0))^2}{1 + r^4 - 2r^2\cos(\delta)} \tag{6.6}$$

or, normalizing,

$$T = \frac{I_t}{I_i} = (1 - r^2)^2 \frac{(1 + r^{4m} - 2r^{2m}\cos(2mNL\omega/c_0))^2}{1 + r^4 - 2r^2\cos(\delta)}. \tag{6.7}$$

In the limit that the measurement time $T_{MAX} \to \infty$, there are an infinite number of reflections and since $r < 1$, we are left with

$$T = \frac{I_t}{I_i} = \frac{(1 - r^2)^2}{1 + r^4 - 2r^2\cos(\delta)}. \tag{6.8}$$

In the final simplification, we use the identity $\cos(\theta) = 1 - 2\sin^2(\theta/2)$ to obtain the well-known form

$$T = \frac{I_t}{I_i} = \frac{1}{1 + K\sin^2(NL\omega/c_0)} \tag{6.9}$$

where $K = \left(2r/(1 - r)^2\right)$. Figure 6.2 shows a plot of the transmitted intensity as a function of normalized wavenumber.

To recap, we launched a pulse into the etalon and got out an infinite train of pulses scaled by powers of the reflection coefficient. To simplify this infinite sum we Fourier trans-

form to the frequency domain and obtained a geometric series for the transmitted intensity. In the frequency domain, the transmitted intensity shows an interesting dependence on the properties of the mirror that might be surprising with no other information than the time series of pulses emerging from the etalon. Even in the case that the pulses are strictly non-overlapping in time, the frequency domain plot (Figure 6.2) shows the clear signature of interference.

Readers familiar with this sort of argument will have already observed that the final result for the spike-transmission coefficient in the frequency domain is the same as if we had started with time-harmonic plane waves and stayed in the time domain.

6.3.2 Thinking in frequency from the beginning

Imagine a standing wave between the two mirrors. The lowest frequency such wave with "clamped" boundary conditions $E(x = 0, \tau) = E(x = L, \tau) = 0$ (putting the origin of the x coordinates on the left mirror) is:

$$E(x, \tau) \propto \sin(m\pi x/L)e^{i\omega\tau}$$

But this can also be written as a sum two traveling waves going in opposite directions. If we adjust the relative phase of the two traveling waves we can make them cancel at the ends of the cavity, thus giving a proper standing wave. Another way of thinking about this is that a standing wave is really a traveling wave that bounces back and forth an infinite number of times.

The intensity is periodic for both L and ω, hence we will see characteristic interference effects either by sweeping through frequency or changing the cavity length. Just like standing waves on a string, the first mode occurs when $\lambda/2 = LN$, the second when $2\lambda/2 = LN$, and so on. This is the same as saying that standing-waves occur when kLN is an integer multiple of π:

$$m\pi = k_m LN = \frac{2\pi}{\lambda_n} LN. \tag{6.10}$$

Figure 6.2 shows the intensity as a function of frequency of the optical resonator. This is where an epiphany may occur, and what makes this apparently trivial problem so interesting. Imagine that we have only one mirror with a reflectivity of 0.999, or 99.9% and that the reflectivity is independent of frequency over some range (readily do-able). A photo-detector downstream of the mirror will measure 0.1% of the incident light. However, by adding a second mirror, the etalon transmits 100% of the incident light at certain frequencies! In effect, we have created an optical filter. The two defining parameters of every Fabry-Perot etalon are the free spectral range (FSR) and the finesse. The free spectral range is the distance, in frequency, between successive transmission maxima. This can be calculated by

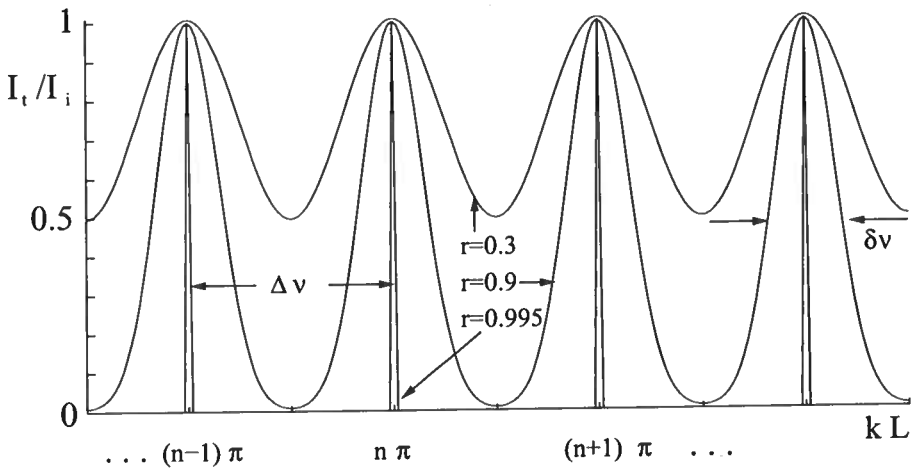

Figure 6.2. The transmitted intensity as a function of normalized wavenumber ($\omega = kc$) for different values of reflectivity. Notice that the transmission is 1 at the eigenfrequencies no matter what reflectivity, whereas in the time domain T_max decays as $1/log(r)$.

using Equation 6.10, and that $k_n = 2\pi/\lambda_n$ where $\lambda_n = c_0/N\nu_n$.

$$k_{n+1}LN - k_nLN = (n+1)\pi - n\pi = \pi \tag{6.11}$$

$$(k_{n+1} - k_n)LN = \frac{2\pi LN}{c_0}(\nu_{n+1} - \nu_n) = \frac{2\pi LN}{c_0}\Delta\nu \tag{6.12}$$

Equating the two, we find the free spectral range to be $\Delta\nu = c_0/2\pi LN$. If we denote the width of the peaks at half maximum transmission ($T = 1/2$) as δ_ν, then by using these two definitions, we establish the concept of finesse,

$$F = \frac{\Delta\nu}{\delta\nu} = \frac{\pi r}{1 - r^2}, \tag{6.13}$$

a dimensionless quantity that characterizes the sharpness of the peaks. A higher finesse means we can resolve more spectral lines within our free spectral range, hence a better interferometer.

6.4 A canonical experiment

Real measurements always have noise, a finite sampling interval and dynamic range. They might be different from instrument to instrument but we want to know which ones influence resolution and how.

In order to avoid the complexity associated with correlated noise, we assume the noise in our data is independent and white (contains all frequencies). Correlated noise can be included but makes the calculations harder. In the case of uncorrelated noise we can reduce the noise level by averaging multiple realizations of the measurement. Let ϵ be the rms (root mean squared) noise level after averaging and ϵ_o is the rms noise of a single realization, then

$$\epsilon = \frac{\epsilon_o}{\sqrt{n}}, \tag{6.14}$$

where n is the number of averaged realizations.

The second limitation we face is the finite dynamic range DR of a particular instrument. The dynamic range is the ratio between the largest and smallest measurable value; it is commonly expressed in decibels (dB):

$$DR = 10\, log_{10}\left(\frac{P_{max}}{P_{min}}\right) dB, \tag{6.15}$$

where P_{max} is the maximum recordable power and P_{min} the minimum non-zero recordable power. If we have an instrument that measures in voltage, then the power P is given by E^2/Z, where E is the voltage and Z is the impedance of the instrument. Hence,

$$DR = 10\, log_{10}\left(\frac{{E_{max}}^2/Z_{max}}{{E_{min}}^2/Z_{min}}\right) dB, \tag{6.16}$$

where E_{max} is the maximum recordable voltage and E_{min} is the minimum recordable voltage. If the impedance is constant for all measurements ($Z_{max} = Z_{min}$), equation (6.16) becomes

$$DR = 20\, log_{10}\left(\frac{E_{max}}{E_{min}}\right) dB. \tag{6.17}$$

DR is often expressed in number of bits B and the relationship between DR in decibel and B is

$$DR = 20\, log_{10}\left(2^B\right) dB. \tag{6.18}$$

Hence, a 14-bit instrument (that is, an instrument with a 14-bit analog to digital converter) will have a dynamic range of $DR = 84.29dB$. If we adjust the amplification such that the highest signal amplitude is 1 Volt and using equation (6.17) we obtain a smallest recordable voltage E_{min} of $6.2 \cdot 10^{-5}$ Volts.

If E_{min} is the smallest measurable increment of our instrument, then we can reduce ϵ to be lower than E_{min} by averaging $n = (\epsilon_o/E_{min})^2$ times. After that we can treat the noise-free case and E_{min} will be the limiting factor for the amplitude resolution. If we can't average n times, however, replacing E_{min} by ϵ in the remainder of the calculation will lead to the right answer, including noise.

Continuing this example we can see that the last measurable pulse coming out of the

etalon (Figure 6.1) has to be at least $6.2 \cdot 10^{-5}$ Volts; anything below that will be under the sensitivity of the 14 bits instrumentation. If we increase the number of bits we will be able to record for a longer time before the signal dies off. But keep in mind that we also have to average more realizations to have a lower noise level, which may become impractical.

6.4.1 Time domain

It is much more natural, for us at least, to think of experiments in the time domain. Peculiar non-causal effects in the frequency domain can lead to apparent paradoxes. In the time domain we visualize the transmitted wave as having bounced back and forth in the cavity m times

$$E_m = E_o r^{2(m-1)} \left(t^2 e^{ikL}\right) e^{i2(m-1)kL} \tag{6.19}$$

and the amplitude is

$$|E_m| = E_o t^2 r^{2(m-1)} \tag{6.20}$$

We want to arrange things so that the first pulse leaving the cavity has a peak voltage of 1 Volt, since we are assuming this is the maximum we can record with our instrumentation. Hence, $|E_i| = 1/t^2$ has to be the amplitude of the incident wave E_i.

We can now calculate the number of bounces m the wave makes in the etalon before it becomes undetectable with our 14 bits instrument, meaning that $E_{min} = |E_m|$. From equations (6.19), (6.20) and (6.18) we calculate

$$m = \frac{log(|E_m|)}{2log(r)} + 1. \tag{6.21}$$

The time T_{max} it takes for the wave to bounce m times is

$$T_{max} = \frac{2N_{unp}Lm}{c_o} = \left[\frac{log(|E_m|)}{log(r)} + 2\right] \frac{LN_{unp}}{c_o} \tag{6.22}$$

For a 14 bits instrument and a reflection index r of 0.99 we will be able to measure a wave that has bounced back and forth 483 times and it takes a time

$$T_{max} = \left[\frac{log(6.29 \cdot 10^{-5})}{log(r)}) + 2\right] \frac{LN_{unp}}{c_o}, \tag{6.23}$$

to do so. After that the amplitude of the wave decays below the sensitivity of the instrument. We now perturb the medium inside the etalon by δN and the maximum recordable time becomes

$$\tilde{T}_{max} = \frac{2\delta NLm}{c_o} = \left[\frac{log(|E_m|)}{log(r)} + 2\right] \frac{L\left(N_{unp} + \delta N\right)}{c_o}. \tag{6.24}$$

The time difference δt that we want to resolve from the two measurement (before and after the perturbation) is the difference between T_{max} and $\tilde{T}_{max}$, and from equations 6.23 and

6.24 we obtain

$$\delta t = \frac{2\delta N L m}{c_o} = \left[\frac{log(|E_m|)}{log(r)} + 2\right] \frac{L\delta N}{c_o}. \tag{6.25}$$

Solving for δN in equation (6.25) and for N_{unp} in equation (6.22) leads to the relative change in index of refraction

$$\frac{\delta N}{N_{unp}} = \frac{\delta t}{T_{max}}. \tag{6.26}$$

This is a telling result. Equation 6.26 lets us compute the theoretical sensitivity for a given experiment and instrumentation. δt is the smallest possible time shift we can measure with a given instrumentation. It can also be thought of as the smallest sampling interval our instrument can measure. T_{max} is given by Equation 6.22 and depends on the dynamic range DR and the reflection coefficient r. Dynamic range and sampling interval are set by the instrumentation and have nothing to do with the physics of the experiment. We can always make the instruments more sensitive by increasing the number of bits and/or the sampling interval, up to the limits of modern technology. The reflection coefficient r, however, is given by the nature of the experiment and it limits the sensitivity of the time domain analysis. A reflectivity close to 1 leads to a large maximum recording time T_{max} and makes for a very sensitive analysis of the data (Figure 6.4). A small reflection coefficient, however, will make our analysis insensitive. In other words, if all the energy is leaks out of the etalon quickly, we can only record few bounces between the mirrors before the amplitudes are smaller than the dynamic range.

We only considered a single pulse at time T_{max}. But we can repeat the analysis for each time the wave bounces back and forth between the mirrors. Hence, we can estimate m independent values of $\delta N/N_{unp}$ and therefore reduce the uncertainty by a factor of $1/\sqrt{m}$.

Furthermore, in this particular experiment we know the path length that the waves have traveled, namely L times the number of bounces m. By measuring the time it takes to traverse that path (T_{max}) we obtain the index of refraction N_{unp} and our measurement becomes an absolute measurement of the change instead of a relative one.

For band-limited data we can still estimate δt by comparing the maxima of the waves. In the case we include noise, however, it becomes a little more complicated. A suitable method to estimate δt is the cross-correlation function, which estimates δt directly. We show how we can get δt from the cross-correlation on an example of Gaussian wave-packets.

In this case we launch a Gaussian pulse into the etalon and record the many echos until the maximum time T_{max}. If we assume, that we can window the signal around the last recorded echo, we get the following expression for the unperturbed wavefield

$$E_{unp}(t) = |E_m| e^{\frac{-\pi(t-T_{max})^2}{\sigma^2}}, \tag{6.27}$$

and for the perturbed wavefield

$$E_{pert}(t) = |E| e^{\frac{-\pi(t-\tilde{T}_{max})^2}{\sigma^2}}, \tag{6.28}$$

where a velocity change δN introduces a time shift δt in the perturbed wavefield and can

be extracted by means of the cross-correlation function $C(t)$ of $E_{unp}(t)$ and $E_{pert}(t)$. σ is defined as the full-width at half-max (FWHM) and determines the band-width in our example. We calculate $C(t)$ by multiplication in the Fourier domain

$$C(\omega) = E_{unp}(k)E^*_{pert}(k), \tag{6.29}$$

where the star denotes the complex conjugate in the Fourier domain. The wavefields in the Fourier domain are given by

$$E_{unp}(\omega) = |E_m|\sigma e^{-\pi\omega^2\sigma^2} e^{-i2\pi\omega T_{max}}, \tag{6.30}$$

and

$$E_{pert}(\omega) = |E_m|\sigma e^{-\pi\omega^2\sigma^2} e^{-i2\pi\omega \tilde{T}_{max}}. \tag{6.31}$$

Inserting 6.31 and 6.30 into 6.29 leads to

$$C(\omega) = |E_m|^2\sigma^2 e^{-2\pi\omega^2\sigma^2} e^{-i2\pi\omega(T_{max}-\tilde{T}_{max})}. \tag{6.32}$$

Inverse Fourier transform gives

$$C(t) = |E_m|^2\sigma^2 e^{\frac{-2\pi(t-(T_{max}-\tilde{T}_{max}))}{\sigma^2}}. \tag{6.33}$$

Hence, the cross-correlation function $C(t)$ is centered at $\delta t = T_{max} - \tilde{T}_{max}$, which is the object of the time-domain calculation and can be estimated from the location of the maximum of $C(t)$. Computing δt with the cross-correlation function has the advantage that we estimate δt directly, this is better than computing two large values (T_{max} and $\tilde{T}_{max}$) and subtracting in order to get a small value. Furthermore, the cross-correlation function can be thought as the impulse response (or Green function) of the perturbation in the medium. In other words, by convolving $E_{unp}(t)$ with $C(t)$ we can compute $E_{pert}(t)$.

6.4.2 Frequency domain

Ironically, many frequency oscillators create sinusoids by coupling pulses to a stable cavity. In any case, the key to making a frequency domain measurement is having a stable, tunable oscillator. Of course, all measurements are made in laboratory time, but if we measure any frequency dependent quantity $A(\omega)$ at enough frequency points we have, in effect, measured the Fourier Transform of its time-domain response $A(t)$. A measurement at a given frequency corresponds to driving the system under test with an long sinusoid and measuring either the amplitude and phase of the response (or quadrature components, i.e., the Cartesian components of the amplitude/phase), or for optical measurements, measuring the time-averaged intensity of the signal.

This means we cannot think of rays reflecting in time off the mirrors any more. We must think in terms of modes of oscillation. We want to find the value δN associated with an index perturbation in the cavity. To do this, we will measure the frequency-shift associated with any one of the cavity modes.

We have already shown that for a large number of reflections the frequency-dependent transmission intensity is Equation 6.9

$$T = \frac{I_t}{I_i} = \frac{1}{1 + K\sin^2(NL\omega/c_0)}.$$

If we look at Equation 6.9 our first thought is that in order to get a transmitted intensity (I_T) of one, the argument of the sin must be zero. This is not the case, however, since none of the parameters (N, L, ω, c_0) are zero. The argument is any integer multiple of π.

The ideal way to measure this frequency shift is to perform a frequency-sweep of the unperturbed system and find one of the frequencies of maximum intensity (I_T) as shown in Figure 6.2. When the system is perturbed by some δN, perform the frequency sweep again in the same neighborhood to obtain the new frequency of maximum intensity. This gives $\delta\nu$, the frequency shift.

As previously mentioned, we would like to find the relative sensitivity $\delta N/N_{unp}$. We begin by rewriting kLN as

$$kLN = \frac{1}{\lambda}2\pi LN = \frac{\nu}{c_0}2\pi LN. \tag{6.34}$$

Replacing kLN and solving for the index of refraction gives

$$N = \pm\frac{1}{\nu}\frac{2\pi L}{c_0}\arcsin\left(\sqrt{\frac{1-T_I}{\left(\frac{2r}{1-r^2}\right)^2 T_I}}\right). \tag{6.35}$$

Negative index of refraction materials do exist, but for simplicity we consider only positive N. The first thing to notice is that ν depends on $1/N$, so when N is increased to $N_{unp}+\delta N$, our observed frequency maximum decreases. We denote the perturbed frequency as ν_{pert} so that $\nu_{pert} = \nu_{unp} + \delta\nu$.

$$\delta N = N_{pert} - N_{unp} =$$
$$= \left(\frac{\delta\nu}{\nu_{unp}^2 - \nu_{unp}\delta\nu}\right)\frac{2\pi L}{c_0}\arcsin\left(\sqrt{\frac{1-T_I}{\left(\frac{2r}{1-r^2}\right)^2 T_I}}\right) \tag{6.36}$$

Finally, we construct the ratio $\delta N/N$ to obtain

$$\frac{\delta N}{N_{unp}} = \frac{\delta\nu}{\nu + \delta\nu}. \tag{6.37}$$

The sensitivity is dependent upon the frequency shift, much like the time-domain method is dependent upon a time shift. However, there is an additional dependence on frequency. For higher frequencies, or higher modes excited in the cavity, the frequency-domain measurement is more sensitive because the same perturbation δN results in a larger

frequency shift.

Note that we can use the spacing between adjacent intensity maxima to obtain an absolute value for the index of refraction N via $\nu_{n+1} - \nu_n = 2NL/c_0$ since we know the cavity length. That means we can also obtain an absolute measure of the perturbation δN from Equation 6.37.

The most interesting thing to notice is what happens if we measure the frequency shift at one of the resonant modes. In Equation 6.7, the denominator becomes unity and for a sufficiently large number of reflections (m large), the numerator $(1 + r^{4m} - 2r^{2m}\cos(2mNL\omega/c_0))^2$ approaches unity for *all* values of reflectivity r. That means our measurement is *independent* of the reflectivity of the mirrors in the frequency domain! This is not the case in the time domain.

6.4.3 Time-frequency domain

In the previous discussion of the time-domain problem a single pulse was analyzed before and after the perturbation. This was then extended to multiple pulses as a way of improving the signal-to-noise ratio of the one-pulse estimate of the perturbation. In doing so, however, we were implicitly treating the pulses as being independent. But the pulses are not independent since they have a common origin. This is an example of *phase coherence.* This coherence manifests itself as an interference effect. Even if the pulses do not overlap in time, provided they are phase coherent when we integrate over all time (by going to the Fourier domain, for example) the interference fringes will show up. These fringes are the key to improving the resolution of the independent-pulse treatment.

The fact that a train of phase-locked pulses gives rise to a harmonic comb of frequencies is routinely exploited in optics (e.g., (Teets *et al.*, 1977), (Bellini *et al.*, 1997)). The idea is very simple. Consider a Gaussian pulse measured at a fixed location

$$E(\tau) = \frac{1}{\sqrt{2\pi\sigma}} e^{-(\tau-\Delta\tau)^2/2\sigma^2}.$$

The time shift introduces a phase shift in the Fourier transform:

$$E(\omega) = \sqrt{\frac{\sigma}{2\pi}} e^{-i\omega\Delta\tau} e^{-\sigma^2\omega^2/2}.$$

Hence, the power spectrum (i.e., the intensity in the frequency domain) for two identical pulses separated by $\Delta\tau$ will contain an interference term. The envelope of the power spectrum will still be the Gaussian $e^{-\sigma^2\omega^2/2}$, but there will be modulation with peaks of full-width at half-max (FWHM) $\pi/\Delta\tau$ and separation $1/\Delta\tau$. For m such pulses the power spectrum is a geometric series the summation of which is:

$$I_m(\omega) = \frac{\sigma}{2\pi} e^{-\sigma^2\omega^2} \left(\frac{1 - \cos(\omega n \Delta\tau)}{1 - \cos(\omega\Delta\tau)} \right). \tag{6.38}$$

In the $m-$pulse case the spacing between the peaks of the power spectrum is still $1/\Delta\tau$ but

the FWHM is $2\pi/m\Delta\tau$. Provided $\Delta\tau$ is constant, then for large m, the pulse superposition provides a precise ruler in the frequency domain, allowing pulse trains to achieve bandwidth far below that of a single pulse (see (Udem & Fergusen, 2002)).

This is almost the result we need. To take into account the nature of the etalon, we simply have to incorporate a decay which goes as r^2 for each back-and-forth reflection in the etalon and an overall factor of t^2 for the transmission. Also, it is convenient to shift the origin of time so that the first pulse through the etalon arrives at the detector at $\tau = 0$. Then, one can show that the total field after m bounces in the etalon is:

$$E_m(t) = \frac{t^2 e^{-\sigma^2\omega^2/2}}{\sqrt{2\pi\sigma}} \left[\frac{1 - r^{2(m+1)} e^{-i\omega(m+1)\Delta\tau}}{1 - r^2 e^{-i\omega\Delta\tau}} \right] \tag{6.39}$$

This is actually extremely close Equation 6.4, recognizing the time delay $\Delta\tau = L/c$. In fact the only real difference is that in 6.4 the envelope of the transmitted field in the frequency domain is flat, since the incident field is just $e^{i\omega t}$, whereas now we are considering Gaussian pulses. So when we compute the intensity associated with Equation 6.39 in the limit of a large number of bounces m we get

$$E(\omega)E(\omega)^* = \frac{\sigma}{2\pi} t^2 e^{-\sigma^2\omega^2} \frac{1}{1 - 2r^2\cos(\omega\Delta\tau)} \tag{6.40}$$

For the finite-time case we have the transmitted intensity after m bounces

$$I(\omega)_t = \frac{\sigma}{2\pi} t^2 e^{-\sigma^2\omega^2} \frac{1 + r^{4m} - 2r^{2m}\cos(\omega m\Delta\tau)}{1 + r^4 - 2r^2\cos(\omega\Delta\tau)}. \tag{6.41}$$

This result can be seen to be a product of a Gaussian envelope and a trigonometric term associated with the interference of the multiple pulses. The interference term is identical to Equation 6.7 when we swap $\Delta\tau$ for the equivalent NL/c_0.

The key idea is that we can exploit the fringes of the interference term to enhance the resolution of the estimates of the perturbation, over what would have been the case with independent pulses. The only difference between this result and the earlier pure frequency domain one is that in the frequency domain the incident field is a monochromatic plane wave and hence the envelope is flat.

For pulses, the breadth of the envelope of the frequency domain intensity is inversely related to the pulse width; this breadth does not depend at all on the time of the recording time. Whereas the FWHM of the interference fringes depends on the number of bounces. So this brings in the finite recording time (and hence the attenuation of the cavity) in a fashion that is mid-way between the pure time-domain and the pure-frequency domain approaches.

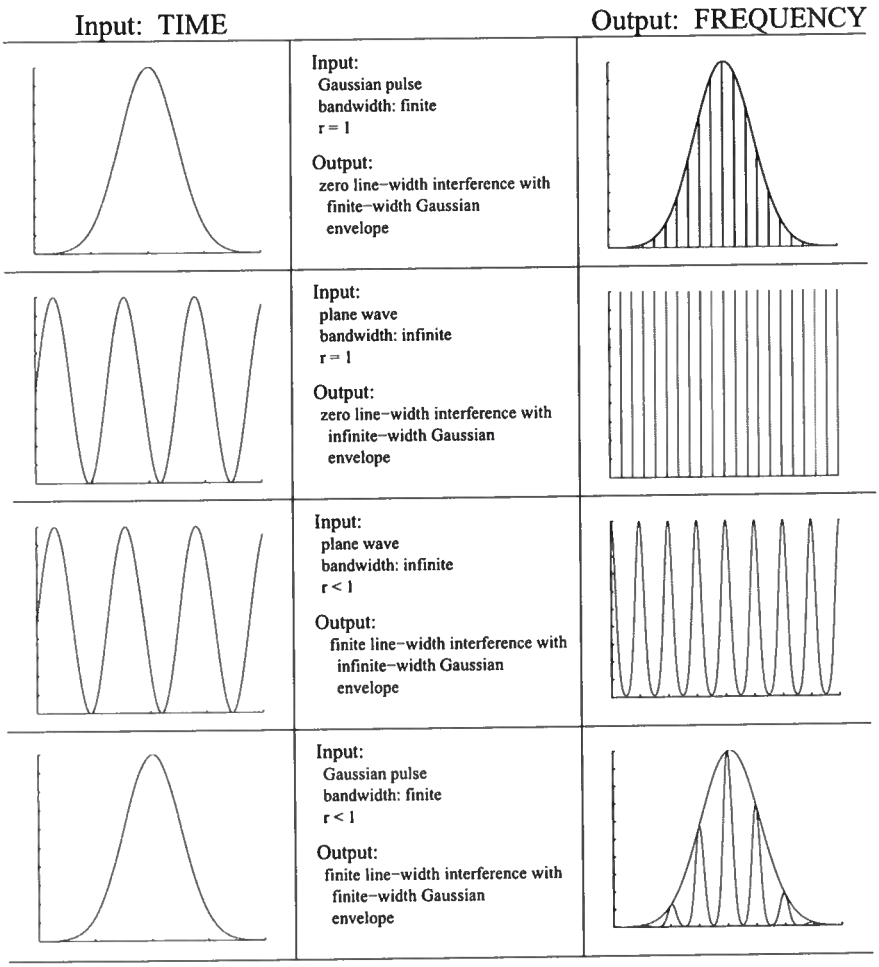

Figure 6.3. *Left:* Time-domain input signal. *Center:* Descriptions of experimental inputs and outputs. *Right:* Frequency-domain output signal (or Fourier Transform of time-domain output).

6.4.4 Comparison of the different methods

Conceptually an impulse-response (time-domain) experiment is the easiest to visualize, and usually perform. As a pulse propagates through the medium, the properties of the medium are impressed on it. If the pulse is somehow confined, then it samples the medium many times. In the limit of no attenuation or loss, the incident pules samples the medium indefinitely. If we make a small perturbation to the system, so small that it is not visible in the first pulse, it may be that if we wait long enough we can see the effect at late times. This is the basic idea of Coda Wave Interferometry and Cavity Ring-Down Spectroscopy. At the simplest level, we can simply compare two late-time pulses (before and after the perturbation). Cross-correlation of these two pulses gives, in effect, the impulse response of the perturbation. This two-pulse approach can be extended statistically by considering many pairs of pulses independently.

But we know that the pulses are not independent, they arise from one source so they are *phase locked.* As a result, not matter how far separated the pulses are in the time domain, when we Fourier Transform to the frequency domain, we get interference fringes in the system response. These interference fringes become increasingly sharp as the number of pulses in the Fourier Transform increases. Ultimately we can sharpen the fringes no more than the *natural line-width* associated with the Finesse of the cavity. And as we showed in the text, the envelope of this system response function is governed by the bandwidth of the incident pulse. As the pulse becomes more and more delta-like, the envelope in the frequency domain becomes more and more flat. In the limit of true delta-function spike, we recover the frequency domain approach, which corresponds to driving the system with a pure sinusoid at a fixed frequency and then sweeping the frequency over some range.

The situation is summarized in Figure 6.3. At the top we see an incident Gaussian pulse. It bounces back and forth many times in the cavity and the Fourier Transform of the response is a Gaussian envelope with interference fringes. The spacing between the fringes depends on the cavity properties, while the width of the fringe depends, additionally, on the number of bounces. If the reflectivity of the mirror approaches 1, then at the eigenfrequencies of the cavity, we have an infinite number of bounces and the line-width goes to zero. As a corollary, in between the eigenfrequencies, no light gets through at all. This is what we call the time-frequency domain.

In the next panel we show the result of applying a fixed sinusoidal input signal. As we sweep over frequencies we get the same result as in the time-frequency approach except that the envelope of the fringes is flat, since we're putting in a constant amplitude at each frequency.

The bottom two panels show the same results but in the case of a more realistic ($r < 1$) mirror. In this case there is a natural linewidth associated with the fringes that depends on the finesse of the cavity. For the pulse experiment at the bottom, there is an additional linewidth associated with the number of bounces in the etalon. In the limit that this becomes large, the linewidth of the time-frequency method approaches the pure frequency domain method.

In addition to the interference fringes, there is another fundamental, physical difference

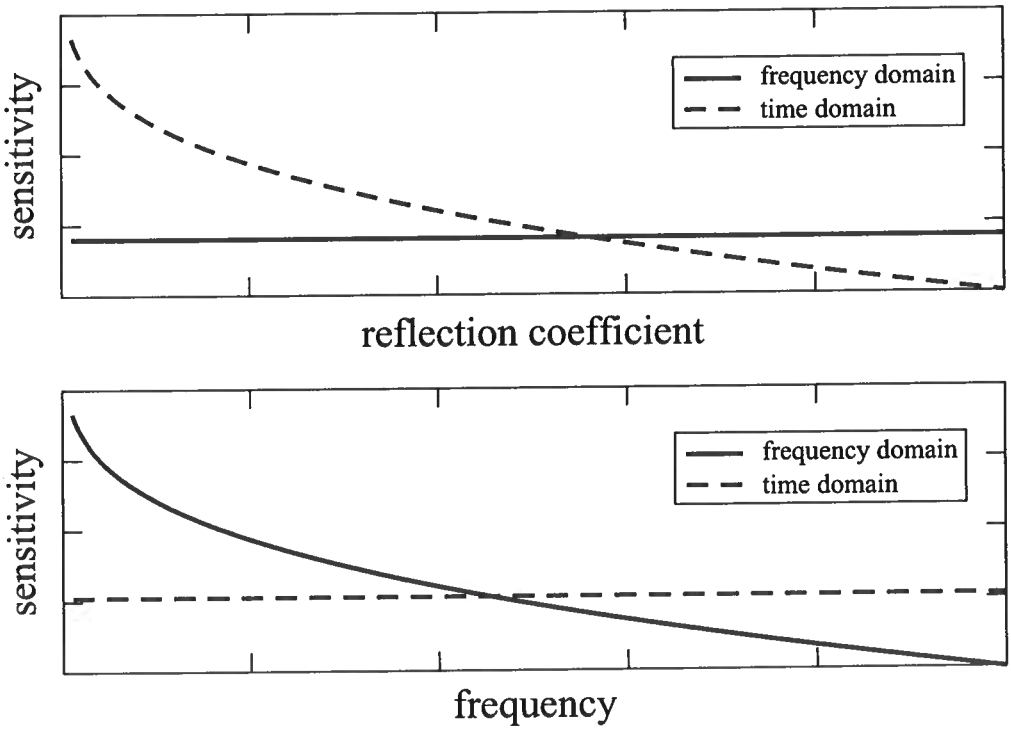

Figure 6.4. Comparison of time- and frequency-domain sensitivities ($\delta N/N$) as a function of frequency and reflection coefficient. A higher sensitivity corresponds to a lower value on the vertical scale.

between the time-domain and the frequency-domain approach. In the time domain we can measure a finite number of bounces between the mirrors depending on the reflectivity. We can put more energy into the system by averaging many traces, which will decrease the noise level but not increase the maximum recordable time and the number of bounces. Hence, the sensitivity of the time-domain method depends on the reflectivity even in the noise free case (see top part of Figure 6.4 *top*). In contrast, we can drive the system in the frequency domain as long as we want, also leading to a noise-free signal where the sensitivity does not depend on the reflectivity of the mirrors (Figure 6.4 *top*).

Similarly, the sensitivity of the frequency-domain measurement depends on the particular frequency we use, where the method is more sensitive at higher frequencies. In contrast, the data analysis in the time-domain has a constant sensitivity independent of frequency (Figure 6.4 *bottom*).

6.5 Acknowledgments

We acknowledge many useful discussion with Roel Snieder, Kasper van Wijk and Martin Smith. This work was partially supported by the National Science Foundation (EAR-0337379).

References

Aki, K. 1969. Analysis of seismic coda of local earthquakes as acattered waves. *J. Geophys. Res.*, **74**, 615–631.

Aki, K. 1985. Theory of earthquake prediction with special reference to monitoring of the quality factor of lithosphere by the coda method. *Earthquake Res. Bull.*, **3**, 219–230.

Aki, K., & Chouet, B. 1975. Origin of coda waves: Source, attenuation, and scattering effects. *J. Geophys. Res.*, **80**, 3322–3342.

Aki, K., & Ferrazzini, V. 2000. Seismic monitoring and modeling of an active volcano for prediction. *J. Geophys. Res.*, **105**(B7), 16617–16640.

Aster, R., Mah, S. Y., Kyle, P., McIntosh, W., Dunbar, N., Johnson, J., Ruiz, M., & McNamara, S. 2003. Very long period oscillations of Mount Erebus Volcano. *J. Geophys. Res.*, **108**, 2522.

Bachrach, R., & Nur, A. 1998. High-resolution shallow-seismic experiments in sand, Part I: Water table, fluid flow, and saturation. *Geophysics*, **63**, 1225–1233.

Baisch, S., & Bokelmann, G.H.R. 2001. Seismic waveform attributes before and after the Loma Prieta earthquake: Scattering change near the earhtquake and temporal recovery. *J. Geophys. Res.*, **106**, 16323–16337.

Bellini, M., Bartoli, A., & Hänsch, T.W. 1997. Two-Photon Fourier Spectroscopy with Femtosecond Light Pulses. *Opt. Lett.*, **22**, 540–542.

Bokelmann, G.H., & Silver, P.G. 2002. Shear stress at the base of shield lithosphere. *Geophys. Res. Lett.*, **29**(23), 2091–2099.

Boley, B.A., & Weiner, J.H. 1960. *Theory of Thermal Stresses.* Dover Publications New York. Page 586.

Born, M., & Wolf, E. 199. *Principles of Optics: Electromagnetic Theory of Propagation, Interference and Diffraction of Light.* 7 edn. Cambridge University Press.

Carmichael, R. S. 1982. *Handbook of Physical Properties of Rocks.* Florida: CRC Press.

Chern, C.J., & Heyman, J.S. 1981. Determination of material stress from the temperature dependence of acoustic natural velocity. *Proceedings of the IEEE Ultrasonic Symposium*, 960–965.

Chouet, B. 1979. Temporal variation in the attenuation of earthquake coda near Stone Canyon, California. *Geophys. Res. Lett.*, **6**, 143–146.

Christensen, N.I., & Wang, H.F. 1985. The Influence of Pore Pressure and Confining Pressure on Dynamic Elastic Properties of Berea Sandstone. *Geophysics*, **50**, 207–213.

Cowan, M. L., Jones, I. P., Page, J. H., & Weitz, D. A. 2002. Diffusing acoustic wave spectroscopy. *Physical Review E*, **65**, 066605–1–11.

Dahlen, F. A., & Tromp, J. 1998. *Theoretical Global Seismology.* Princeton University Press.

Dodge, D.A., & Beroza, G.C. 1997. Source Array Analysis of Coda Waves Near the 1989 Loma Prieta, California, Mainshock: Implications for the Mechanism of Coseismic Velocity Changes. *J. Geophys. Res.*, **102**, 24437–24458.

Fehler, M., Roberts, P., & Fairbanks, T. 1998. A temporal change in coda wave attenuation observed during an eruption of Mount St. Helens. *J. Geophys. Res.*, **93**, 4367–4373.

Fink, M. 1997. Time reversed Acoustics. *Physics Today*, **20**, 34–40.

Foldy, L.L. 1945. The Multiple Scattering of Waves, I. General Theory of Isotropic Scattering by Randomly Distributed Scatterers. *Phys. Rev.*, **67**, 107–119.

Fredrich, J.T., & Wong, T. 1986. Micromechanics of thermally induced cracking in three crustal rocks. *J. Geophys. Res.*, **91**, 12743–12764.

Freed, A.M., & Lin, J. 2001. Delayed triggering of the 1999 Hector Mine earthquake by viscoelastic stress transfer. *Nature*, **411**, 180–183.

Friedel, M. J., Jackson, M. J., Scott, D. F., Williams, T. J., & S., Olson. M. 1995. 3D Tomographic Imaging of Anomalous Conditions in a Deep Silver Mine. *Applied Geophysics*, **34**, 1–21.

Friedel, M. J., Scott, D. F., Jackson, M. J., Williams, T. J., & Killen, S. M. 1996. 3D Tomographic Imaging of Anomalous Stress Conditions in a Deep U.S. Gold Mine. *Applied Geophysics*, **36**, 1–17.

Got, J.L., Poupinet, G., & Fréchet, J. 1990. Changes in source and site effects compared to coda Q-1 temporal variations using microearthquake doublets in California. *Pure Appl. Geophys.*, **134**, 195–228.

Grêt, A. A., Snieder, R., & Aster, R. 2004a. Monitoring rapid temporal change in a Volcano with Coda Wave Interferometry. *submitted to Geophysical Research Letters.*

Grêt, A. A., Snieder, R., & Ozbay, U. 2004b. Monitoring stress change in an underground mining environment with coda wave interferometry. *submitted to Journal of Mining Applications.*

Grêt, A. A., Snieder, R., & Scales, J. 2004c. Time-lapse Monitoring of Rock Properties with Coda Wave Interferometry. *submitted to Journal of Geophysical Research.*

Griffin, T.W., & Watson, K.W. 2002. A Comparison of Field Techniques for Confirming Dense Nonaqeuous Phase Liquids. *Ground Water Monitoring and Remediation*, **22**(2).

Groenenboom, J., & Snieder, R. 1995. Attenuation, Dispersion and Anisotropy by Multiple Scattering of Transmitted Waves Through Distributions of Scatterers. *J. Acoust. Soc. Am.*, **98**, 3482–3492.

Hanna, T. H. 1985. Field Instrumentation in Geotechnical Engineering. *Trans Tech Publications.*

Hawkes, I., & Bailey, W. V. 1973. Design, develop, fabricate, test and demonstrate permissible low cost cylindrical stress gages and associated components capable of measuring change in stress as a function of time in underground coal mines. *U.S. Department of the Interior, Bureau of Mines.*

Heckmeier, M., & Maret, G. 1997. Dark Speckle Imaging of Colloidal Suspensions in Multiple Light Scattering Media. *Progr. Colloid. Polym. Sci.*, **104**, 12–16.

Hicks, W.G., & Berry, J.E. 1956. Application of Continuous Velocity logs to Determination of Fluid Saturation of Reservoir Rocks. *Geophysics*, **21**, 739–744.

Hodges, J. T., Layer, H. P., Miller, W. W., & Scace, G. E. 2004. Frequency-stabilized single-mode cavity ring-down apparatus for high-resolution absorption spectroscopy. *Review of Scientific Instruments*, **75**(4), 849–863.

Hubbert, M. K., & Willis, D. G. 1957. Mechanics of Hydraulic Fracturing. *Pages 153–168 of:* Hubbert, M. K. (ed), *The 1957 Transactions of A.I.M.E.*, vol. 210.

Hughes, D.S., & Maurette, C. 1956. Variation of elastic wave velocities in granites with pressure and temperature. *Geophysics*, **21**, 277–284.

Ide, J.M. 1937. The velocity of sound in rocks and glasses as a function of temperature. *J. Geol.*, **45**, 689–716.

Joass, G. G. 1993. Stability monitoring on the west wall of the Muja open cut. *Pages 283–291 of:* Szwedzicki, T (ed), *Proceedings of Geotechnical Instrumentation and Monitoring in Open Pit and Underground Mining.* Kalgoorlie, Western Australia: Balkema, Rotterdam.

Johnson, B., Gangi, A.F., & Handin, J. 1978. Thermal cracking subjected to slow, uniform temperature changes. *paper presented at 19th U.S. Rock Mechanics Symposium, U.S. Nat. Comm. for Rock Mech., Univ. of Nevada, Reno.*

Kaiser, J. 1953. Erkenntnisse und Folgerungen aus der Messung von Gerüschen bei Zugbeanspruchung von metallischen Werkstoffen. *Archiv Eisenhüttenwesen*, **24**, 43–45.

Kern, H., Popp, T., Gorbatsevich, F., Zkarikov, A., Labanov, K.V., & Smirnov, Yu.P. 2001. Pressure and temperature dependence of V_P and V_S in rocks from the superdeep well and from surface analogues at Kola and the nature of velocity anisotropy. *Tectonophysics*, **338**, 113–134.

King, M.S. 1966. Wave Velocities in Rocks as a Functin of Changes in Overvurden Pressure and Pore Fluid Saturation. *Geophysics*, **31**, 50.

Kobori, O., & Iwashimizu, Y. 1990. *Effects of stress and temperature on ultrasonic velocity.* Elastic Waves and Ultrasonic Nondestructive Evaluation. Elsevier.

Kurita, K., & Fujii, N. 1979. Stress memory of crystalline rocks in acoustic emission. *Geophys. Res. Letters*, **6**, 9–12.

Lagendijk, A., & van Tiggelen, B.A. 1996. Resonant Multiple Scattering of Light. *Phys. Rep.*, **270**, 143–215.

Lauterborn, W., & Kurz, T. 2003. *Coherent Optics.* second edn. Springer.

Lavrov, A. 2002. The Kaiser effect in rocks: principles and stress estimation technique. *International Journal of Rock Mechanics and Mining Sciences*, **40**, 151–171.

Leary, P.C., Malin, P.E., Phinney, R.A., Brocher, T., & Von-Colln, R. 1979. Systematic Monitoring of Milisecond Travel Time Variations Near Palmdale, California. *J. Geophys. Res.*, **84**, 659–666.

Lee, W. H. K., Bennett, R. E., & Meagher, K. L. 1972. A method of estimated magnitude of local earthquakes from signal duration. *U.S. Geol. Surv. Open File Report.*

Li, X., Durduran, T., Chance, B., Yodh, A.G., & Pattanayak, D. 1997. Diffraction Tomography for Biomedical Imaging with Diffuese-photon Density Waves. *Optics Letters*, **22**, 573–575.

Li, Y.G., Vidale, J.E., Aki, K., & Xu, F. 2000. Depth-Dependent Structure of the Landers Fault Zone From Trapped Waves Generated by Aftershocks. *J. Geophys. Res.*, **105**, 6237–6254.

Lumley, D.E. 1995. *Seismic time-lapse monitoring of subsurface fluid flow.* Ph.D. thesis, Stanford Univ.

Maret, G. 1995. Recent Experiments on Multiple Scattering and Localization of Light. *In:* Akkermans, E., Montambaux, G., Picard, J.L., & Zinn-Justin, J. (eds), *Mesoscopic quantum physics.* Amsterdam: Elsevier Science.

Maret, G., & Wolf, P.E. 1987. Multiple Light Scattering From Disordered Media. The Effects of Brownian Motion of Scatterers. *Z. Phys. B. - Condensed Matter*, **65**, 409–413.

Mavko, G. M., & Nur, A. 1979. Wave attenuation in partially saturated rocks. *Geophysics*, **44**(02), 161–178.

McSkimmin, H. J. 1964. *Ultrasonic methods for measuring the mechanical properties of liquids and solids, in Physical Acoustics.* Vol. 1A. Academic Press.

Meredith, P.G., Knigh, K.S., Boon, S.A., & Wood, I.G. 2001. The microscopic origin of thermal cracking in rocks: An investigation by simultaneous time-of-flight neutron diffraction and acoustic emission monitoring. *Geophys. Res. Lett*, **28**, 2105–2108.

Migliori, A., & Sarrao, J. L. 1997. *Resonant ultrasound spectroscopy: applications to physics, materials measurements, and non-destructive evaluation.* John Wiley & Sons, INC., New York.

Miller, V., & Savage, M. 2001. Changes in seismic anisotropy after volcanic eruptions: Evidence from Mount Ruapehu. *Science*, **293**, 2231–2233.

Mjaaland, S., Causse, E., & Wuldd, A.M. 2001. Seismic monitoring from intelligent wells. *The Leading Edge*, **20**, 1180–1184.

Nikitin, O. 2003. Mining block stability analysis for room-and-pillar mining with continuous miner in estonian oil shale mines. *Oil Shale*, **20**, 515–528.

Niu, F., Silver, P.G., Nadeau, R.M., & McEvilly, T.V. 2003. Migration of seismic scatterers associated with the 1993 Parkfield aseismic transient event. *Nature*, **426**, 544–548.

Nur, A. 1971. Effect of stress on velocity anisotropy in rocks with cracks. *Journal of Geophysical Research*, **76**, 2022–2034.

Nur, A., & Simmons, G. 1969. The Effect of Saturation on Velocity in Low Porosity Rocks. *Earth Planet. Sci. Lett*, **7**, 183–190.

O'Keefe, A., & Deacon, D. A. G. 1988. Cavity ring-down optical spectrometer for absorption measurements using pulsed laser sources. *Review of Scientific Instruments*, **59**(12), 2544–2551.

Pacheco, C. 2003. *Localized Coda Wave Interferometry.* M.Phil. thesis, Colorado School of Mines.

Pacheco, C., & Snieder, R. 2003. *Time-lapse monitoring with multiply scattered waves.* Soc. of Expl. Geophys. extended abstracts. Pages 1849–1852.

Peselnick, L., & Stewart, R.M. 1975. A sample assembly for velocity measurements of rocks at elevated temperatures and pressures. *J. Geophys. Res.*, **80**, 3765–3768.

Poupinet, G., Ellsworth, W. L., & Frechet, J. 1984. Monitoring Velocity Variations in the Crust Using Earthquake Doublets: an Application to the Calaveras Fault, California. *J. Geophys. Res.*, **89**, 5719–5731.

Ratdomopurbo, A., & Poupinet, G. 1995. Monitoring a Temporal Change of Seismic Velocity in a Volcano: Application to the 1992 Eruption of Mt. Merapi (Indonesia). *Geophys. Res. Lett.*, **22**, 775–778.

Rayleigh, John William Strutt, Baron. 1896, 1945 re-issue. *The Theory of Sound.* 2 edn. Vol. 1. New York: Dover Publications.

Revenaugh, J. 1995. The Contribution of Topographic Scattering to Teleseismic Coda in Southern California. *Geophys. Res. Lett.*, **22**, 543–546.

Roberts, P.M., Scott Phillips, W., & Fehler, M.C. 1992. Development of the active doublet method for measuring small velocity and attenuation changes in solids. *J. Acoust. Soc. Am.*, **91**, 3291–3302.

Robinson, R. 1987. Temporal variations in coda duration of local earthquakes in the Wellington region, New Zealand. *Pure Appl. Geophys.*, **125-130**.

Rowe, C., Aster, R., Schlue, R. Kyle P., & Dibble, J. 1998. Broadband recording of Strombolian explosions and associated very-long-period seismic signals on Mount Erebus volcano, Ross Island, Antarctica. *Geophys. Res. Lett.*, **25**, 2297–2300.

Salama, K., & Ling, C.K. 1980. The effect of stress on the temperature dependence of ultrasonic velocity. *J. Appld. Phys.*, **51**, 1505–1510.

Sarkar, D., Bakulin, A., & Kranz, R. L. 2003. Anisotropic inversion of seismic data for stressed media: Theory and a physical modeling study on Berea Sandstone. *Geophysics*, **68**(2), 690–704.

Sato, H. 1986. Temporal change in attenuation intensity before and after the eastern Yamanashi earthquake of 1983 in central Japan. *J. Geophys. Res.*, **91**, 2049–2061.

Sato, H. 1988. Temporal change in scattering and attenuation associated with the earthquake occurence - a review of recent studies on coda waves. *Pure Appl. Geophy.*, **126**, 465–497.

Scales, John A., & Malcolm, Alison E. 2003. Laser characterization of ultrasonic wave propagation in random media. *Phys. Rev. E*, **67**.

Scott, F. S., Jordan, J., Tesarik, D., Williams, T. J., & Denton, D. K. 1999. Validation of seismic tomography to detect stress in an underground mine. *NIOSH report.*

Sheppard, I., & Murie, A. 1992. Mining Lady Bountiful slip cut-back. *Pages 201–112 of:* Szwedzicki, T (ed), *Proceedings of Geotechnical Instrumentation and Monitoring in Open Pit and Underground Mining.* Kalgoorlie, Western Australia: Balkema, Rotterdam.

Simmons, G., & Cooper, H.W. 1978. Thermal cycling cracks in three igneous rocks. *Int. J. Rock Mech.*, **15**, 145–148.

Snieder, R. 1999. Imaging and Averaging in Complex Media. *Pages 405–454 of:* Fouque, J.P. (ed), *Diffuse waves in complex media.* Dordrecht: Kluwer.

Snieder, R. 2002. Coda wave interferometry and the equilibration of energy in elastic media. *Phys. Rev. E*, **66**, 046615–1,8.

Snieder, R. 2004. Coda wave interferometry. *Pages 54–56 of: 2004 McGraw-Hill yearbook of science & technology.* New York: McGraw-Hill.

Snieder, R., & Douma, H. 2000. Coda Wave Interferometry. *EOS Trans. AGU, Fall Meeting Suppl., Abstract*, **48**, 848.

Snieder, R., & Hagerty, M. 2004. Monitoring change in Volcanic Interiors using Coda Wave Interferometry: Application to Arenal Volcano, Costa Rica. *Geophys. Res. Lett.*, **31**, L09608, doi:10.1029/2004GL019670.

Snieder, R., & Scales, J.A. 1998. Time Reversed Imaging As a Diagnostic of Wave and Particle Chaos. *Phys. Rev. E*, **58**, 5668–5675.

Snieder, R., & Vrijlandt, M. 2004. Constraining Relative Source Locations with Coda Wave Interferometry: Theory and Application to Earthquake Doublets in the Hayward Fault, California. *submitted to J. Geophys. Res.*

Snieder, R., Grêt, A., Douma, H., & Scales, J. 2002. Coda Wave Interferometry for Estimating Nonlinear Behavior in Seismic Velocity. *Science*, **295**, 2253–2255.

Spencer, J. W. 1981. Stress relaxation at low frequencies in fluid-saturated rocks: Attenuation and modulus dispesion. *J. Geophys. Res*, **86**, 1803–1812.

Stein, R.S. 1999. The role of stress transfer in earthquake occurrence. *Nature*, **402**, 605–609.

Teanby, N., Kendall, J.M., Jones, R.H., & Barkved, O. 2004. Stress-induced temporal variations in seismic anisotropy observed in microseismic data. *Geophys. J. Int.*, **156**, 459.

Teets, R., Eckstein, J.N., & Hänsch, T.W. 1977. Coherent Two-Photon Excitation by Multiple Light Pulses. *Phys. Rev. Lett*, **38**, 760.

Terzaghi, K. 1936. The shearing resistance of saturated soils. *Pages 54–56 of: Proc. of the First International Conference on Soil Mechanics and Foundation Engineering*, vol. 1.

Thirumalai, K., & Demou, S.G. 1973. Thermal expansion behaviour of intact and thermal fractured mine rocks. *Am. Inst. Phys. Conf. Proc.*

Timur, A. 1977. Temperature dependence of compressional and shear wave velocities in rocks. *Geophysics*, **42**, 950–956.

Todd, T.P. 1973. Effects of cracks on elastic properties of low porosity rocks. *Thesis, Massachusetts Institute of Technology.*

Udem, T., & Fergusen, A.I. 2002. Achievements in optical frequency metrology. *In:* Figger, H., Meschede, D., & Zimmermann, C. (eds), *Laser physics at the limits.* Springer-Verlag.

Wang, Z. 1997. Feasibility of time-lapse seismic reservoir monitoring: The physical basis. *The Leading Edge*, **16**, 1327–1329.

Weaver, R.L., & Lobkis, O.I. 2000. Temperature Dependence of Diffuse Field Phase. *Ultrasonics*, **38**, 491–494.

Wegler, U., & Luehr, B. 2001. Scattering behaviour at Merapi volcano (Java) revealed from an active seismic experiment. *Geophysical Journal International*, **147**, 579–592.

Wulff, A.M., & Mjaaland, S. 2002. Seismic monitoring of fluid fronts: An experimental study. *Geophysics*, **67**, 221–229.

Wyllie, M.R., Gregory, A.R., & Gardner, G.H.F. 1958. An Experimental Investigation of Fractors Affecting Elastic Wave Velocities in Porous Media. *Geophysics*, **23**, 459.

Yong, C., & Wang, C. 1980. Thermally induced acoustic emission in Westerley granites. *Geophys. Res. Lett.*, **7**, 1089–1092.

Zadler, B., LeRousseau, J., Scales, J.A., & Smith, M.L. 2004. Resonance ultrasound spectroscopy: theory and application. *Geophysical Journal International*, **156**, 154–169.